# INTERFACIAL INTERACTIONS BETWEEN BIOMOLECULES AND MATERIALS

A Dissertation

by

ARACELY ROCHA-ZAPATA

Submitted to the Office of Graduate Studies of
Texas A&M University
in partial fulfillment of the requirements for the degree of

DOCTOR OF PHILOSOPHY

August 2011

Major Subject: Mechanical Engineering

# INTERFACIAL INTERACTIONS BETWEEN BIOMOLECULES AND MATERIALS

A Dissertation

by

ARACELY ROCHA-ZAPATA

Submitted to the Office of Graduate Studies of
Texas A&M University
in partial fulfillment of the requirements for the degree of

DOCTOR OF PHILOSOPHY

Approved by:

| | |
|---|---|
| Chair of Committee, | Hong Liang |
| Committee Members, | Sai C. Lau |
| | K. Ted Hartwig |
| | Victor M. Ugaz |
| Head of Department, | Jerald Caton |

August 2011

Major Subject: Mechanical Engineering

# ABSTRACT

Interfacial Interactions between Biomolecules and Materials. (August 2011)

Aracely Rocha-Zapata, B.S., The University of Texas-PanAmerican;

M.S., Texas A&M University

Chair of Advisory Committee: Dr. Hong Liang

This research investigates the interfacial interactions between biological entities and synthetic materials at two length scales: bulk and nanometer size. At the bulk scale, biomolecule adhesion is key for synthetic material incorporation in the body. Quantifying the adhesion strength becomes necessary. For the nanometer scale, the nanoparticles are generally delivered through the blood stream and their effect on the blood flow must be studied.

An experimental approach was taken to study interaction at both material length scales. The cell/protein adhesion strength to bulk-sized materials was studied. The goal was to identify the most influential factor affecting adhesion: chemistry or surface roughness. The effects of nanoparticles on the viscosity of protein and amino acid solutions were measured. A statistical thermodynamic analysis was focused on the entropy change induced by the addition of gold nanoparticles to protein/amino acid solutions.

Rheological studies were applied. A rheometer with a parallel plate was used to quantify the adhesion strength of cells and proteins to synthetic surfaces at the bulk

scale. The adhesion strength depends on the applied shear stress and the radius of cells or proteins that remained attached to the surface after testing. At the nanometer scale, the viscosity of the nanoparticle enhanced protein or amino acid solutions were measured with a cone and plate.

The adhesion studies were conducted with the following biological entities: fibroblasts, egg-white protein, and neurons. The fibroblast adhesion to poly(carbonate) and poly(methyl methacrylate) demonstrate fibroblasts are strongly attached to highly polar materials. Protein adhesion to titanium and chromium nitride coatings showed that chemical composition is the most influential factor. The neuron adhesion to poly-D-lysine coated glass demonstrated that neuron strengthening was due to an increase in adhesion molecules at the neuron/material interface. For nanoparticulates, it was found that the charged nanoparticles affect the protein and amino acid conformation and the potential energy of the solutions.

Quantifying biomolecule adhesion to surfaces and predicting the behavior of nanoparticles inside a biological system are crucial for material selection and application. The major impact of this research lies in observing the interaction mechanisms at the interfaces of material-biological entities.

# DEDICATION

To Julio and Valeria, it is all for you.

# ACKNOWLEDGEMENTS

I would like to thank my committee chair, Dr. Liang, for her guidance, support, and encouragement throughout the course of this research and thank my committee members, Dr. Lau, Dr. Hartwig and Dr. Ugaz for their time. Also, thank you to Dr. Vinson for his participation in the final defense.

I would like to extend my gratitude to our collaborators in this work, Dr. Hahn, Dr. Ko, Dr. Vinson and all their research groups.

Thanks also go to the Surface Science Group for their help, ideas, and great support at each group presentation, especially to the guys for making the graduate student life a fun ride.

I also want to extend my gratitude to the Diversity Fellowship, the GEM Fellowship, NSF – EAPSI, and NSF grant number 0535578 for their financial support.

# NOMENCLATURE

| | |
|---|---|
| NP | nanoparticle |
| NG | negative gold nanoparticle |
| PG | positive gold nanoparticle |
| L | lysine |
| A | arginine |
| GA | glutamic acid |
| AA | aspartic acid |
| CNS | central nervous system |
| DI | de-ionized water |
| PC | poly(carbonate) |
| PMMA | poly(methyl methacrylate) |
| PAH | poly(allylamine hydrochloride) |
| CTAB | cetyltrimethylammonium bromide |

# TABLE OF CONTENTS

CHAPTER Page

# LIST OF FIGURES

Page

Page

Page

Page

Page

Page

# LIST OF TABLES

# CHAPTER I

# INTRODUCTION*

This chapter provides some basic information on the response of biological entities to foreign materials. Topics include adhesion of biomolecules, or cells to synthetic materials of various sizes, methods of evaluation, and effects of nanoparticles on central nervous systems.

## 1.1. Materials and the human body

Materials are extensively used in the human body for temporary and long-term applications. Such materials are identified as biomaterials. Although the term biomaterials was introduced approximately 50 years ago (1), the use of synthetic materials for medical applications dates back many centuries. Evidence shows the use of materials in medicine dates back over 2000 years by the Aztecs, Egyptians, and Greeks (1, 2).

Metals (3-6), polymers (7-9), ceramics (10-12), composite materials (13-15), and more recently nanomaterials (6, 16-21) are used in the body for a broad range of applications. Some applications are intended to: regain function (heart valves, ocular

---

This dissertation follows the style of the *Proceedings of the National Academy of Sciences of the United States of America.*

* Part of the information reported in this chapter is reprinted with permission from "*In vivo* observation of gold nanoparticles in the central nervous system of *Blaberus discoidalis*" A Rocha, Y Zhou, S Kundu, JM Gonzalez, SB Vinson, H Liang. *Journal of Nanobiotechnology*, 9 (1):5-13. Copyright 2011 by BioMed Central.

implants, and prosthetic devices), relieve pain (artificial joints and drug delivery), or for aesthetic reasons (dental implants and contact lenses) to name a few.

Modern biomaterials have been far improved from what they were 2000 years ago. Nowadays, biomaterials are engineered for specific applications or to induce specific reactions in the body. Some materials are designed to enhance cell growth (22-24), to withstand the corrosive body environment (25-27), or to provide structural support (28-30). These are just a few in a vast number of examples.

Independent of the application is the fact that the synthetic materials interact with the biological materials found in the body, namely tissues, cells, proteins and amino acids depending on the application of interest. Needless to say, the biomaterial interaction with the body is a surface/interface phenomenon.

The degree of interaction at the material/biomolecule interface depends greatly on the application. For example, material/biomolecule interaction is undesirable for contact lenses. We neither want, nor expect the eye to react or adhere to the contact lens. On the other hand, a permanent implant, such as an artificial joint, must interact with the cells and tissues surrounding it to guarantee its success. So the most important aspect to study material/biomolecule interaction is to understand its need and expected outcome.

The first question that must be addressed is how does the body respond when a foreign material is introduced? The answer to this question is far from simple. Chemists, chemical engineers, material scientists, mechanical engineers, surface scientists, bioengineers, biologists, and physicians have been studying it for many years (2, 6). In

this work, we will focus on the material/biomolecule study from an engineering and materials science point of view.

The material/biomolecule interaction has been widely studied. It is well known that within seconds of material implantation, proteins are adsorbed onto the materials' surface. Protein adsorption aids in material incorporation into the body. Therefore, the adsorption of proteins onto the surface of biomaterials has been studied for decades. Once the layer of proteins forms around the material, the tissue cells begin to agglomerate around the protein layer and attach to the surface. Moreover, the cellular adhesion significantly affects their behavior and normal function. This tells us two things. First, that cell adhesion is an important aspect of foreign material incorporation and second, that protein adsorption and interaction with the material significantly affects the cell interaction and behavior.(2, 6) Figure 1 shows the initial body's response to foreign materials its observed time-scales.(2)

The next question that must be addressed is how can we study the interaction mechanisms? What should we be looking for at the material/biomolecule interface? The interaction greatly depends on the material scale. Bulk materials are expected to interact with cells and whole tissues while nano materials will interact mainly with proteins and amino acids.

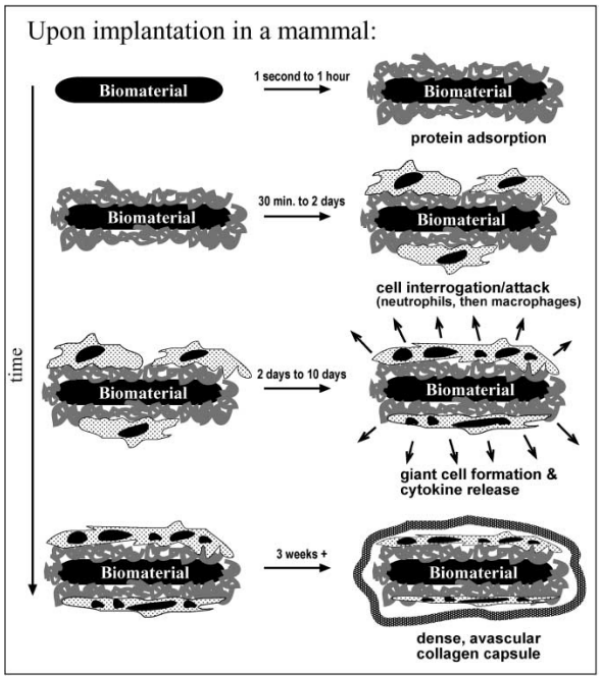


Figure 1 Body response to biomaterials (2)

## 1.2. Bulk material/cell interaction studies

The interaction of biomolecules with bulk materials is greatly dependent on their adhesion because it is what mediates cell function (31-37). Therefore, measuring cell adhesion to bulk materials is essential to study their interaction mechanisms. Quantifying cell-material adhesion has been one of the most importuned steps in improving biomaterial performance (38). Given the nature of the material/biomolecule interaction for the bulk-sized material, it is of utmost importance to study the materials' interaction mechanisms with a cell network instead of individual cells (39, 40).

Material's surface chemistry and surface roughness have been identified as the main factors affecting biomolecule adhesion (41). Therefore, quantifying the effect of materials' chemistry and surface roughness on cell adhesion is essential. Quantifying

cellular adhesion and protein interaction with nanomaterials is a key factor into predicting and potentially controlling their behavior *in vivo*.

Using fluid flow to study the detachment of cells from the surface is widely used (33, 42-51). Although previous work provides great insights into rotational flow design and cell response, quantifying the material/biomolecule adhesion strength has not been the main focus. Additionally, few systems can be used to compare the strength of adhesion between many different materials and/or biomolecules.

### 1.3. Bulk material/protein interaction studies

The human body is an amazing and complex machine. For centuries, men have been in the search to understand how it works. It is extraordinary to know that all body functions are due to well balanced protein interactions. Proteins are present in the body by the billions and their function controls even the simplest of tasks in the body. Proteins are organic macromolecules whose building blocks are called amino acids (6). Proteins control all cell functions including cell-cell and cell-foreign material interactions (52).

For decades, there has been an interest in understanding how proteins adsorb onto materials in bulk. This process is generally represented with an adsorption isotherm (53-55). The adsorption isotherm is a parameter that indicates the interaction between proteins and a biomaterial. It is traditionally used for protein / bulk polymer pairs.

The adsorption isotherms are equations that represent how likely proteins are to interact with a surface. This value strongly depends on the concentration of proteins; i.e. if there are more proteins available, there would be a thicker layer of proteins that accumulate around a material. However, there is a limit to how many proteins can be

adsorbed on the surface of a material so the curve plateaus. This type of equation or relationship is independent of temperature and it is simply called an isotherm due to its characteristic curve (see Figure 2).

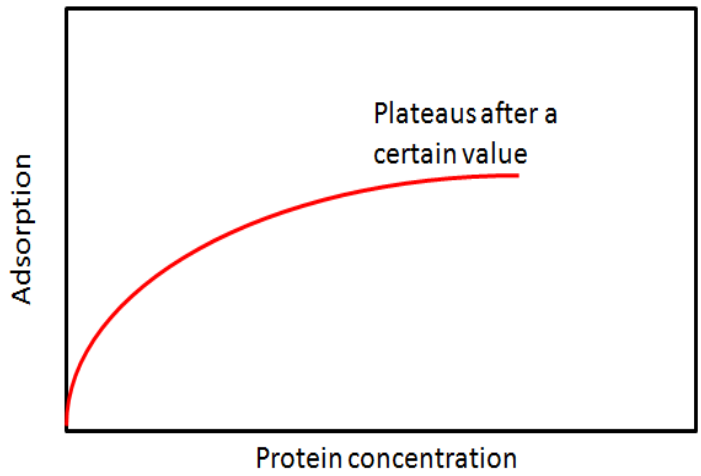


Figure 2 Protein adsorption onto a surface depends on protein concentration. The plateau indicates the concentration of the protein monolayer

There are two main models used to represent the protein/biomaterial adsorption, the Langmuir and the Freundlich models. The Langmuir model was developed for gasses but it has been adapted to protein/polymer pairs with great success (53). The Langmuir equation is:

$$C_s \frac{\mathrm{g}}{\mathrm{cm}^2} = \frac{M}{AN_A}\left(\frac{KC_b}{1+KC_b}\right) \quad [1]$$

where $C_s$ is the protein adsorption on the surface in g/cm$^2$, $M$ is the protein's molecular weight, $K$ is an equilibrium adsorption constant, $C_b$ is the grams of protein per mL of solution, $A$ is the area and $N_A$ is Avogadro's number (53). The value of $K$ depends on the material/protein pair.

The second common equation to represent the protein adsorption isotherm is the Freundlich adsorption isotherm (53). This however, is an empirical relation of the form:

$$C\,\frac{\mathrm{g}}{\mathrm{cm}^2} = \mathrm{K}(\mathrm{C_b})^{1/\mathrm{n}} \qquad [2]$$

In this equation, $C$ is the surface protein concentration in g/cm$^2$, $C_b$ is the concentration of protein in the solution, $K$ depends on how likely a surface is to adsorb protein and n in the intensity of adsorption (53). Specific values for $K$ and $n$ for any given protein/material pair must be found experimentally.

Another method for identifying the protein/material interaction is to quantify its potential energy (54). The total potential energy is the result of the primary and induced electrostatic energies, the dispersive attraction and repulsion (54). The accuracy of the calculated potential energy depends greatly on the amount of proteins present in the system and the distance between proteins. Protein quantification and equilibrium distance measurements are challenging.

Moreover, these models do not predict the strength of the material/protein interaction. The models simply analyze how likely the protein is to be attracted to the materials' surface.

### 1.4. Nanomaterial/protein and amino acid interaction studies

Nanomedicine is an exciting emerging field that utilizes nanomaterials to help reach places that traditional medicine does not allow. Nanomaterials are widely studied for medical applications and have successfully been used for imaging and targeted drug

delivery (20, 21, 56-58). It has been established that nanomaterials are those with at least one dimension <100nm.

Until now it is known that when materials are introduced into the human body, proteins will surround the material in an attempt to incorporate it. This protein adsorption is also true for nanomaterials (59-62).

In a recent study, Cheng and colleagues successfully demonstrated that a PEG/ gold nanoparticle was faster and more effective as a drug carrier to treat cancer bearing mice than the pure drug (63). The results indicate an effective drug delivery within two hours and the tumors receded within one week (63). The results show success but not much detail is provided as to how this PEG/gold nanoparticle moves through the blood stream to the tumor site.

Others, like Chithrani and Chang have a step further into understanding the nanoparticle uptake by cells; i.e. how nanoparticles get into and out of cells (64). Most importantly, how particle size and surface treatment (by protein coating) affects the time it takes for nanoparticles to enter and exit the cell (64). These results provide a better understanding about the nanoparticle size effect and its interaction with proteins. More importantly, how these will affect the behavior and normal function of the cells.

To date, research has been focused on identifying the applicability and efficacy of nanoparticles for drug delivery and also how surface treatments make the nanoparticle more or less likely to interact with cells. But do nanoparticles have a preference to which proteins they interact with? What dictates this preference? Most importantly, can we predict this interaction?

In addition, the surface of the nanomaterials must be functionalized to guarantee interaction with specific biomolecules once they are injected (65). Functionalization is a process where molecules are attached to the nanoparticles' surface to ensure its interaction with specific tissues. In addition, nanoparticles can be functionalized with the drug that needs to be delivered.

Nanoparticles for drug delivery and imaging are generally introduced to the body via the blood stream (63). Studying the effect that functionalized nanomaterials will have on blood flow is a question that deserves attention. Nanofluid research has demonstrated how the viscosity significantly increases with the addition of nanoparticles (66-69) as demonstrated by Prasher et al. and shown in Figure 3. Based on the effect that nanoparticles have on viscosity of fluids, increased pumping power is required (70). This presents a potential risk to the body.

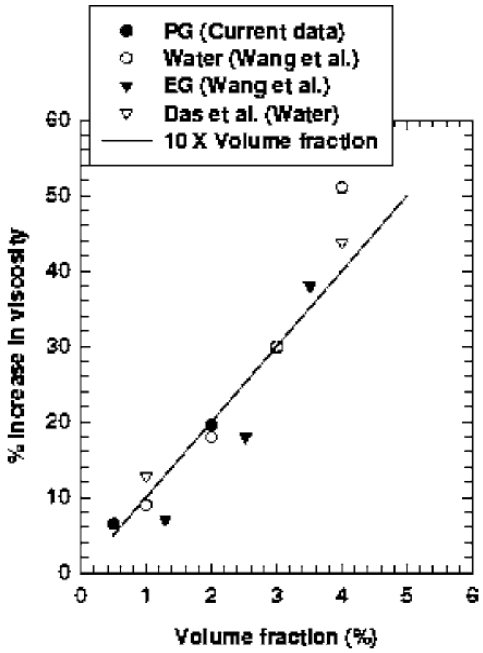


Figure 3 Effect of nanoparticle volume fraction on nanofluid viscosity (67)

The flow properties of the nanomaterial/biomolecule solution must be studied to assess the risk. The system under study gets very complicated given that nanomaterial-nanomaterial, nanomaterial-protein, and protein-protein interactions are expected. This is without considering the effects of the functional group attached to the nanomaterials' surface.

Furthermore, research has shown that some solvents affect the conformation of proteins and amino acids in solution (71, 72). This can cause a significant change in the viscosity and structural integrity of the solution.

### 1.5. *In vivo* nanomaterials and the CNS

Nanomaterials have been successfully used for medical applications. The nervous system could greatly benefit from nanomedicine. Nanomaterials can reach places that traditional medicine does not allow. The work of Provenzale and colleagues has demonstrated the use of nanomaterials for imaging of the nervous system (73). Bagley discusses in great detail the possible methods of drug delivery to the nervous system with nanoparticles as the drug carriers (74).

Common biological systems, mainly mice, currently used to study, analyze, and test *in vivo* treatments for neuron damage and repair are expensive and many times difficult to maintain. It is necessary to find a suitable biological system that is inexpensive, easy to maintain, and handle. As early as in 1990, Huber et al. reported cockroaches as good candidates for neurobiology studies (75). This idea was later applied by Scharrer for endocrine studies (76). There are reports proving the similarities between vertebrate and invertebrate brains (77). In particular, non-vertebrate systems such as

cockroaches were ideal models for neurotoxicology studies (78). The comparison between invertebrate (like cockroaches) and vertebrate (like mice) has been made in terms of their behavior, anatomy, biology, and physiology. Invertebrate subjects are not only cost effective and readily available, but also they do not feel pain (79). This opens new avenues for experimental protocols and controls currently implemented in vertebrate animals and humans.

Cockroaches have been used as model systems for neurological research. Early neurobiology cockroach research has been focused on octopamine and serotonin response in the nervous system (NS). Previous studies were to observe how chemicals were distributed in the brain and how they affected the nervous system (80, 81). In more recent work by Brown et al., roaches were used to study how age affects memory and brain integrity (82).

Perhaps nanomaterials can be used to repair a damaged nerve, a very difficult task with current technology, but at what cost? The effect of the functionalized nanomaterial on the communication channels of the nervous system is a subject that deserves attention. Using the cockroach as a system of study will help find the answer.

# CHAPTER II

## MOTIVATION AND OBJECTIVES

The most important objective of this research is to comprehend how materials and biomolecules interface at the bulk and nanometer length scales. Polymers, metals, and ceramics have been used in the body for many applications. Independent of its application is the fact that these materials have to interact with the cells and proteins in the body. The main questions this research wants to address are why their interaction is important and how they interact.

For the long-term applications of bulk materials, like artificial joints, it is necessary that the tissues surrounding it recognize the implant's surface as part of the body. If there is poor interaction (i.e. poor adhesion) at the material/tissue interface, the tissue's behavior will be significantly affected causing tissue death. For nanomaterials, which are mainly used for imaging and drug delivery systems, it is necessary to understand how these functionalized nanoparticles will interact with the body. Nanoparticles are usually delivered through the blood stream and the effect they have on the flow properties must be addressed.

In order to understand the interaction mechanisms at the biomolecule/material interface this work will address the following objectives:

1. Develop a methodology to quantitavely evaluate the interactions of cells and proteins on a material's surface and identify the main factor affecting adhesion: materials chemistry or surface roughness.
2. Obtain fundamental understanding in effects of fluid shear on cell adhesion. Mainly, to quantify the strengthening mechanisms of the cells when externally stimulated by the applied flow.
3. Quantify changes in viscosity of protein and amino acid solutions when mixed with nanoparticles and estimate the potential energy change due to their interaction.

Experimental and analytical approaches will be used for this research. Figure 4 is the summary of the proposed work flow representing different length scales. The biomolecules / material interaction study will be separated into materials at two scales. The first approach will be to study how cells and proteins adhere to materials in bulk. The second is for materials in the nanometer scale. For this work, the effect of adsorbed proteins on gold nanoparticles will be analyzed. The effects that nanoparticle size, concentration and surface charge have on the flow properties of protein solutions will be studied. To obtain better understanding of the preference and interaction of specific proteins to nanoparticles, the biomolecules will be further simplified by analyzing the effects of nanoparticles on amino acid solutions.

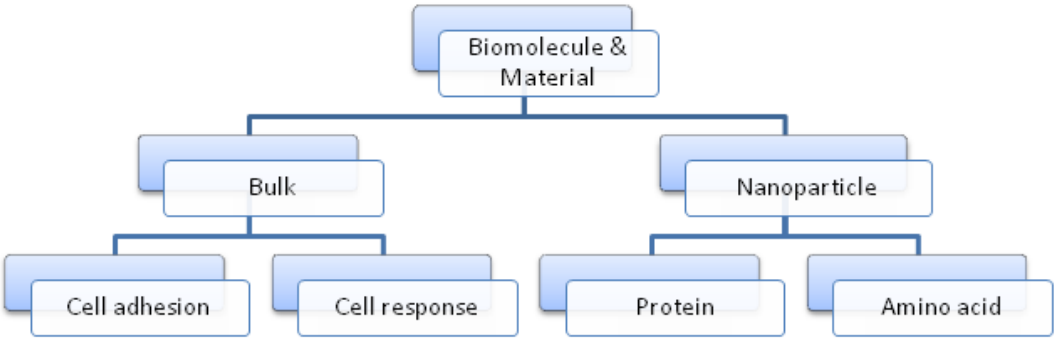


Figure 4 Proposed work flow

We will conclude this research by analyzing the *in vivo* interactions of charged gold nanoparticles on the central nervous system of the cockroach. Such understanding would help us predict nanoparticle behavior *in vivo* and would help identify the insect as a viable system for nanomedicine studies.

# CHAPTER III

## METHODOLOGIES*

In this chapter, all materials and methods used are described. The first part introduces the biomolecules: 3T3 Swiss mouse fibroblasts, 12-day-old chick embryo neurons, egg-white protein, bovine serum, L-arginine, L-lysine, L-aspartic acid, and L-glutamic acid. The materials at two scales: bulk (poly-carbonate, poly(methyl methacrylate) and poly-D-lysine coated glass) and nano (negatively and positively charged gold nanoparticles). The second part discusses a methodology developed in this research using a rheological approach. Finally, characterization techniques used are described. The techniques used to obtain material properties include: surface roughness, contact angle, EDS, and XRD and for physical properties: digital microscope, confocal microscope, SEM, TEM, AFM, XPS, and hyperspectral imaging.

---

* Part of the information reported in this chapter is reprinted with permission from "Critical fluid shear stress analysis for cell–polymer adhesion" A. Rocha, M. Hahn, H. Liang, 2010. *Journal of Materials Science,* 45 (3)**:** 811-817, Copyright 2010 by Springer/Kluwer Academic Publishers and from "Neuron adhesion and strengthening" A. Rocha, K. Jian, G. Ko, H. Liang, 2010. *Journal of Applied Physics*, 108 (2): 024702-024706, Copyright 2010 by American Institute of Physics and from "*In vivo* observation of gold nanoparticles in the central nervous system of *Blaberus discoidalis*" A. Rocha, Y. Zhou, S. Kundu, J.M. Gonzalez, S.B. Vinson, H. Liang, 2011. *Journal of Nanobiotechnology*, 9 (1): 5-13 Copyright 2011 by BioMed Central.

## 3.1. Materials

### 3.1.1. Bulk materials

The materials used for bulk-scale interaction include: polymers, glass, and metallic coatings. The interaction of these materials with cells and proteins is studied.

#### 3.1.1.1. Polymers

Poly(methyl methacrylate) (PMMA) and polycarbonate (PC) were the two polymeric materials selected. PMMA is used as dental cement (83) and PC is used for renal dialysis as for surgical instruments (84). The substrate materials were cut into 3 x 3 $cm^2$. The samples were cleaned by rinsing in ethanol followed by air-drying in a laminar flow hood. They were then sterilized by shortwave UV irradiation for 24 hours in a laminar flow hood. The samples were placed in a sterile 6-well culture dish (Falcon). The surface roughness and contact angle of the PC and PMMA substrates were measured before and after sample preparation. The repeat unit of the PC and PMMA are shown in Figures 5 and 6 respectively. A summary of their properties is given in Table 1.

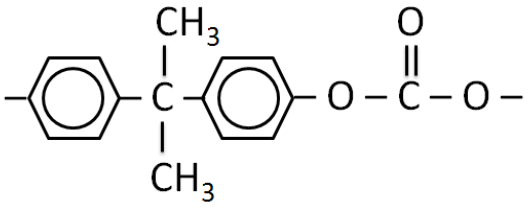


Figure 5 PC repeat unit

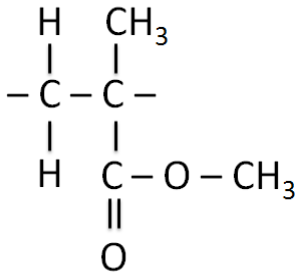

Figure 6 PMMA repeat unit

Table 1 Properties of PC and PMMA

| Material | Tg (°C) | Tm (°C) |
|---|---|---|
| PC | 150 | 267 |
| PMMA - atactic | 105 | 160 |

### 3.1.1.2. Protein coated glass

Glass is a standard material used in cell culture studies. The glass must be coated with protein to ensure interaction. The 25mm diameter glass coverslips (Carolina Biological Supply Co.) were coated with poly-D-lysine (Sigma, St. Louise). The molecular structure of the poly-D-lysine is shown in Figure 7. The properties of the sample are summarized in Table 2.

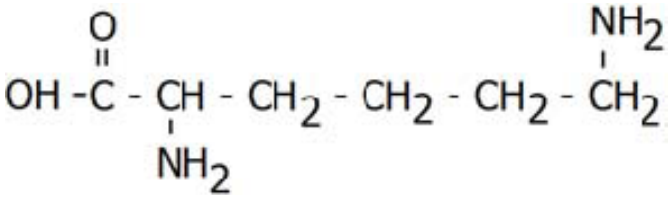

Figure 7 Repeat unit of D-lysine

Table 2 Properties of poly-D-lysine coated glass

| Material | Property | value |
|---|---|---|
| Glass | Ra (μm) | 3 ± 1.2 |
| D-Lysine solution | pH | 8.4 |

### 3.1.1.3. Metals

Titanium (Ti) alloy and cobalt-chrome (CoCr) alloys are widely used in high wear biological applications. Unfortunately, wear is still an issue. Four coating materials were selected as potential candidates to decrease surface wear in biological applications: TiN, TiAlN, CrN, and CrAlN. Two substrates were used: Si and Ti. The (111) Si wafer was used as received with no further surface treatment. The Ti alloy samples were mechanically polished with 600 grit-sandpaper and with polishing cloth and 5, 3.5, and 1nm diamond particle polishing paste to reach an average surface roughness (Ra) of 150nm and 30nm respectively. The materials and targeted surface roughness are indicated in Table 3.

Table 3 Summary of selected materials, target surface roughness and polishing method

| Substrate | Target Ra (nm) | Treatment to achieve Ra |
|---|---|---|
| (111) Si | 3nm | used as received |
| Ti smooth | 30nm | Polished with 200, 400, 600, 800, 1000 and 1200 grit sandpaper and polished with 5, 3, and 1nm diamond paste on polishing cloth |
| Ti rough | 150nm | Polished with 200, 400, and 600 grit sandpaper |

The coatings were prepared by asymmetric bipolar pulsed reactive magnetron sputtering under a high purity nitrogen environment. The samples were ultrasonically cleaned in acetone twice for 10 minutes, once in ethanol for 10 minutes and forced air dried prior to coating. The pressure was set at $8 \times 10^{-4}$ Pa. The leak rate was below $5 \times 10^{-2}$ Pa/s. Argon gas was used to ignite the arcs, its flow rate was constant. The substrates were mounted on rotating fixtures at 200mm from the targets (85, 86).

The coating material and surface roughness were selected to identify the most important factor in protein adhesion: chemistry of the coating material or surface roughness. Furthermore, two substrates were selected to identify if the substrate material had any effect on protein interaction.

### 3.1.2. Nanomaterials

Nanomaterials are widely investigated for medical applications. Gold is one of the main materials used in nanomedicine (87-89). Gold nanoparticles must be functionalized to enhance its interaction with specific cells or proteins.

The gold nanoparticles used in this work are assembled with a bottom up approach using gold seeds. These particles absorb a 510nm light wave and emit at 560 nm (90-92). This allows for fluorescent and spectral imaging to identify the presence of nanoparticles embedded in biomolecules without adding fluorescent tags.

The synthesis of gold nanoparticle seeds is as follows: 250µl of 0.01 M $HAuCl_4$ solution was added to 10ml of 0.1 M CTAB (Cetyltrimethylammonium bromide) solution while stirring. Then 0.60 ml of 0.01 M sodium borohydride was added. This forms a

brown-yellow solution. The solution was vigorously stirred at 25 °C for 2min. This process yields spherical gold seeds with approximately 4nm diameter.

#### 3.1.2.1. Negatively charged gold nanoparticles

The Turkevich wet chemical method was used to synthesize the gold nanoparticles (93). The Au particles are suspended in DI water by the negatively charged tri-sodium-citrate molecule (i.e. citrate) (93). The chemical composition of citrate is shown in Figure 8. The target nanoparticle sizes for this study were 10, 20, and 50 nm.

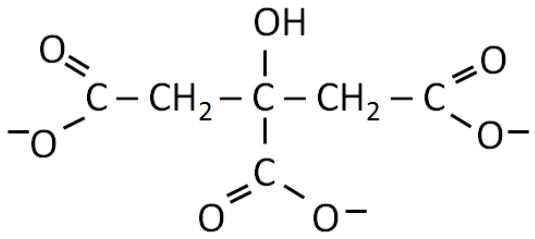


Figure 8 Citrate repeat unit

Briefly, the ingredients were prepared before nanoparticle synthesis. Hydrogen tetrachloroaurate tri-hydrate, tri-sodium citrate dihydrate (both from Sigma-Aldrich), and de-ionized (DI) water were used to make the nanoparticles. The gold precursor is hydrogen tetrachloroaurate tri-hydrate. Tri-sodium citrate dihydrate solution controls the particle growth. Tri-sodium citrate is the reducing and stabilizing agent for the gold particle formation (93).

The 1.25 mL of aqueous gold chloride with a concentration of $10^{-2}$ (M) was mixed with 48.35 ml of de-ionized water. The resulting mixture was heated to 80 °C while being magnetically stirred. The 1 wt% of tri-sodium citrate solution was slowly added while

continuously stirring and heating. The amount added depends on the targeted nanoparticle size. The solution color depends on the nanoparticle size. Once the solution turned wine-red, the solution was stirred for another 10-15 minutes. The nanoparticle concentration can be controlled by addeing more DI water. Typically, DI water was added to complete 50mL. The particle's size depends on the volume of citrate solution in the reaction mixture (93).

Figures 9 to 11 show the actual particle size distribution for the negatively charged gold nanoparticles used in this study. The average nanoparticle diameters are 13.8 ±1.1 nm, 20.0 ±3.1 nm, and 43.9 ±5.2 nm for the solutions labeled 10, 20, and 50nm respectively.

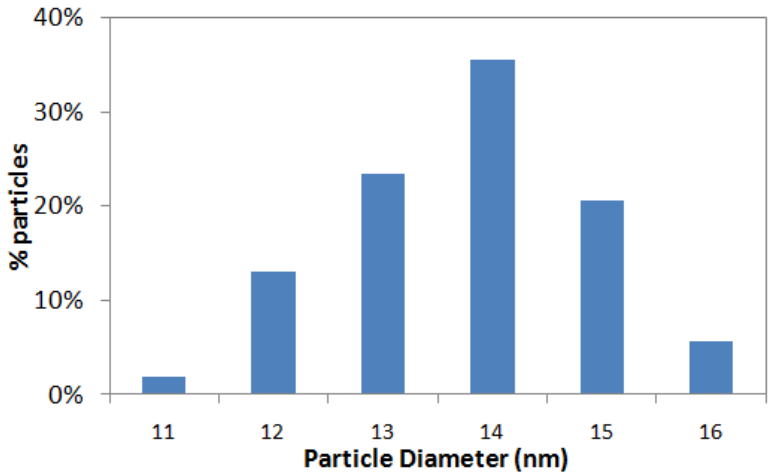


Figure 9 Particle size distribution for the negatively charged gold nanoparticles labeled as 10nm. The average size is 13.8 ±1.1 nm

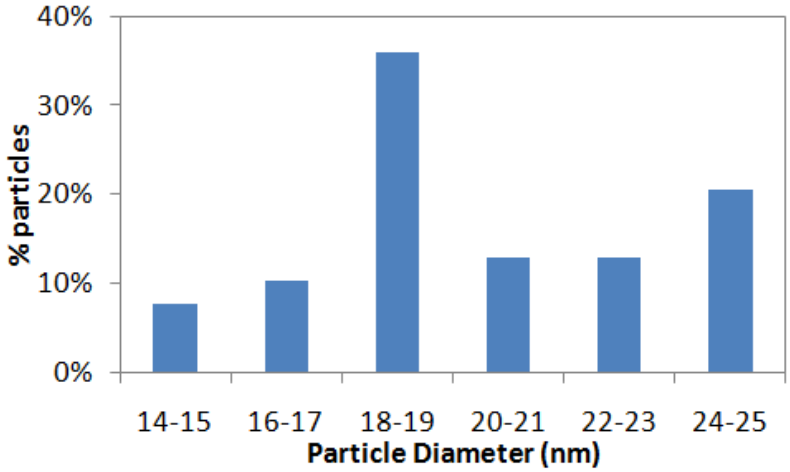


Figure 10 Particle size distribution for the negatively charged gold nanoparticles labeled as 20nm. The average size is 20.0 ±3.1 nm

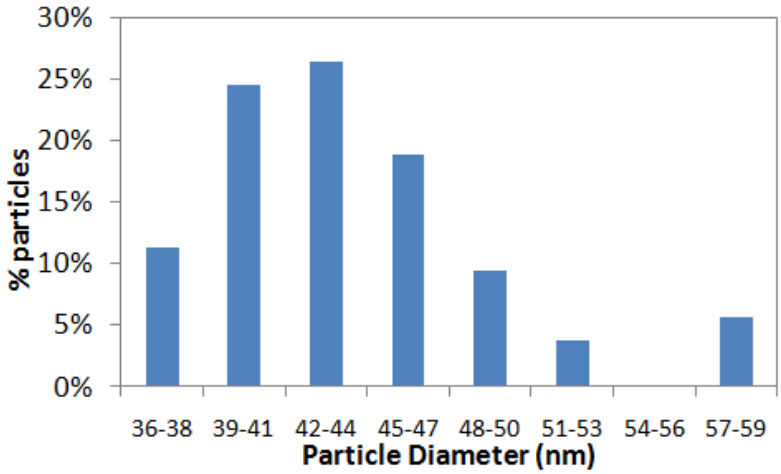


Figure 11 Particle size distribution for the negatively charged gold nanoparticles labeled as 50nm. The average size is 43.9 ±5.2 nm.

### 3.1.2.2. Positively charged gold nanoparticles

Two surfactant materials are used to achieve different nanoparticle sizes. poly(allylamine hydrochloride) (PAH) is used to fabricate 20nm size nanoparticles while Cetyltrimethylammonium bromide (CTAB) is used to fabricate other sizes. The

nanoparticle size will depend on the concentration of PAH or CTAB and gold in the solution. The molecular structure of PAH and CTAB are given in Figure 12.

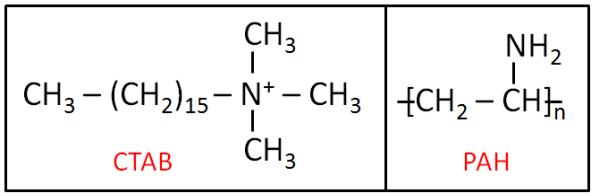


Figure 12 Molecular structure of CTAB and PAH

To make the 10 and 50 nm diameter nanoparticles, three growth solutions are needed for seed-mediated growth steps. Solutions A and B had 0.25 mL of chloroauric acid at a concentration of 0.01 M, 0.05 mL of 0.1M sodium hydroxide, 0.05 mL of ascorbic acid with a concentration of 0.1M, and 9 mL of CTAB solution with a concentration of 0.01 M. Solution C had 2.5 mL of chloroauric acid at a concentration of 0.01 M, 0.50 mL of sodium hydroxide at a concentration of 0.1 M, 0.50 mL of ascorbic acid with a concentration of 0.1M, and 9 mL of CTAB solution at a concentration of 0.075 M. Nanosphere formation started by mixing solution A to 1 mL of gold seed. The mixture was allowed to set for five minutes, then 1 mL of the new mixture was added to solution B. The new mixture was allowed to set for another five minutes and was then mixed with solution C. After 30 minutes, the final solution changed from clear to deep magenta-purple. Excess CTAB solution was removed by centrifuging the solution and resuspended in DI water to control the nanoparticle concentration.

The 20 nm nanoparticle was made with PAH surfactant. Details of this process have been published elsewhere (94, 95). Briefly, the PAH solution was prepared by

dissolving 0.1 wt% PAH in ultra pure distilled water. The solution was stirred for 10 hours while protected against light. Then 5 mL of 0.1wt% PAH solution was added to 200 µL of chloroauric acid at a concentration of 0.01 M. The resulting solution was stirred for 2–3 min. The solution was heated for 30–60 s in a microwave in 10 s intervals (94, 95). The resulting solution is stable for over six months when stored at standard temperature and pressure.

Figures 13 to 15 show the actual particle size distribution for the positively charged gold nanoparticles used in this study. The average nanoparticle diameters are 8.18 ±2.1 nm, 26.8 ±4.4 nm, and 49.2 ±3.3 nm for the solutions labeled 10, 20, and 50nm respectively.

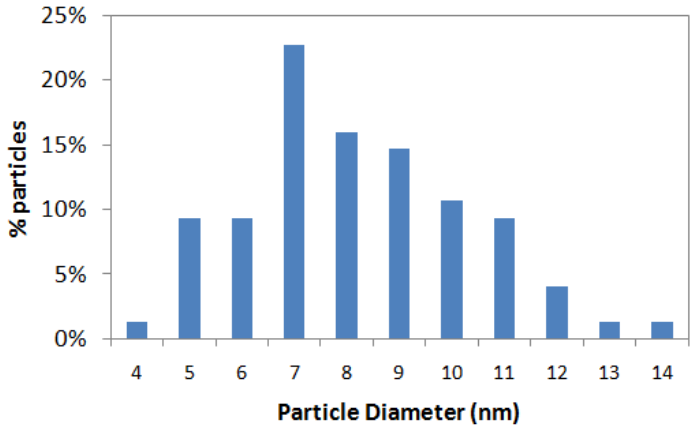


Figure 13 Particle size distribution for positively charged gold nanoparticles labeled as 10nm. The average size is 8.18 ±2.1 nm

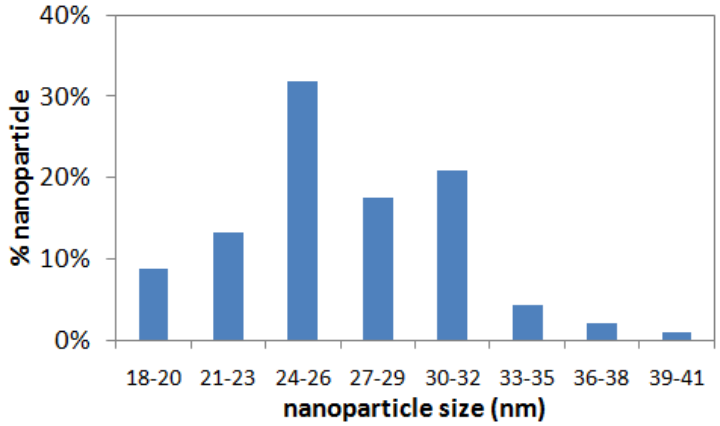


Figure 14 Particle size distribution for positively charged gold nanoparticles labeled as 20nm. The average size is 26.8 ±4.4 nm

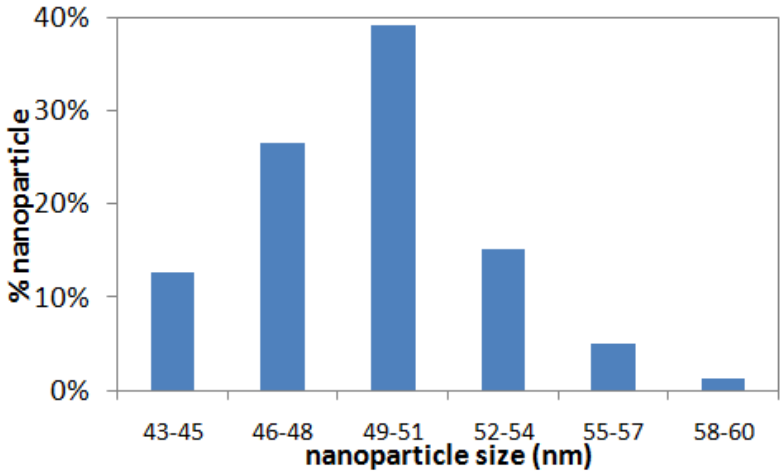


Figure 15 Particle size distribution for positively charged gold nanoparticles labeled as 50nm. The average size is 49.2 ±3.3

### 3.1.3. Biomolecules

In this work, biomolecules refers to any cell, protein, and amino acid. Cells and proteins are studied for their interaction with bulk materials while proteins and amino acids are studied for their interaction with nanomaterials.

#### 3.1.3.1. Cells

Two cell types were used in this study, 3T3 Swiss mouse fibroblasts and 12-day-old chick embryos. The cells used in this study were cultured 24 hours prior to adhesion testing for consistency and to ensure cell stability and adhesion. A minimum of 60% surface coverage by cells was required for testing.

##### 3.1.3.1.1. 3T3 Swiss mouse fibroblasts

The sample preparation has been discussed in detail (39). Briefly, NIH/3T3 fibroblasts (ATCC) were expanded in cell culture media (Dubelcco's Modified Eagles Medium with 10% bovine calf serum and penicillin/streptomycin) and maintained at 37$^{o}$C in 5% $CO_2$. All cell culture reagents were obtained from Cell Applications unless otherwise stated. Cells at passage 9-12 were harvested from T75 cell culture flasks and pelleted by centrifugation. The cells were resuspended in fresh cell culture media and counted using a hemacytometer. Cells were then seeded on each substrate at 5,000 cells/cm$^2$. Cell density on the sample was verified by cell count after 2 and 24 hours of seeding.

Immediately prior to testing, the cell culture media was exchanged with physiological phosphate buffered saline (PBS). All tests were performed with a controlled maximum shear stress at 37$^{o}$C. Two cell cultured samples of each material were tested and measurement was repeated for at least six times. The sample-to-spindle gap was set to 480μm. Samples were tested at the applied shear for 10 minutes. The applied shear stabilizes after 2 minutes.

Cells were fixed immediately after testing. The samples were immersed in formalin for 24 hours to fix the cells. The fixed samples were dehydrated in graded ethanol baths for scanning electron microscopy (SEM). Formalin was used as a fixative to prevent the cells from moving. Subsequently, samples were sputter-coated with gold and imaged with a JEOL JSM-6400 Scanning Electron Microscope.

#### 3.1.3.1.2. 12-day old chick embryo neurons

Retina neurons (bipolar neurons) were extracted from 12-day-old chick embryos. Chick retinas from fertilized eggs (*Gallus gallus,* Poultry Science Department at Texas A&M University) were dissociated at embryonic day 12 (E12). Cells were incubated at 39$^{o}$C and 5% $CO_2$ for 24±1 hours prior to testing to ensure adhesion and allow the culture to stabilize. A 60% cell confluence, substrate surface coverage by cells, was required for testing.

The distance between plates was set at 500μm. Each test was conducted under a constant shear stress and the duration was set for 10 minutes. All tests were conducted at 39$^{o}$C, which is the incubation temperature for chick embryos. The main goal was to observe and quantify the cell strengthening mechanisms. Therefore, the cultured neurons were tested at increasing values of maximum shear stress ($\tau_{max}$). The $\tau_{max}$ ranged from 10 to 70 dynes/cm$^2$ with 15 dynes/cm$^2$ increments. Each test was confirmed 3 times. The samples were fixed with Zamboni's fixative (Newcomer Supply) immediately after testing for 10 minutes, rinsed 3 times with DPBS for 5 minutes, and allowed to air dry before imaging.

#### 3.1.3.2. Proteins

Albumin is the most abundant protein found in the body. Egg-white protein and bovine serum are rich in albumin (96-98). Egg-white protein was used for adhesion studies to bulk materials while bovine serum was used to study the interaction mechanisms with nanomaterials.

##### 3.1.3.2.1. Egg-white protein

An amount of 0.3 g of egg-white protein (Sigma Aldrich) was dissolved in 10mL of DI water. The coated samples were ultrasonically cleaned in acetone and DI water for 10 minutes each prior to protein coating. A protein solution of 0.200 mm thickness was applied to the sample's surface (volume depended on the sample's surface area) and allowed to dry for 12 hours in a desiccator at room temperature. All DI water evaporated leaving a thin, well-adhered, egg-white protein layer on the surface.

##### 3.1.3.2.2. Bovine serum

Bovine serum (Hyclone – Fischer Scientific) was separated into ~300mL glass vials for easy storage at -4$^{o}$C. The small vials also help to defrost small quantities as needed. The serum was vigorously stirred for 5 minutes prior to each use to avoid sedimentation. The composition of bovine serum is shown in Table 4.

Table 4 Composition of bovine serum (99)

| PROTEINS/OTHER | Concentration | TRACE METALS/IRON | Concentration |
|---|---|---|---|
| Albumin | 3.2 gm% | Calcium | 10.9 mg/dL |
| Alkaline Phosphatase | 225 mU/mL | Chloride | 101 mEq/L |
| Blood Urea Nitrogen | 5 mg/dL | Inorganic Phosphorus | 9.1 mg/dL |
| Creatinine | 1.3 mg/dL | Iron | 469Ug/dL |
| Gamma Globulin | 12.8 % tp | Percent Saturation (Iron) | 81% |
| Glucose | 81 mg/d | Potassium | 6.0 mEq/L |
| Glutamic Oxaloacetic Transaminase(SGOT) | 134 mU/mL | Sodium | 142 mEq/L |
| Glutamic Pruvic Transaminase (SGPT) | 41 mU/mL | Total Iron Binding Capacity (TIBC) | 581 ug/dL |
| IqG-Nephelometer | 14.5 mg/mL | | |
| Lactase Dehydrogenase | 4820 mU/mL | | |
| Osmolality | 296 mOsm/Kg | | |
| Total Bilirubin | 0.4 mg/dL | | |
| Total Protein | 6.9 gm% | | |

### 3.1.3.3. Amino acids

Amino acids are the building blocks of proteins. There are positive, negative, and neutral amino acids which are made of C, H, N, and O mainly. Amino acids have a general backbone structure of $CH_2$, have one carboxyl group (COOH), one amine group ($NH_2$), and one functional group, which what makes it positive, negative, or neutral (6, 100, 101).

L-lysine, L-arginine, L-glutamic acid, and L-aspartic acid are the four amino acids selected for this study. These are four main components in albumin protein (102). Two amino acid concentrations were prepared: one at 0.01M (mol/L) and one at 0.0001 M. The 0.0001 M solution was prepared by diluting 1mL of the 0.01M in 100mL of DI water.

#### 3.1.3.3.1. L-lysine

Lysine is a positively charged amino acid. Figure 6 shows its chemical structure. The solution with 0.01M was prepared by mixing 0.0365 g of L-lysine in 20mL of DI

water. The solution was magnetically stirred for 15 minutes. The pH of the 0.01M is 7 and the pH of the 0.0001M is 8 y. Assuming a linear conformation, the L-lysine repeat unit is 1.036nm, based on the bond lengths of N-C, C-C, and C-O.

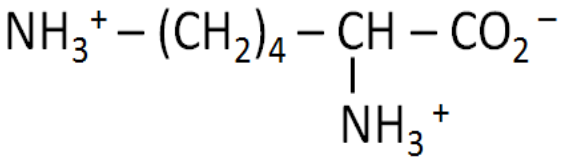

Figure 16 Chemical structure of L-lysine

#### 3.1.3.3.2. L-arginine

Arginine is a positively charged amino acid. Figure 17 shows its chemical structure. An amount of 0.0266g of L-arginine was mixed in 20mL of DI water to achieve the 0.01 M concentration. The solution was stirred for 15 minutes. The pH for both solutions is 7.5. Based on the bond lengths of N-C and C-C L-arginine has an estimated length of 1.302nm.

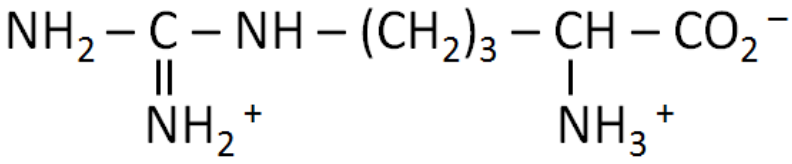

Figure 17 Chemical structure of L-arginine

#### 3.1.3.3.3. L-glutamic acid

This amino acid is negatively charged. Figure 18 shows its chemical structure. Twenty nine mg of glutamic acid were mixed in 20mL of DI water to make the 0.01 M

solution. The solution was stirred for 30 minutes. The 0.01 M solution has a pH of 4 and is more difficult to dissolve. The pH of the 0.0001 M is 7.0. Based on the bond lengths of C-C and C-O L-glutamic acid has an estimated length of 0.831nm.

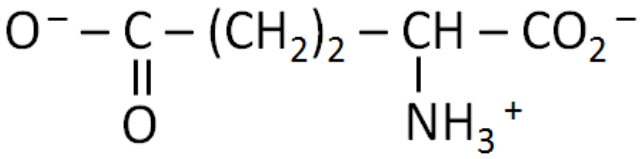

Figure 18 Chemical structure of L-glutamic acid

#### 3.1.3.3.4. L-aspartic acid

Aspartic acid is a negatively charged amino acid. Figure 19 shows its chemical structure. An amount of 0.0421g of aspartic acid was mixed in 20mL of DI water to make the 0.01 M concentration. The solution was stirred for 30 minutes. The 0.01 M solution has a pH of 4.5 and is more difficult to dissolve. The pH of the 0.0001 M is 7.5. Based on the bond lengths of C-C and C-O L-glutamic acid has an estimated length of 0.677nm.

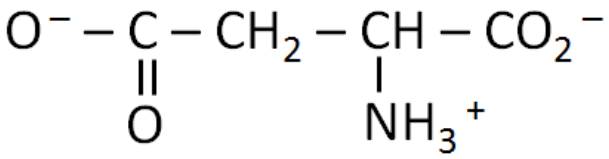

Figure 19 Chemical structure of L-aspartic acid

## 3.2. Methodology

### 3.2.1. Cell and protein adhesion to bulk materials

Over the last decades, many techniques have been developed to assess the cell's behavior when it comes in contact with a biomaterial. The method presented here offers the advantage of quantifying and comparing the strength of interaction between different cell types and different substrate materials. This technique has been proven effective for the following biomolecules: fibroblasts, neurons and with egg-white proteins. Furthermore, the technique allows to quantify and compare the strength of cell adhesion to polymeric (39) and protein coated surfaces (40) and the adhesion strength of egg-white protein with metallic, and polymeric surfaces (103).

A rheological method is developed to evaluate cell adhesion to various materials. Cell adhesion strength can be investigated using a parallel plate rheometer to apply a defined rotational shear to adhered cells, shown in Figure 20. It contains a lower fixed plate and a rotating spindle. A Peltier plate is the lower fixed plate and it is used to control the temperature from $0^{o}$C to $100^{o}$C. The fibroblasts tests were performed at $37^{o}$C, the neuron tests were conducted at $39^{o}$C and the protein adhesion tests were performed at $25^{o}$C.

The rotating spindle is controlled by a torque motor equipped with an air bearing to minimize friction and allow for accurate viscosity measurements of very light liquids. The parallel plates can be readily sterilized, and the rheometer can fit within standard laminar flow hoods. In addition, the maximum applied stress ($\tau_{max}$) is easily controlled in the rotational rheometer. The success of the test relies on a laminar flow generated by the

rotating plate. A laminar flow is one where the molecules in the flow move in smooth paths in well-defined concentric radii. A laminar flow could be obtained by controlling the density of the testing liquid, the distance between plates, and the rotational velocity of the disk. For the parallel plate rheometer, the laminar to turbulent transition occurs at a Reynold's number approximately equal to 10 (104-113).

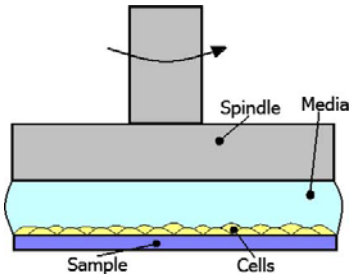

Figure 20 Diagram of parallel plate rheometer

During spindle rotation, the shear stress varies with the radial position being the highest at the maximum radius and zero at the center. The critical radius ($R_C$), shown in Figure 21, is defined as the radius at which the cell adhesion force equals to the applied shear force. At this point, the cells are removed from the surface leaving a well-defined radius, which can be used to calculate the cell adhesion in terms of the shear stress to which the authors will refer as the critical shear stress ($\tau_C$). This approach has the advantage of short test duration and low shear stress as compared to existing techniques (39). Unlike most other shear flow systems, cell shape, size, and confluency are not affected by this test method (2).

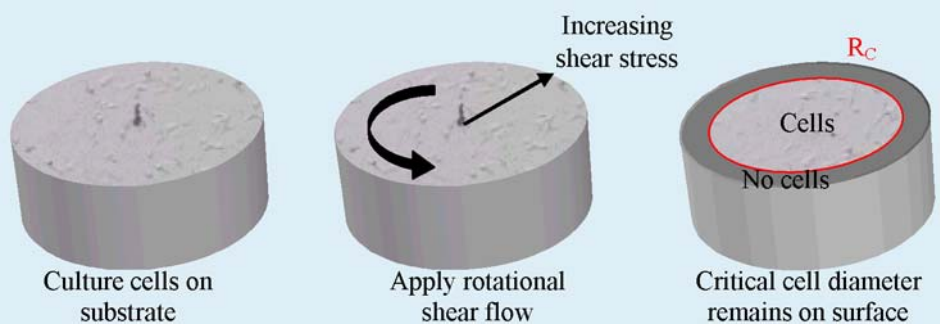


Figure 21 Diagram of cell culture sample, rotational shear flow, and interpretation of results (39)

The equations needed to calculate the $\tau_C$ are now discussed. For a Newtonian fluid undergoing non-slip rotational shear, the shear stress ($\tau$) is:

$$\tau \text{ Pa} = \frac{\eta \omega r}{z} \quad [3]$$

where η in Pa is the fluid's dynamic viscosity, the angular velocity is $\omega$, $r$ is radius and the distance between plates is $z$. Since $\omega$ reaches equilibrium within two minutes of testing and remains there for the duration of the test, we can assume $\omega$ is constant and independent of radial position. This gives that $\omega$ at the critical radius, $R_c$, must equal to $\omega$ at the spindle radius, $R_{max}$, ($\omega_{R_c} = \omega_{max}$):

$$\frac{Z}{\eta R_c} \tau_{R_c} = \frac{Z}{\eta R_{max}} \tau_{max} \quad [4]$$

The distance between plates ($Z$) and the viscosity ($\eta$) are constant for the duration of the test and can be cancelled, giving the simplified form of the equation:

$$\tau_c \text{ Pa} = \frac{R_c}{R_{max}} \tau_{max} \quad [5]$$

Equation 5 relates the observed critical radius to the critical shear stress and the equation can be used to calculate the shear tress of cell or protein adhesion to a bulk material. This equation is used to calculate the $\tau_C$ of Swiss mouse fibroblasts to polymeric materials, the $\tau_C$ of 12-day-old chick embryo neurons to poly-D-lysine coated glass, and the $\tau_C$ of egg-white protein to metallic coatings.

The main goal of this work is to identify the interaction mechanisms at the biomolecule and material interface and to identify the main factors affecting this interaction.

### 3.2.2. Protein and amino acid interaction with nanomaterials

Nanoparticles are widely researched for drug delivery and imaging applications with promising results (20, 21, 56, 65, 73, 114-117). The nanoparticles must be functionalized to guarantee interaction with specific proteins for imaging or functionalized with the drug they will deliver. These nanomedicines are usually delivered through the blood stream. However, nanofluid research has shown us that the flow properties are significantly affected when nanoparticles are suspended in the base liquid (67, 68, 70, 118). Nanofluid research is focused on understanding its thermal properties and little attention has been placed to the flow properties of the system. Furthermore, we must understand how the flow properties will be affected by the interaction between nanoparticles and proteins.

A dynamic viscosity analysis is used to understand how nanoparticle size, nanoparticle surface charge, nanoparticle concentration, protein or amino acid type and

charge are going to affect the flow properties. The analysis will be conducted with a cone and plate rheometer, shown in Figure 22.

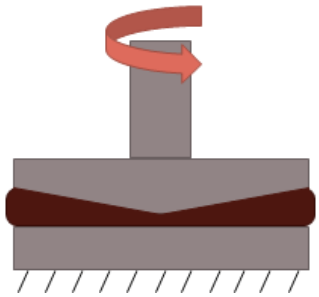

Figure 22 Diagram of cone-and-plate rheometer. The lower plate is fixed while the top cone rotates

Rotational rheometers, like the one used in this research, control the shear rate and measure the shear stress required to keep this shear rate. The viscosity is calculated with the following equation:

$$\tau\ Pa = \frac{\eta\omega r}{r\tan(\alpha)} \quad [6]$$

where $\mu$ is the dynamic viscosity, $\omega$ is the angular velocity, $r$ is the cone radius, and $\alpha$ is the cone angle. For systems where $\alpha$<<1 (in radians), the equation can be simplified to:

$$\tau\ Pa = \frac{\eta\omega}{\alpha} \quad [7]$$

This simplified equation is valid in our system since $\alpha$=0.0175 radians. The angular velocity depends on the shear rate, therefore the cone-and-plate rheometers calculates the viscosity with the following equation, where ω is a function of the shear rate ($\dot{\gamma}$)

$$\eta\ Pa.s = \frac{\tau\alpha}{\omega} \quad [8]$$

Based on Equation 8 above, it is assumed and widely accepted that the shear stress experienced by the tested sample is independent of radial direction. This assumption is valid only for cones with $\alpha$<<1 and a cone radius>>1mm (47, 119). The cone used in this study meets both criteria with $\alpha$=0.0175 radians and cone radius = 20mm. The success of the cone-and-plate system is based on a laminar flow during test. For this geometry, the laminar to turbulent transition occurs at a Reynolds number of approximately 4 (119).

A stepped flow test procedure will be applied. Increased levels of shear rate will be applied to the sample while the shear stress is measured. The controlled and recorded values are used to calculate the dynamic viscosity. The applied shear rate will range from 20 to 500 $s^{-1}$ with increments of 20 $s^{-1}$. Every shear rate increment is maintained for 10 seconds to allow stabilization and the reported viscosity is the one calculated for the last 5 seconds.

This methodology will be applied to measure the flow properties (dynamic viscosity in particular) of the interaction of positively and negatively charged gold nanoparticles with bovine serum and with lysine, arginine, glutamic acid, and aspartic acid at various concentrations.

Table 5 summarizes the material combinations (nanoparticle size, charge, and concentration) used for bovine serum solutions. Figure 23 indicates the naming scheme used for these samples. Table 6 summarizes the material combinations for the amino acid solutions tested. Figure 24 indicates the sample name used.

Table 5 Summary of material combinations for bovine serum solutions

| NP size (nm) | NP charge | Medium | %NP solution volume |
|---|---|---|---|
| 10, 20, 50 | negative | bovine serum | 25%, 50%, 75% |
| 10, 20, 50 | positive | bovine serum | 25%, 50%, 75% |

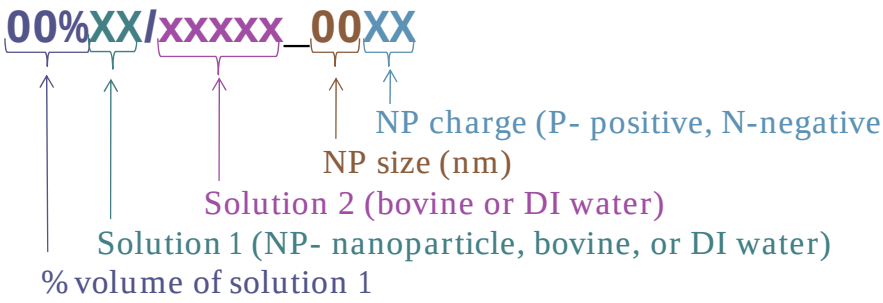


Figure 23 Sample name scheme used for bovine serum solutions

Table 6 Summary of material combinations for amino acid solutions

| NP size (nm) | NP charge | Amino acid | $M_{amino\ acid}$ (mol/L) | %NP solution volume |
|---|---|---|---|---|
| 10, 20, 50 | negative | L-lysine, L-arginine, | 0.01, 0.0001 | 33% & 67% |
| 10, 20, 50 | positive | L-glutamic acid, L-aspartic acid | 0.01, 0.0001 | 33% & 67% |

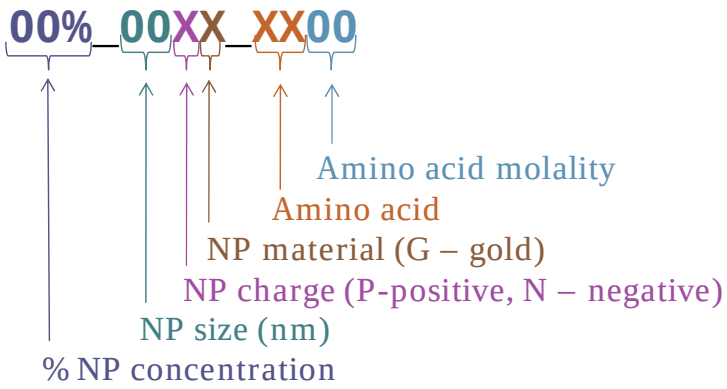


Figure 24 Sample name scheme used for amino acid solutions

### 3.2.2.1. The NP/ amino acid solutions

The physical appearance of the nanoparticle solutions is a good indication of a homogenous nanoparticle suspension. The gold nanoparticle solutions have a deep red to pink color, shown in Figure 25. The characteristic color depends to the NP size present in the solution. Solution color depends on the nanoparticle size present (73, 120, 121). Therefore, a change in color, from red-pink to purple, indicates nanoparticle agglomeration.

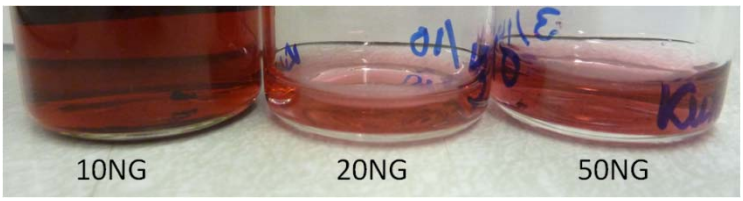


Figure 25 Characteristic red-to-pink color of pure NP solutions

The pure amino acid solutions are clear. The mixed NP/ amino acid solution should show the characteristic red-pink color. However, some samples changed colors when mixed. Figure 26 shows the glutamic acid solutions mixed with positive gold.

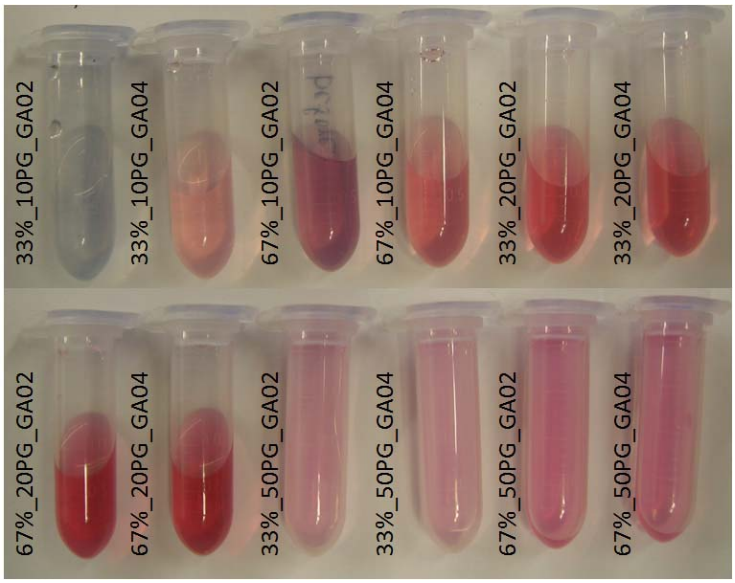

Figure 26 NP solution changes color after mixing with amino acids

### 3.2.3. *In vivo* nanoparticle interaction with the CNS

Nanoparticles have shown promising results in the medical field. Extensive work has been done to understand the uptake of nanoparticles by cultured cells. The main advantage of using nanoparticles in medicine is that their size allows to reach places that traditional medicine does not. The central nervous system (CNS) would greatly benefit from the use of nanomaterials for imaging and drug delivery. The limited access to the spinal cord can be overcome by the use of nanomaterials.

Based on the results obtained from the protein and amino acid interaction with nanoparticles, we understand that negatively charged nanoparticles will interact with positive amino acids and proteins. We introduce a novel method to study the interaction of negatively charged, spherical gold nanoparticles of 46.7 ±5.47nm diameter with the CNS of the discoid or false dead-head roach, *Blaberous discoidalis*. The communication signals of the brain rely on positively charged ions ($Ca^{2+}$, $K^{+}$) (122, 123). We take

advantage of this ionization present in the CNS to promote the interaction with negatively charged nanoparticles.

This research will address the interaction mechanisms of charged nanoparticles with the CNS and present a new, simple biological system for study. The typical biological system used for CNS research is mice but these systems are expensive and strict protocols are in place. We will discuss the viability of using the cockroach for CNS research.

Two groups were selected for this study. Each group had 9 roaches. The selected groups were separated for 24 hours prior to injecting the nanoparticles. Group 1 was used as the control since no nanoparticles were injected into this group. Negatively charged spherical gold nanoparticles were injected into the roaches in Group 2. This methodology will consist of injecting the nanoparticles suspended in DI water into the CNS of the cockroach through the sub-esophageal ganglion. The nanoparticles have a concentration of $1x10^{11}$ NPs/mL, a total of 7μL were injected into the CNS of each insect.

Male *Blaberus discoidalis* (weight = 2.1 ±0.3 g) grown in-house were used in this study. These roaches were maintained in hard plastic containers (9x18”) under controlled environment. The room’s temperature was maintained at 28 ±2 $^{\circ}$C and had a 12/12h day/night cycle. They were fed with dry dog chow. Food and water were supplied *ad libitum*.

The cockroaches were kept in isolation to minimize stressors like noise, wind, and vibration that could alter their behavior. A two-minute video was taken daily at 8:00am, only 10 minutes into the light cycle, to record their activity. Although the insect is most

active during the dark cycle, light was needed to record their activity. The first hour was selected for recording since slightly over one third or 38.1% of the cockroaches show activity during the first hour of the light cycle (124, 125).

Figure 27 shows the basic CNS structure of the cockroach and the site of nanoparticle insertion. The NPs are injected at the sub-esophageal ganglion (SEG) in the direction indicated by the red arrow. The roaches were placed in the plastic container immediately after treatment and were closely monitored for the first 4 hours to ensure activity had been resumed. The insects were monitored daily to verify activity. The roaches that did not show signs of activity were considered dead and were removed and placed in a -80$^{o}$C freezer to prevent tissue damage and allow further analysis.

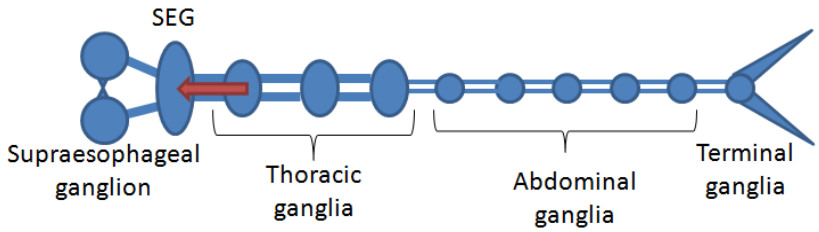


Figure 27 Diagram of the cockroach's central nervous system. The arrow shows the site and orientation of nanoparticle injection

### 3.2.3.1. Monitoring insect behavior

The effect of the NPs on the CNS will be evaluated by monitoring changes in the insect's activity. The cockroach locomotion is controlled by the CNS (77) and if the communication channels are altered by the charged nanoparticles, the insect's activity will be affected. The activity of a control (untreated) and the treated groups were monitored daily for 2 months at which time the insects' brains were be extracted and dissected to

observe if the NPs remain in the CNS, if have traveled through the CNS of the cockroach and to observe the nanoparticle interaction mechanisms.

## 3.3. Characterization

The material and physical properties of all used samples were characterized. The tools used for characterization depended on the material scale and properties.

### 3.3.1. Material properties

#### 3.3.1.1. Surface roughness

The surface roughness of the bulk materials (PC, PMMA, and glass) and the thickness of the Ti and Cr nitride coatings were measured with contact & non-contact profilometers. For the PC, PMMA, and glass a TR200 Profilometer from Qualitest was used, Figure 28. The stylus scanned across the surface in a 5mm single straight line in order to trace the surface profile and to measure the average surface roughness (Ra). As a standard procedure, five readings were taken at various locations and the average values of Ra were recorded. A Dektak 150 Profilometer with 3mg load was used to measure Ti and Cr nitride coating thickness, Figure 29.


Figure 28 TR200 Qualitest contact profilometer

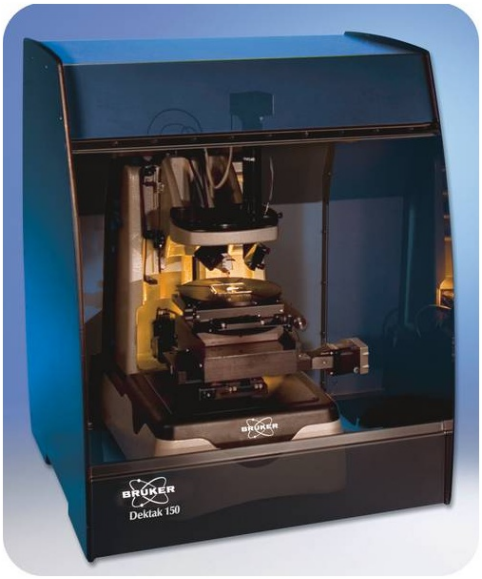


Figure 29 Dektak 150 contact profilometer (126)

A Zygo NewView 600s 3D optical surface profilometer is shown in Figure 30. The Ti and Cr nitride coating thickness were measured with this instrument. A 10X magnifying lens was used for analysis. Figure 31 shows a diagram of how the optical profilometer works. The light source is split and the reflected light beams from the tested surface and an ultra smooth reference mirror are detected by the camera. Any deviation between the reflected light from the sample and the reference mirror is due to height differences.


Figure 30 Zygo NewView 600s non-contact profilometer (127)

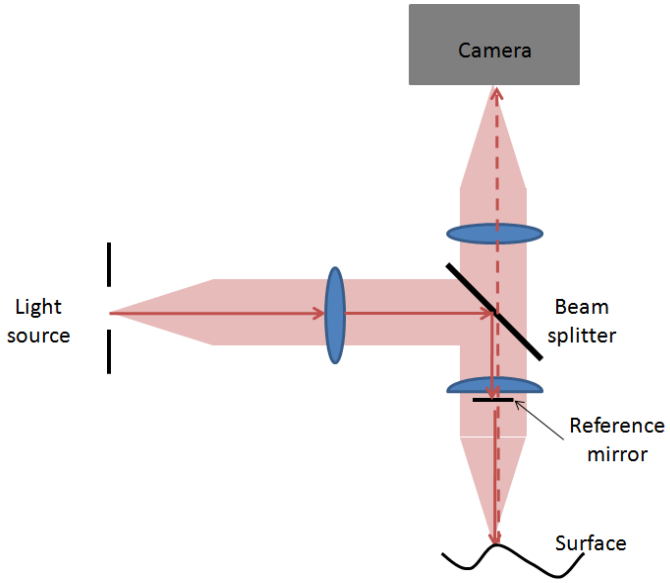


Figure 31 Diagram of optical profilometer. The height map is obtained by comparing the intensity of the reflected light beams from the surface and the reference mirror

### 3.3.1.2. Contact angle

The Sessile drop method was used to measure the contact angle. The images were recorded with a Panasonic Lumix SMC-ZS1 digital camera and analyzed with the LB-ADSA drop analysis feature from ImageJ.

### 3.3.1.3. Energy Dispersive X-Ray Spectroscopy (EDS)

A SUPRA 55 Scanning Electron Microscope (SEM), shown in Figure 32, was used on the Ti and Cr nitride coatings to analyze the coating composition with the Energy Dispersive X-Ray Spectroscopy (EDS). The EDS was used with an acceleration voltage of 15.0 kV and a take-off angle of 33.1$^{o}$.

Figure 32 Supra 55 scanning electron microscope (SEM) equipped with energy dispersive X-ray spectroscopy (EDS) (128)

### 3.3.1.4. X-ray diffraction (XRD)

XRD helps identify the crystallographic composition and orientation of the material's surface. The XRD was used to characterize the Ti and Cr nitride coatings. A

scanning rate of 0.020 $s^{-1}$ in the $2\theta$ range 5-90° was used for XRD. The system uses a Rigeku $D_{max}$ $\gamma_A$ X-ray diffractometer with Cu Kα radiation ($\lambda$ = 0.154178).

### 3.3.2. Physical properties

#### 3.3.2.1. Digital microscope

The cultured chick retina cells were imaged before and after testing with a VHX-600 3D digital image microscope from Keyence, shown in Figure 33, to observe changes in cell size and shape before and after testing. The microscope was used with magnifications from 100X to 1000X, depending on the desired feature sizes.

Figure 33 VHX 600 digital microscope from Keyence

#### 3.3.2.2. Confocal microscope

An Olympus FV1000 Confocal Microscope, shown in Figure 34, equipped with a 510 nm argon laser was used to detect where the negatively charged gold nanoparticles were located within the cockroach brain. The insect brains were extracted, fixed with FrozFix (Newcomer Supply), mounted in OCT at -17°C and cryocut to 12 μm thickness and mounted with DPBS (Dulbecco's Phosphate Buffered Saline) on glass slides. The

gold nanoparticles used in this study fluoresced at 560 nm with an excitation wavelength of 510 nm.

Figure 34 FV1000 confocal microscope (courtesy of Olympus)

### 3.3.2.3. Scanning electron microscope (SEM)

The adhered cells on the surface of PMMA and PC were imaged with a JEOL JSM-6400 Scanning Electron Microscope. The SEM images for PMMA were taken at 1,000X magnification, with 15 kV accelerating voltage, and a working distance of 11 mm. The SEM images for PC were at 1,000X magnification, 15 kV accelerating voltage, and 8 mm working distance. The pre-focus was done outside the test area to reduce the electron beam damage. Minor focus adjustments were done on the test area. Figure 35 shows the SEM used in this study.

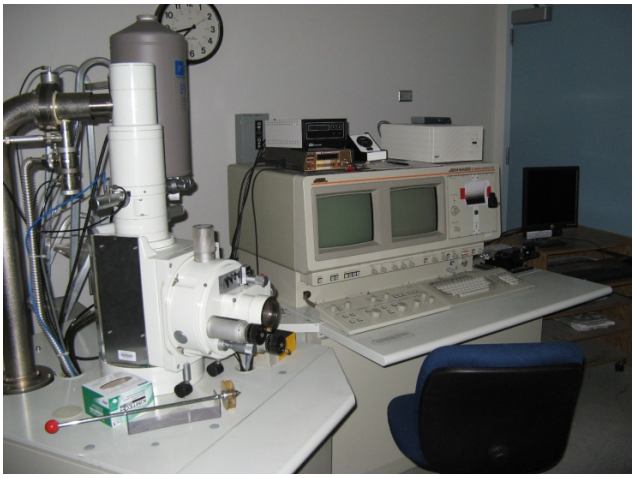

Figure 35 JEOL JSM-6400 Scanning Electron Microscope

### 3.3.2.4. Transmission electron microscope (TEM)

A JEOL-JEM 2010 TEM (Figure 36) was used to characterize the morphology of NPs in the CNS of the cockroach. The insect brains were extracted, fixed with FrozFix (Newcomer Supply), mounted in OCT at -17$^{o}$C and cryocut to 12 µm thickness and placed on copper grids for TEM imaging. The images were taken within 24 hours of samples preparation.

Figure 36 JEOL-JEM 2010 TEM used to characterize the morphology of the NP/ CNS of the cockroach

The NP/amino acid solutions were characterized with the JEOL 1200EX TEM (Figure 37). One drop of the tested NP/amino acid solution was set on the copper grid. The excess DI water was evaporated by heating the copper grid. The samples were tested within 24 hours of preparation.

Figure 37 JEOL 1200EX TEM used for NP/amino acid morphology characterization

#### 3.3.2.5. Atomic force microscope (AFM)

A Pacific Nanotechnology AFM with a Si tip was used in tapping mode (1Hz frequency) to identify the surface properties of the Ti and Cr nitride coatings deposited on (111) Si wafer and Ti alloys. Figure 38 shows the AFM used in this study.

Figure 38 Atomic force microscope (courtesy of Pacific Nanotechnology)

### 3.3.2.6. X-ray photoelectron spectroscopy (XPS)

Two XPS systems were used: one for the characterization of the amino acid/nanoparticle bonding and one for the characterization of the nanoparticle interaction with the CNS of the cockroach.

The line 8 of the Stanford Synchrotron Radiation Lightsoure was used to characterize the amino acid/gold nanoparticle interactions. The samples were scanned with a monochromatic energy of 780eV (incident energy). The CMA was charged with a pass energy of 50eV to filter out stray electrons from entering the analyzer. The scans were performed between 0.5 and 1 s/step, with a step size between 0.1-1 eV depending on the feature of interest. The sample was at a maximum pressure of $5x10^{8}$ torr during scans.

The results provide insights into amino acid and/or surfactant polymerization. Several layers of the solution were deposited on the surface of a Si wafer. The sample was allowed to air dry. Based on the amount of amino acid and nanoparticles present in the solution, it is estimated that the coating thickness was in the order of tens of nanometers.

A Kratos Axis Ultra Imaging X-ray photoelectron spectrometer (XPS) with a spherical mirror analyzer was used to identify gold in the CNS of the cockroach. The XPS was operated with a Mg-Kα (1253.6 eV) X-ray radiation at a power of 350 W and a base pressure of $10^{-10}$ Torr. The treated insect brain was extracted, fixed with FrozFix (Newcomer Supply). The extracted brains were mounted in OCT at -17$^{o}$C and cryocut to 12 μm thickness and mounted on quartz slides.

### 3.3.2.7. Hyperspectral imaging

The presence of gold nanoparticles in the CNS of the cockroach was first identified with the hyperspectral imaging system from CitoViva. This imaging system identified the presence of gold in the tissues by comparison. A sample of NGs/DI water solution was scanned to identify the emitted fluorescence of the nanoparticles. The hyperspectral imaging, as shown in Figure 39a, provided a range of emitted signal due to the variations in size during nanoparticle fabrication and possible agglomeration once in contact with the CNS. A signal library was generated from this scan, Figure 39. The NGs treated tissue was then scanned and the spectral imaging was compared to that of the library. The NG treated brain was extracted, fixed in Zamboni's fixative for 30 min and rinsed in DI water 3 times for 10 minutes each. The samples were placed on a glass slide.

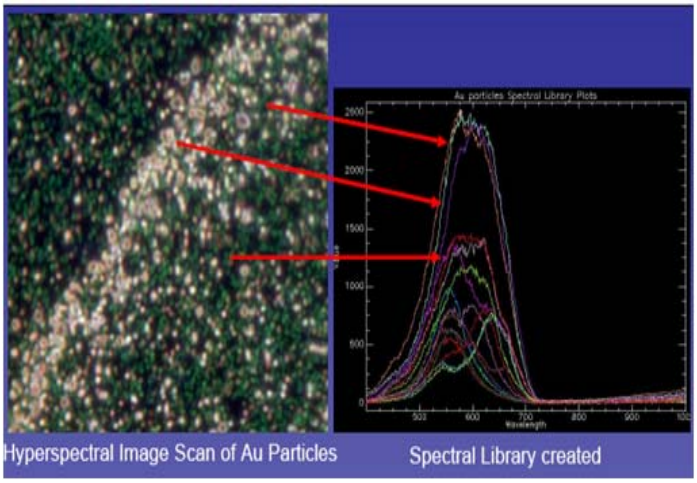


Figure 39 (Right) spectral library created by scanning the gold nanoparticle solution (left)

# CHAPTER IV

# BIOMOLECULAR INTERACTIONS WITH SYNTHETIC BULK MATERIALS*

This chapter discusses the material characterization and cell or protein adhesion studies. Great emphasis is placed on the effect of material chemistry on the cell adhesion and the strengthening mechanisms of the cells. Swiss mouse fibroblasts (3T3), chick embryo neurons, and egg-white protein are used in these experiments to study adhesion mechanisms of biomolecules with bulk materials. The adhesion of 3T3 fibroblasts to polymeric surfaces, the strengthening of chick embryo neurons on poly-D-lysine coated glass, and the adhesion of egg-white protein to titanium and chromium nitride coatings on Si and Ti alloy substrates are studied.

## 4.1. The importance of cell/protein adhesion

Cellular interaction with a foreign surface (i.e., a biomaterial) is of utmost importance for the long-term performance of the biomaterial. The strength of cell/surface interaction greatly depends on its application. There are cases where a strong interaction (good cell adhesion to the surface) is necessary. Such is the case of cochlear implants, artificial joints, and heart valves, to name a few. For these applications, it is imperative

---

* Part of the information reported in this chapter is reprinted with permission from "Critical fluid shear stress analysis for cell–polymer adhesion" A. Rocha, M. Hahn, H. Liang, 2010. *Journal of Materials Science,* 45 (3), 811-817, Copyright 2010 by Springer/Kluwer Academic Publishers and from "Neuron adhesion and strengthening" A. Rocha, K. Jian, G. Ko, H. Liang, 2010. *Journal of Applied Physics*, 108 (2), 024702-024706, Copyright 2010 by American Institute of Physics.

that the tissues surrounding these devices identify the biomaterial as part of the body. If cell function is altered, the risk of tissue death and ultimately rejection are inevitable.

The adhesive strength of NIH/3T3 fibroblasts, a commonly used cell type in adhesion studies on poly (methy methacrylate) (PMMA) and polycarbonate (PC) substrates is measured. These materials were selected because they are widely used in biomedical applications. The adhesion and strengthening mechanisms of 12-day old chick embryo neuron adhesion to poly-D-lysine coated glass is investigated. This work also studies the adhesion of egg-white protein on titanium and chromium nitride coatings.

## 4.2. NIH/3T3 Swiss mouse fibroblast adhesion to polymeric materials

### 4.2.1. Material characterization

The surface roughness and contact angle of the PMMA and PC was measured as received and after exposure to shortwave UV radiation, used to clean the surface. Their surface roughness was measured with a TR200 surface profilometer from Qualitest. The contact angle was measured with the Sessile drop method. Table 7 summarizes the results. The surface roughness (Ra) of PMMA had a 6.7% increase from 0.0672 to 0.0716 μm while PC had a 70% decrease from 0.0602 to 0.0182 μm. The surface of PC became smoother after exposure to UV radiation for sterilization. The contact angle increased by $1.1^{o}$ for PC and decreased by $3.2^{o}$ for PMMA.

Table 7 Surface roughness and contact angle of the substrate materials before and after exposure to shortwave UV radiation for sterilization

| | | Ra (nm) | Angle (deg) |
|---|---|---|---|
| PC | Before | 67.2 ± 25.4 | 71.3 ± 1.4 |
| | After | 71.6 ± 9.3 | 70.3 ± 3.2 |
| PMMA | Before | 60.2 ± 11.8 | 64.9 ± 2.5 |
| | After | 18.2 ± 7.5 | 68.1 ± 1.6 |

### 4.2.2. Cell adhesion

Figure 40 shows a representative set of images demonstrating the removal of cells beyond the radius of the critical shear stress for cells adhered to the PMMA exposed to a maximum rotational shear stress of 2.5 Pa. The circular region outlined in Figure 40g corresponds to the critical radius, with associated optical micrographs positioned along its perimeter. Note that, beyond the critical radius, cells have been stripped from the surface while cells remain adherent within this radius. The PC was tested to a maximum of 1.0 Pa and it showed similar behavior. The observed critical radius must be translated into a corresponding critical shear stress using Equation 5, presented in Chapter III.

$$\tau_{R_c} = \frac{R_c}{R_{max}} \tau_{max}$$

The measured $R_C$ for PMMA and PC were 1.05±0.015 cm and 0.636±0.008 cm respectively. The calculated $R_C$ was 2.1Pa for PMMA and 0.509Pa for PC. The cell adhesion results are indicated in Table 8.

Table 8 Critical radius and calculated critical shear strength of fibroblast on PMMA and PC

| Material | Rc (cm) | $\tau_C$ (Pa) |
|---|---|---|
| PMMA | 1.05±0.015 | 2.1 |
| PC | 0.636±0.008 | 0.51 |

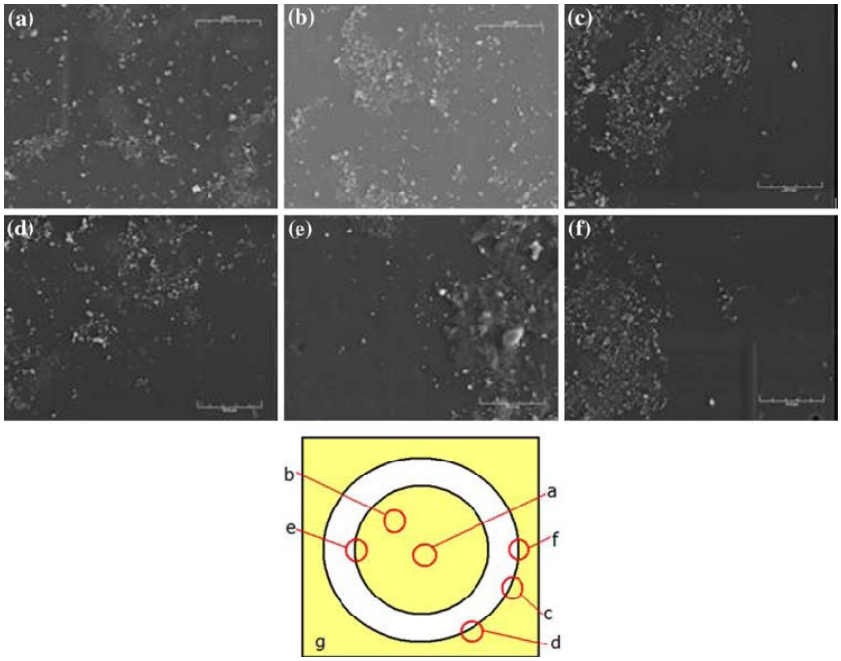


Figure 40 a-g SEM images of cell cultured PMMA after adhesion testing. The line scale is 30 μm

The cells have a stronger adhesion to PMMA than to PC. There are two possible reasons for this behavior. One is the molecular interactions at the cell-substrate interface and the other is the surface roughness of the substrate. The molecular interactions are mainly due to the chemical composition of proteins and the substrate material. Cell attachment is mediated by the extracellular matrix (ECM), which is made of polysaccharides (sugars), and collagen (proteins) that provide structural support and protection to cells (129). The proteins in the ECM are also responsible for carrying all

necessary electrochemical processes and control tissue elasticity, humidity, and adhesion (100, 101). Those are key elements in the cell/biomaterial interface (6). The proteins that participate in cell-cell adhesion and cell-substrate adhesion vary with cell type. In the case of fibroblasts, cytokines are the main proteins that mediate cell-cell adhesion while fibronectin is the main protein that controls cell-substrate adhesion in the (83, 129, 130). The cell attaches to the fibronectin through the selectins. The end of the fibronectin that reacts with the selection on the fibroblast has a carboxylic end (-COOH). The other end has an amide group ($-NH3^{+}$) which attaches to the substrate (131-135). This amide group is electropositive thus results in high adhesion strength if the surface is electronegative as in the case of PMMA. In terms of the surface roughness, our results showed that both samples had ultra smooth surface in comparison with the size of a cell (~30 μm). The PC became even smoother after the sample preparation. The wetting angle results showed that there was minimum change in the value ($\sim 3^{o}$) indicating the negligible effects of the surface roughness. The smooth surface enabled us to effectively evaluate the method to test cell/fluid shear. Further studies on roughness (at high value range) effects will be carried out in near future.

We developed a methodology, using a simple rheometry technique, to quantitatively measure the adhesive strength of cells attached to synthetic polymer surfaces. To demonstrate the technique, two polymer based materials currently used in various biomedical applications were examined, namely PMMA and PC. The cell-seeded polymers were exposed to the rotational shear stress under a constant operating maximum shear stress constraint. Since a shear stress varies with its radial position, a threshold shear

stress beyond which cells were detached from the material surface could be identified. Subsequent analysis of experimental results indicated that the cell adhesive strength on the tested materials varied based on material chemistry. One possibility for the PMMA to have a stronger adhesion than PC was due to its highly polarized C-H-O group.

### 4.3. Neuron adhesion to poly-D-lysine coated glass and strengthening

Cells, as live organisms, will respond and react when an external force is applied. This study is focused on measuring neuron adhesion and to understand the neuron strengthening mechanism.

#### 4.3.1. Quantifying cell adhesion

The same testing method was used for neuron adhesion studies (rotational flow via parallel plate). To identify the strengthening mechanisms of the cells, the samples were tested with increasing shear stress from 1 to 7 Pa with a 1.5 Pa increments.

After testing, a series of images were taken along the critical radius (Rc). The images were aligned, as in Figure 41, to form a "panoramic view" along the Rc. Figure 41 clearly shows there was a clear continuous circle that indicates the location of neurons after testing. In the area outside the circle, the neurons were completely detached.

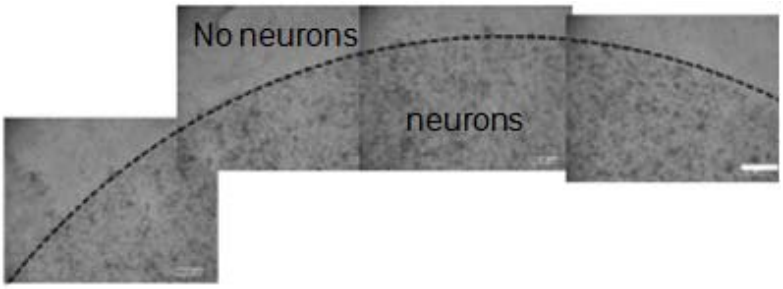


Figure 41 Critical radius representing the critical point of cell detachment in 12-day-old chick embryo neurons

### 4.3.2. Neuron strengthening

The recorded values for angular velocity ω (rad/s) and dynamic viscosity η (Pa.s) for all tests are summarized in Figure 42. The values reported here are for the last minute of test, well beyond the point of equilibrium flow. As expected, the angular velocity values increase with increasing shear stress. The dynamic viscosity values only show a slight variation.

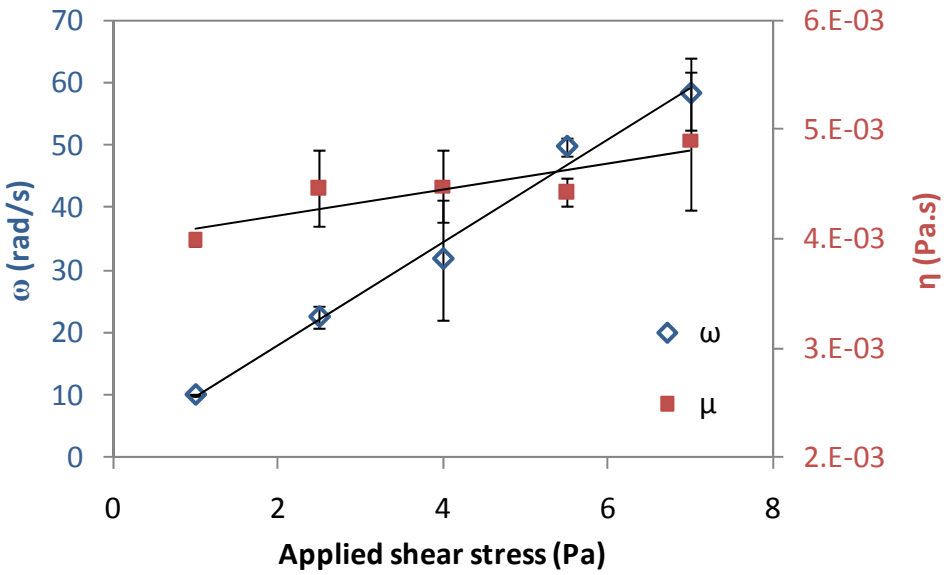


Figure 42 Average angular velocity (ω) and dynamic viscosity (μ) with respect to applied shear stress ($\tau_{max}$)

The results of neuron adhesion, tested from 1 to 7 Pa is summarized in Figure 43. These experiments were conducted in order to understand how the fluid shear affects the neuron/poly-D-lysine interface. The neurons respond to the fluid shear actively. In other words, the neuron adhesion to poly-D-lysine is stronger with higher applied shear. The critical radius $R_C$ was measured against the applied fluid shear stress and results are

summarized in Figure 43. The measured $R_C$ decreases almost linearly with the increasing fluid shear. It means that more cells were detached with increasing fluid shear value.

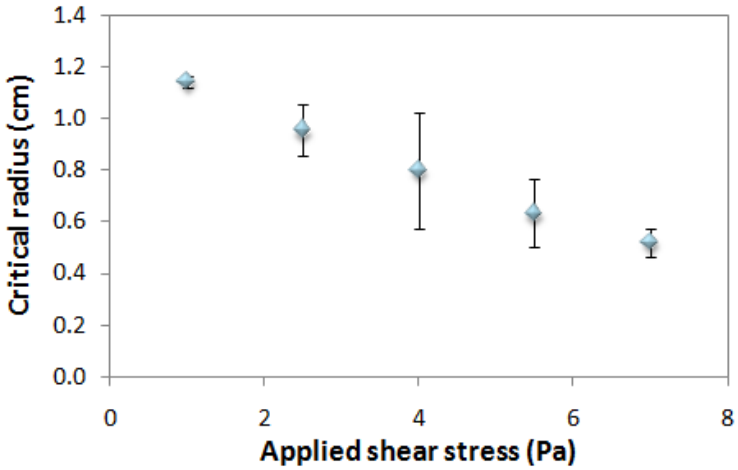


Figure 43 Critical radius decreases with increasing applied shear stress for chick embryo neurons

Estimating the adhesive strength is achieved by calculating the critical shear stress ($\tau_C$) which has been discussed in detail in Chaper III. The calculated $\tau_C$ results are plotted in Figure 44. It is seen that the $\tau_C$ varied from 1.0 to 3.0 Pa. Even though the $R_C$ decreased with increasing $\tau_a$ (Figure 3), the $\tau_C$ reached a constant value of approximately 3 Pa for the $\tau_{applied}$ of 4 Pa and higher. The repeatability and consistency of the results obtained here in comparison with other methods for neuron adhesion studies (104, 136) have demonstrated that the system used here is of high accuracy.

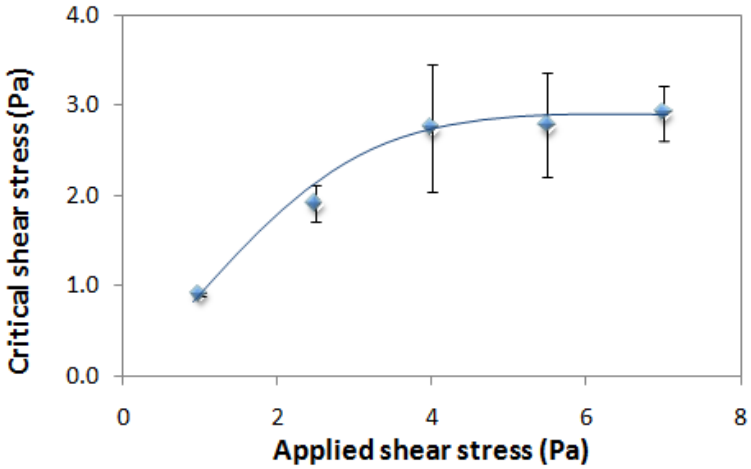


Figure 44 Chick embryo neuron strengthening. The adhesion strength ($\tau_c$) reaches a maximum of 3Pa

Interestingly, the results in Figure 44 indicated that the $\tau_C$, i.e., the adhesive stress at the neuron/substrate interface increased with the applied shear stress. The adhesive shear stress plateaus after a specific applied stress value. This means that the neuron cell adhesion was strengthened at the beginning and then stabilized. The strengthening, or strain hardening, effects have been observed in other cells (83, 137-139) but it has not been quantified prior to this work, particularly for neurons. The increase in $\tau_C$ indicates the strain hardening and the neuron's adhesive strength then reached a constant value at approximately 3 Pa. It is believed that strain hardening of a cell is accompanied by a permanent deformation. We conducted high resolution characterization of the neurons before (Figure 45a) and after testing (Figures 45b and c). It is seen that neurons maintained their shape and confluency. Figures 45b and c demonstrate that no neuron deformation occurs after testing. This proves that the generated flow does not damage the cells inside the $R_C$.

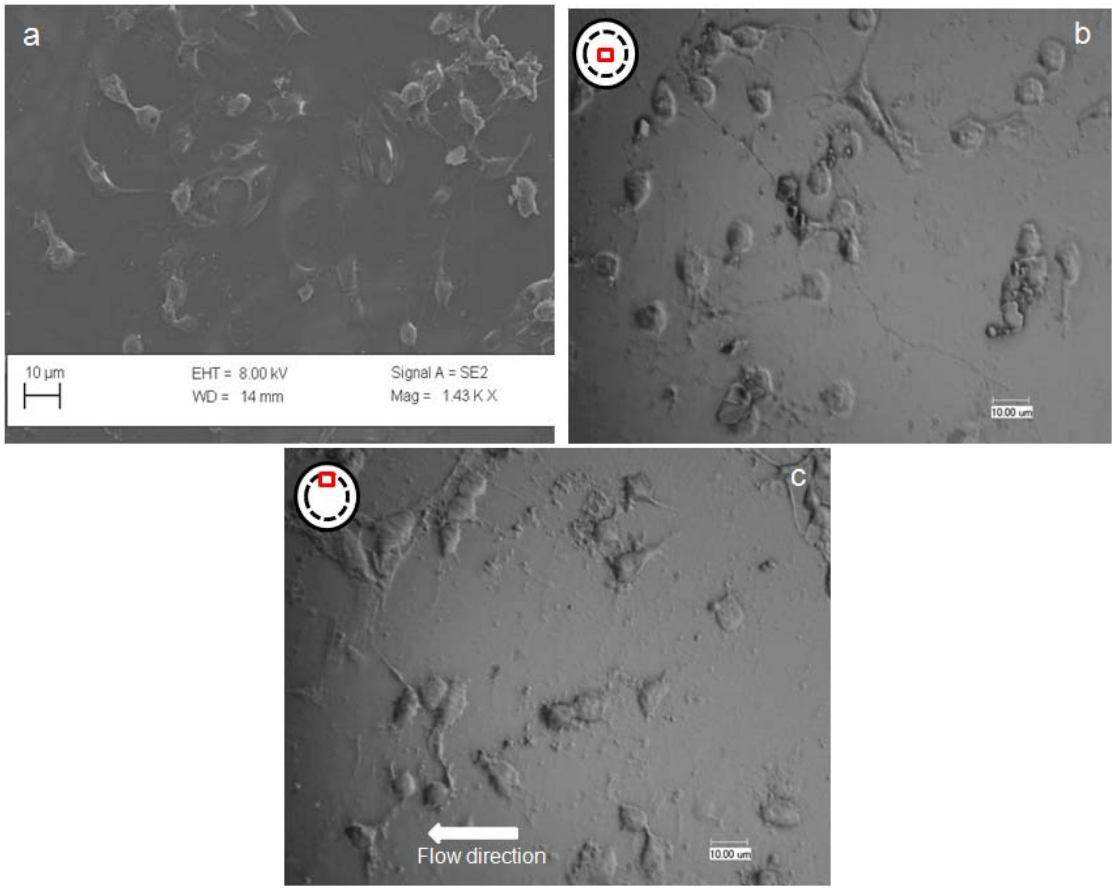


Figure 45 Microscopic images of 12-day old chick embryo retina neurons on poly-D-lysine coated glass (a) before testing and at various locations after testing: (b) center, and (c) along the critical radius

What is the likely reason for the strain hardening? It has been reported that different external stimulus, such as mechanical stretching, could increase the cell adhesion. There are two possible reasons. One is an increase in the number of adhesion molecules (i.e. focal adhesions) (139, 140) and the other the polymerization of the actin filaments in the direction of the deformation (138, 139, 141-143). The latter is generally accompanied by permanent cell deformation which leads to an increase in cell spread projecting a larger surface area on the image obtained. The apparent surface (2D projection on the substrate) was measured with the area feature from the Image Tool.

Image tool is free software developed to acquire, edit, and analyze images. Some of its features include distance, angle, perimeter, and area measurements. This software was selected to measure the surface area (2D projection of the neuron onto the substrate) of the neurons before and after testing.

The neuron 2D projection before and after testing was measured. The neuron projection was 61.4 ±21.1 $\mu m^2$ before testing. Two test regions were selected for after testing, at the center (minimum shear stress) with 58.8 ±11.9 $\mu m^2$ and along the critical radius (highest shear stress and close to adhesion stress) with 66.17 ± 13.9 $\mu m^2$ at. The results are summarized in Figure 46.

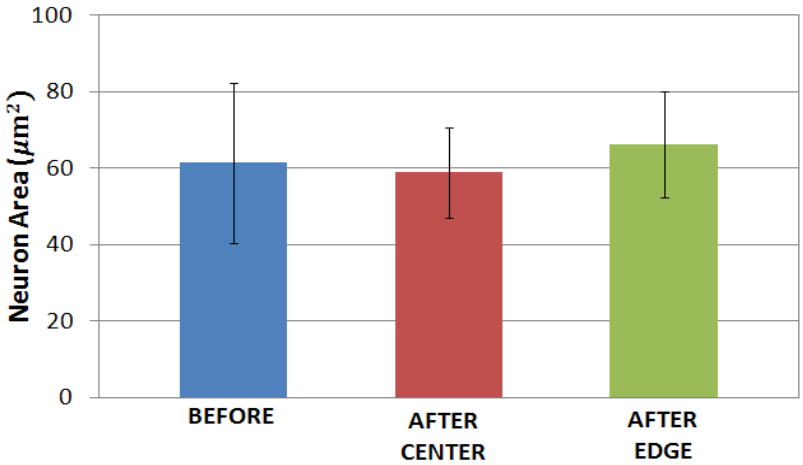


Figure 46 Neuron 2D projection on the substrate measured before and after fluid shear testing at the center (no shear) and along the critical radius (edge – maximum shear)

Based on our measurements of the area projection onto the surface, the neurons show no sign of deformation. This can be physically observed in Figures 45a-c. The shape and state of the neurons along the critical radius (45c) are close to the untested (45a) and the cells at the center of the tested samples (45b). The negligible difference in neuron size

before and after testing indicates that actin polymerization is not likely the reason of strengthening.

#### 4.3.2.1. Neural adhesive force

The methodology used here enables to measure the shear stress of neuron detachment with high repeatability and accuracy. This critical shear stress can then be used to calculate the adhesion force. It is widely known that the shear stress ($\tau$), force ($F$), and area ($A$) are related as follows:

$$\tau = \frac{F}{A} \quad [9]$$

The adhesion force, or critical adhesion force $F_C$, can be calculated using the critical shear stress ($\tau_C$) and the measured 2D projection of the neuron on the substrate. The critical force ranges from 56.8 ±0.3 pN for an applied shear stress ($\tau_{applied}$) of 1Pa and 181.5 ±4.8 pN for an applied shear stress of 7 Pa. The calculated value of $F_C$ is summarized in Figure 47. There is no data available on adhesion force of chick embryo neurons. The only close data was found in the AFM measurement of various cells.(144, 145) It is clear that data obtained in this research are in the same magnitude of previous reports. This indicates that the fluid method is consistent with other methods such as AFM. The method used in this study is simpler and faster than the ones currently used. Using a shear flow method to study the neuron cell adhesion is an approach that is simple and fast. It has been proven to be effective and accurate in adhesion evaluation without destruction of neuron cells. Being so, the strengthening phenomenon was observed.

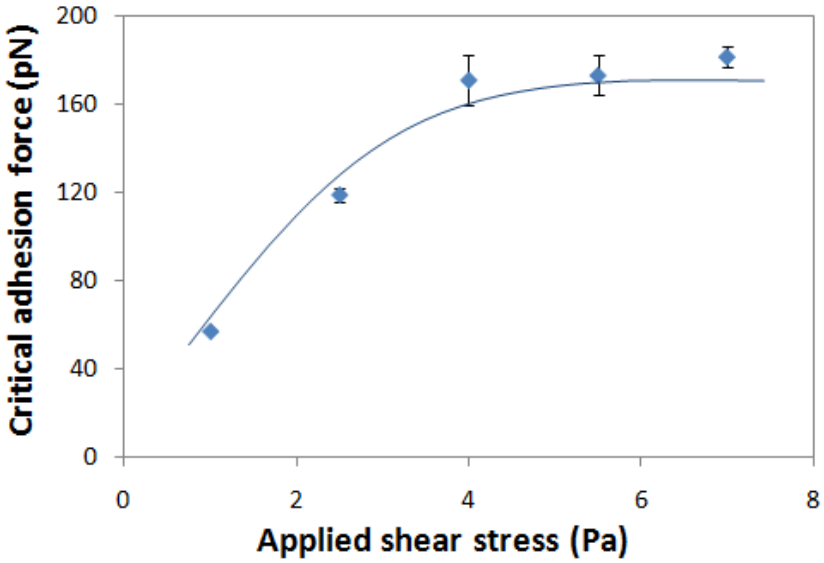


Figure 47 Critical adhesion force (detachment force)

### 4.4. Egg-white protein adhesion to titanium and chromium nitride coatings

Artificial joints have undergone significant improvements in their design. Their success, however, also heavily relies on the materials selected. Polymer-on-metal (POM), ceramic-on-metal (COM), and metal-on-metal (MOM) have been among the top choices where POM has been more widely used. Recent work by Fisher and colleagues show that MOM offer improved wear resistance (146). Their work, as well as the work of Liang et al. clearly demonstrates a decrease in wear when the Ti and Cr surfaces are nitrided (146-148).

Although improved wear properties have been identified, the biocompatibility of the material is still an issue. The work of Serro and colleagues and Williams et al. indicate an improved biocompatibility of the TiN and CrN coatings respectively (149, 150). Furthermore, Serro et al. identify how likely albumin protein is to interact with the surface by following the Langmuir model (149). Their work, however, only indicates how likely

the protein is to be attracted to the surface and makes no attempt at quantifying the strength of this protein/surface interaction.

Protein adhesion is important for biocompatibility since it is the first step in bioincorporation (31-37, 39, 83, 151). The most important objective of this investigation is to quantify the protein adhesion strength to TiN, TiAlN, CrN, and CrAlN coatings and identify the main factor affecting protein adhesion: coating material, surface roughness, or substrate. We address the effect of surface roughness by tailoring it to ~3nm, ~30nm, and ~150nm. Si wafer was used as the substrate for the samples with 3nm surface roughness. Ti alloy was mechanically polished to ~30nm and ~150nm surface roughness. The Si and Ti substrates were also selected to identify if the substrate plays any role in the surface's interaction with the protein.

### 4.4.1. Characterization methods

The coating composition was verified with a SUPRA 55 EDS and its microstructure was analyzed with AFM. Composition by EDS confirms the presence of the coating materials (Ti, Cr, Al, and N). The results also show traces of Si because the EDS was performed on the coatings of the Si substrates.

A Dektak 150 contact profilometer was used to measure the coating thickness. The surface roughness was measured with a Zygo 3D Optical Surface Profilometer. The contact angle was measured with the Sessile drop method. The drop was analyzed with the LB-ADSA drop analysis feature from ImageJ. Egg-white protein solution was used for this experiment.

### 4.4.2. Protein adhesion measurements

The protein adhesion is measured with a rotational shear flow as described in Chapter III. DI water was used to create the shear flow. The tests were conducted at 25°C to prevent test media evaporation. The $R_C$ can be clearly seen after testing. A photograph of the tested sample was taken with a Panasonic Lumix SMC-ZS1 digital camera. The $R_C$ is measured with UTHSCSA ImageTool. An example of a clean radius is evidenced in Figure 48. The outer circle is the spindle size (25mm) and the dashed line is the proteins that remained on the surface ($R_C$).

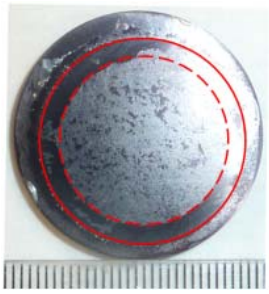

Figure 48 Result from protein adhesion. — is the size of the testing spindle (25mm) and --- is the critical radius ($R_C$)

### 4.4.3. Material characterization

The EDS results are summarized in Table 9. The samples scanned were those coated on Si substrate. The results indicate the coating materials are present. Traces of Si on some samples are caused by the penetration depth of the instrument, i.e., the X-ray penetrated beneath the coating. However, EDS has the limitation of not identifying the presence of oxygen or hydrogen on the surface.

Table 9 EDS results indicates coating composition is contamination free. The presence of Si is from the substrate

| | TiN | | TiAlN | | CrN | | CrAlN | |
|---|---|---|---|---|---|---|---|---|
| | wt% | at% | wt% | at% | wt% | at% | wt% | at% |
| Ti | 55.9 | 28.5 | 28.4 | 12.9 | - | - | - | - |
| Al | - | - | 7.9 | 6.4 | - | - | 6.4 | 7.0 |
| N | 37.8 | 66.0 | 40.5 | 62.8 | 1.5 | 5.3 | 24.5 | 51.5 |
| Cr | - | - | - | - | 98.5 | 94.7 | 64.3 | 36.4 |
| Si | 6.3 | 5.5 | 23.2 | 17.9 | - | - | 4.9 | 5.1 |
| sum | 100 | 100 | 100 | 100 | 100 | 100 | 100 | 100 |

XRD was performed on the metallic coatings to identify if the coating materials formed crystal structures. The results are summarized in Figure 49. TiN, TiAlN, CrN and CrAlN coatings prepared by magnetron sputtering typically form the rock salt crystal structure (152-156). The peaks that have not been labeled correspond to the substrate material.

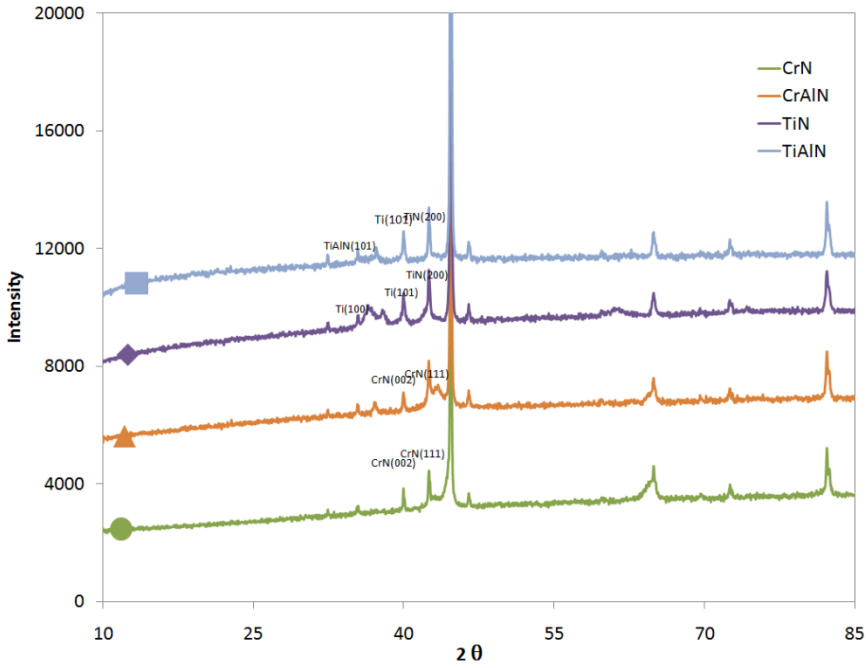


Figure 49 XRD results of the Ti and Cr nitride coatings

The surface morphology was studied with AFM. The height-scan is shown in Figure 50. Grains with 50-100 nm in diameter can be clearly seen. This indicates the coating materials formed crystal structures. The coating thickness was measured with a Dektak 150 contact profilometer with a 3-mg load, shown in Figure 51. The coating thickness ranged from 600 to 800nm. The values presented are an average of five readings. The variation in thickness depends on deposition rate, temperature, and atomic size of the coating materials.

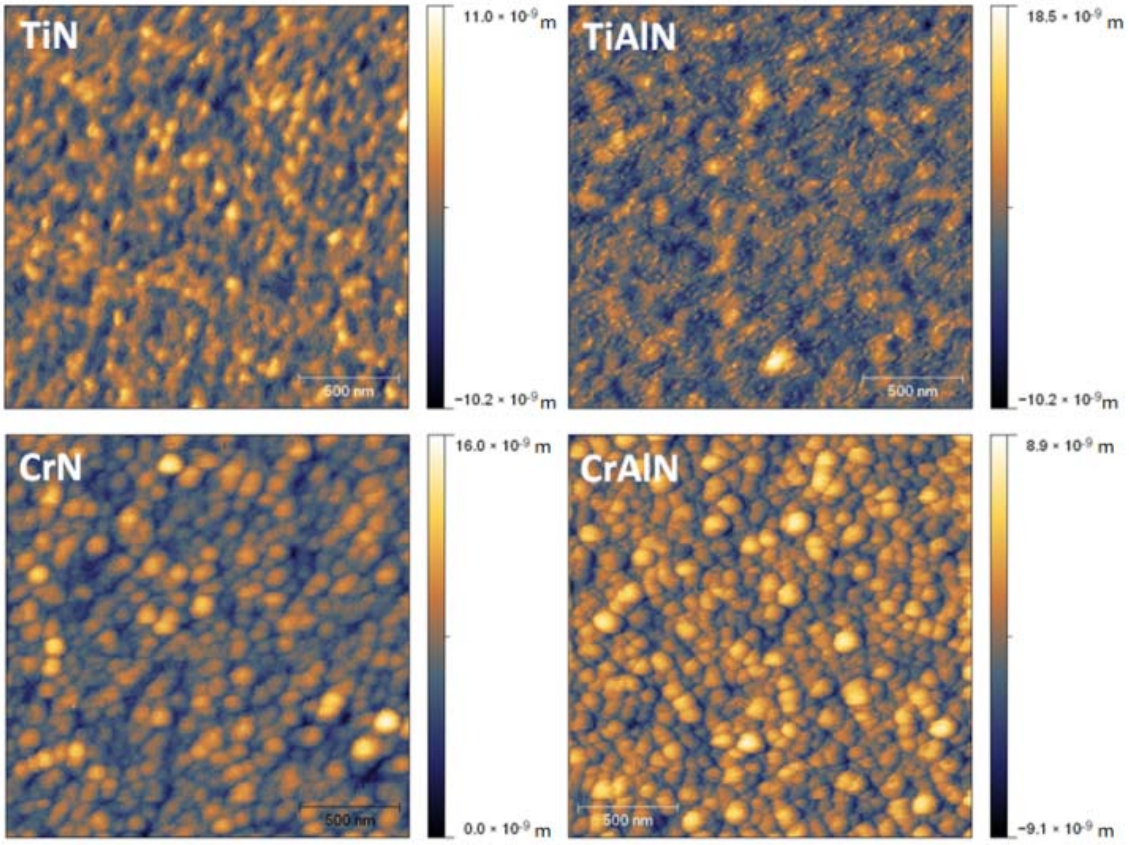


Figure 50 The AFM images (height) indicate a grain size from 50 to 100nm in size. The scale bar is 500nm

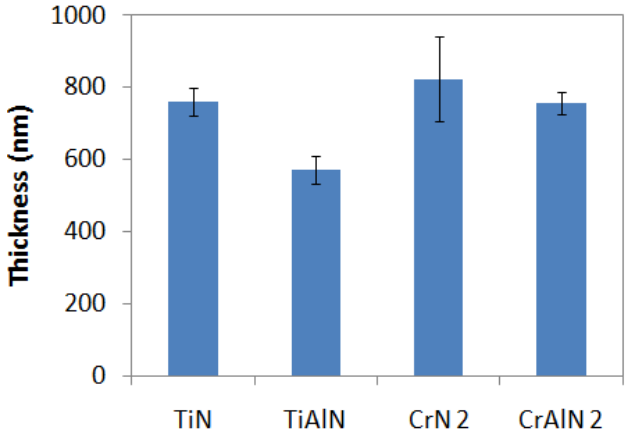


Figure 51 Coating thickness measured with Dektak 150 contact profilometer with a 3mg load

The results of the surface roughness measured with a Zygo 3D Optical Surface Profilometer are summarized in Figure 52. These measurements were performed after the substrates were coated by magnetron sputtering (TiN, TiAlN, CrN and CrAlN). The measurements are averaged over five readings.

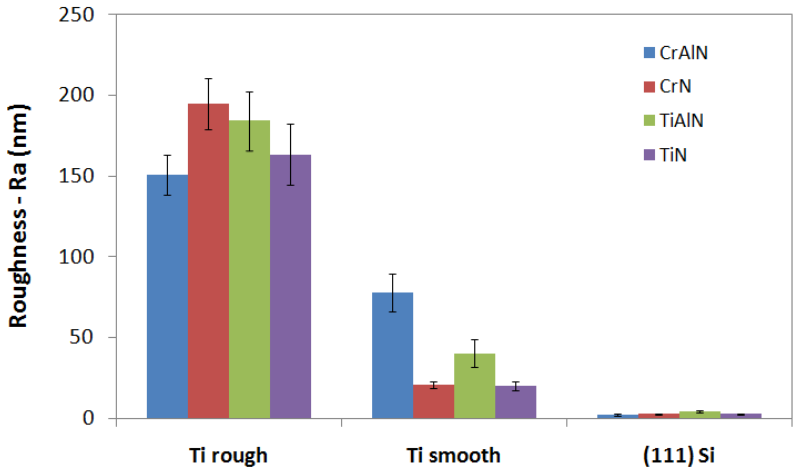


Figure 52 Surface roughness (Ra) measured with a Zygo 3D Optical Profilometer

The substrate's surface roughness was controlled by to order of magnitude difference (i.e. ~3nm, ~30nm, and ~180nm). These values were targeted to observe the effect of surface roughness on its interaction with protein. The coatings on Si wafers have the lowest surface roughness (Ra), 2nm average, and also had negligible variation. Two Ra values were aimed for the Ti alloy substrates, one set at approximately 30nm and another at approximately 150nm. Coatings on the Ti alloy substrates have a wider variation in surface roughness because they were achieved by mechanical polishing. Ti alloy is soft therefore surface roughness by mechanical polishing is difficult to control. Furthermore, the optical profilometer demonstrated that the diamond particles of the

polishing paste used for the 30nm surface roughness caused deep holes on the surface as shown in Figure 53. These pits are the reason for the wide variation on the surface roughness compared to the rough Ti alloy substrates and the Si wafer substrates.

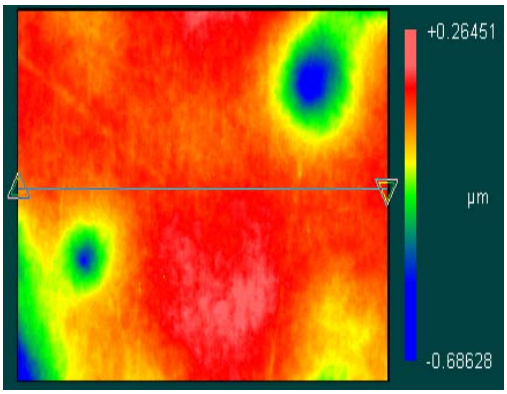


Figure 53 The diamond particles of the polishing paste created pits on the 30nm Ti alloy substrate prior to sputtering. Scan window size is 70mm wide by 53 mm tall

The results of the contact angle measured with the Sessile drop method with egg-white protein-DI water solution are summarized in Figure 54. The drops were analyzed with the LB-ADSA drop analysis feature from ImageJ. On average, the TiAlN coatings have the highest contact angle, followed by CrN, CrAlN, and TiN. It can also be noted that the highest contact angle values are for Ti rough, followed by Si and Ti smooth.

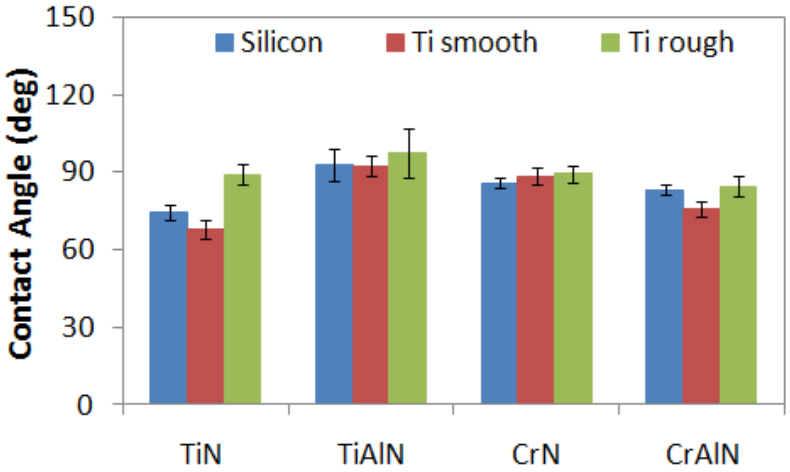


Figure 54 Contact angle measured with the Sessile drop method with egg-white protein in DI water. The contact angle in increasing order is: TiAlN, CrN, CrAlN, and TiN

The results of protein adhesion are summarized in Figures 55a and 55b. The egg-white protein adhesion to the silicon wafer is one order of magnitude higher than that to the Ti alloy as shown in Figure 55a. Figure 55b shows only the protein adhesion to the Ti smooth and Ti rough samples for better comparison. In general, the adhesion of egg-white protein is higher to the smooth than to the rough Ti substrate.

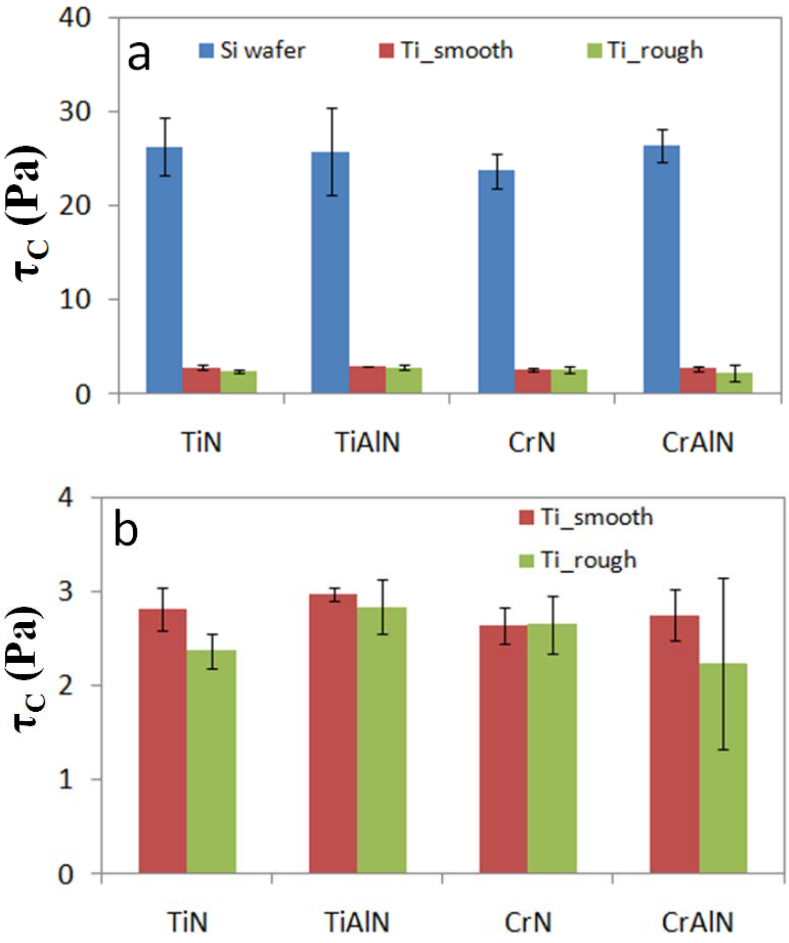


Figure 55 The adhesion strength of egg-white protein to TiN, TiAlN, CrN, and CrAlN coatings on Si, Ti alloy substrates. Figure 55b shows only the results for the Ti substrate to allow better comparison

The TiN, TiAlN, CrN, and CrAlN coatings have been characterized. The EDS shows that only the coating materials are present on the surfaces. Traces of Si are found because the Si substrates were tested. The main concern for the authors is that the system does not identify oxygen, which is expected to be present on the Si and Ti alloy substrates since oxides easily form on these materials when exposed to the environment (157-160). More so in these samples since no attempts were made to remove these oxide layers from the substrate's surface prior to sputtering.

Previous research indicates there is a direct correlation between surface roughness and contact angle (161, 162). This relationship is analyzed in Figure 56. In general, the results show an increasing contact angle with increasing surface roughness, a trend that is expected.

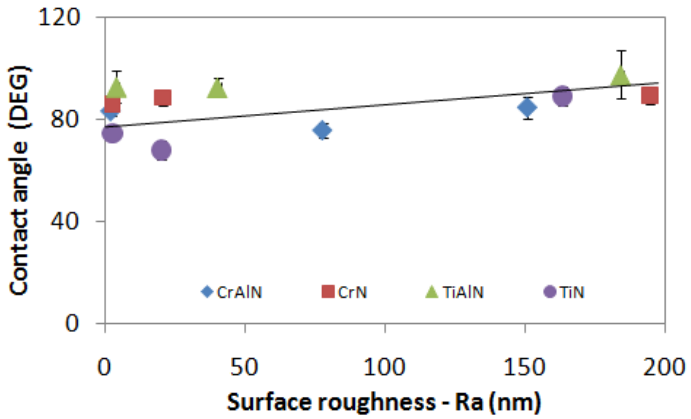


Figure 56 Effect of surface roughness on contact angle

In order to identify the main factor affecting protein interaction, the $\tau_C$ is plotted against contact angle as series of the coating materials in Figure 57a. The results show no dependence of protein adhesion on the coating material. Figure 57b is shown to enhance the adhesion of Ti substrates. Figure 57a clearly demonstrates that substrate material is the most dominant factor. The protein adhesion to the Ti substrates is significantly lower (~2.7 Pa) than the protein adhesion to the Si wafer (~25 Pa).

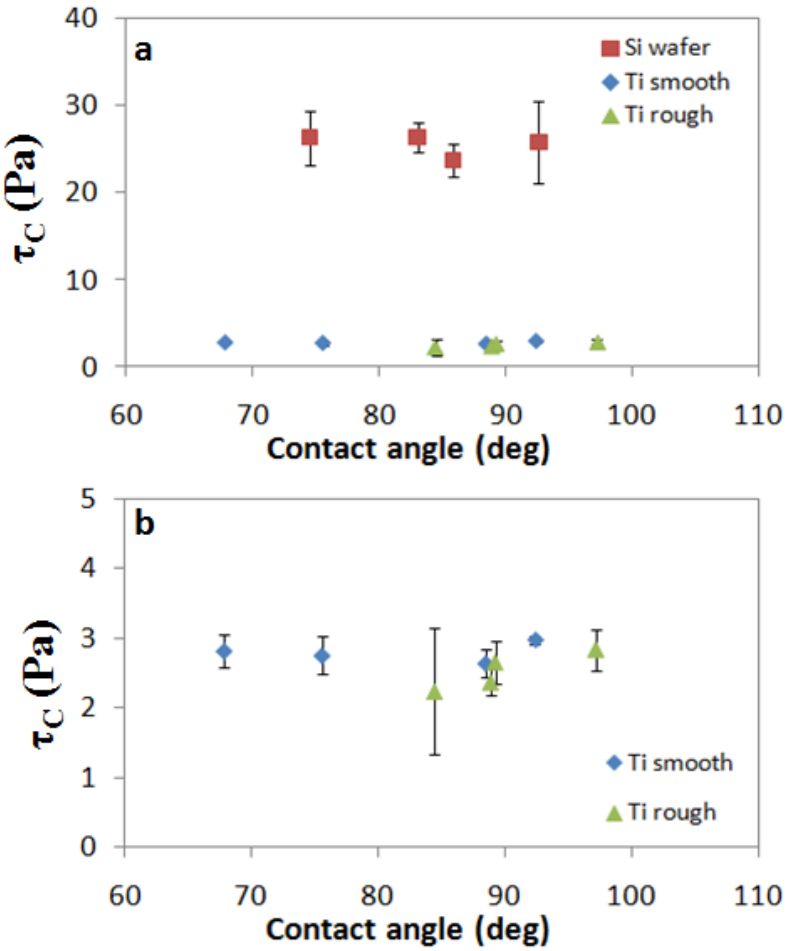


Figure 57 Protein adhesion is clearly dependent on substrate material. The adhesion of egg-white protein, rich in albumen, is one order of magnitude higher (~25 Pa) than the Ti substrates (~2.7 Pa)

What is the reason for this difference? It would be expected that the protein interacts only with the coating material (TiN, TiAlN, CrN, and CrAlN). However, no clear trends can be identified. There is a possibility that the grains formed by the coating material and shown in the AFM images in Figure 50 are not completely sealed; that there are micron-sized gaps between the grains that allow the protein used for adhesion testing to interact with the substrate.

If this assumption is correct, another question arises. Why is the adhesion to Si one order of magnitude higher than the adhesion to Ti alloy? The authors have found in previous experiments that the main factor affecting protein or cellular adhesion is the surface chemistry, the electronegativity of the surface in particular, which based on the results is the substrate's electronegativity.

The electronegativity of the surface is important because egg white protein is rich in albumen, which is attracted to electronegative surfaces. The electronegativities of the Si and Ti are 1.9 (163, 164) and 1.5 (163, 165) respectively. The higher electronegativity of Si would explain way it has higher protein adhesion than Ti.

# CHAPTER V

## INTERACTIONS OF BIOMOLECULES AND NANOPARTICLES

This chapter discusses the mechanisms of interfacial interactions between biomolecules and nanoparticles. The interaction between functionalized (positively and negatively charged) nanoparticles and proteins will be studied. Albumin is the most common protein in the body, making it the protein of choice. Emphasis will be placed on the effect of NP on protein flow properties – viscosity in particular. The positively and negatively charged gold nanoparticles are also mixed with amino acid solutions to further simplify the system under study and to observe the interaction mechanisms that occur. Two positively charged amino acids, L-arginine and L-lysine, are mixed with negatively charged gold nanoparticles. Two negatively charged amino acids, L-glutamic acid and L-aspartic acid, are mixed with positively charged gold nanoparticles. These four amino acids were selected because they are the main building blocks of albumin protein.

The viscosity is studied with a cone-and-plate rheometer as described in Chapter III. We address the effects of nanoparticle surface charge (positive and negative), nanoparticle size (10, 20 and 50nm), and nanoparticle solution concentration (33 and 67% by volume of NP solution) on the flow properties. All tests were conducted at 25$^{o}$C.

## 5.1. Gold nanoparticle/bovine serum flow properties

### 5.1.1. The NP/bovine serum viscosity

The flow properties of the base materials used (DI water, bovine serum, and nanoparticle solutions) must be identified first. Figure 58 shows the dynamic viscosity of the DI water and bovine serum. The viscosity of bovine serum is approximately twice of that of DI water. This significant increase in viscosity, 2.04 times higher (17.5 x$10^{-4}$ Pa.s for bovine and 8.54 x $10^{-4}$ Pa.s for DI), is expected since the molecules (proteins, and salts) in bovine serum increase its viscosity as nanofluid theories predict (67, 70, 166, 167).

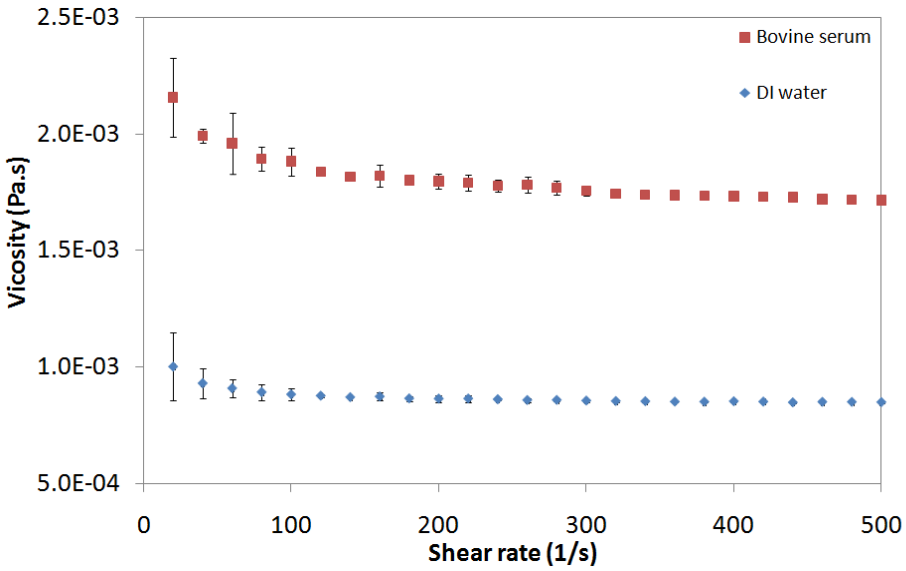


Figure 58 Viscosity of bovine serum and DI water

The viscosity of the positive gold (PG) and negative gold (NG) nanoparticle solutions are presented in Figures 59 and 60 respectively. The viscosity of DI water is added for comparison. In these figures, the viscosity depends on the shear rate. The high

viscosity at shear rates below 200 $s^{-1}$ is caused by the high spindle inertia to begin rotation. After 200$s^{-1}$, the rheometer has established a steady rotation resulting in a steady viscosity measurement.

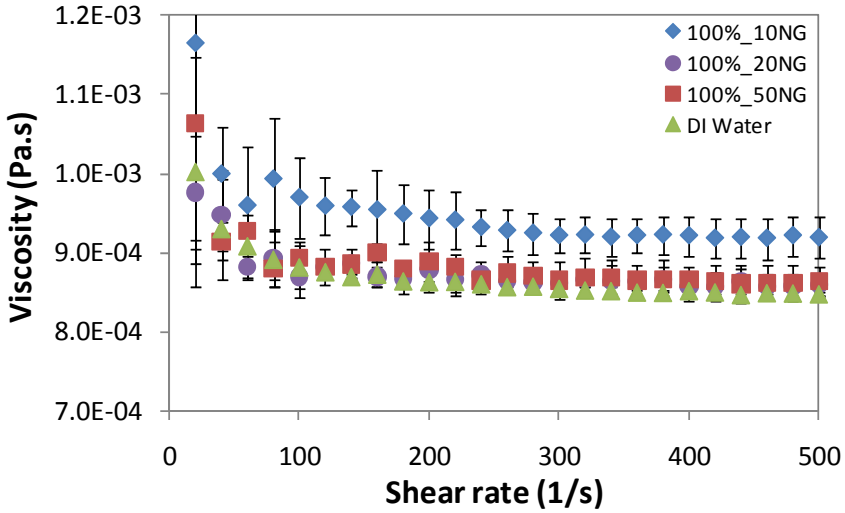


Figure 59 Dynamic viscosity of negative gold nanoparticle solutions (NP suspended in DI water)

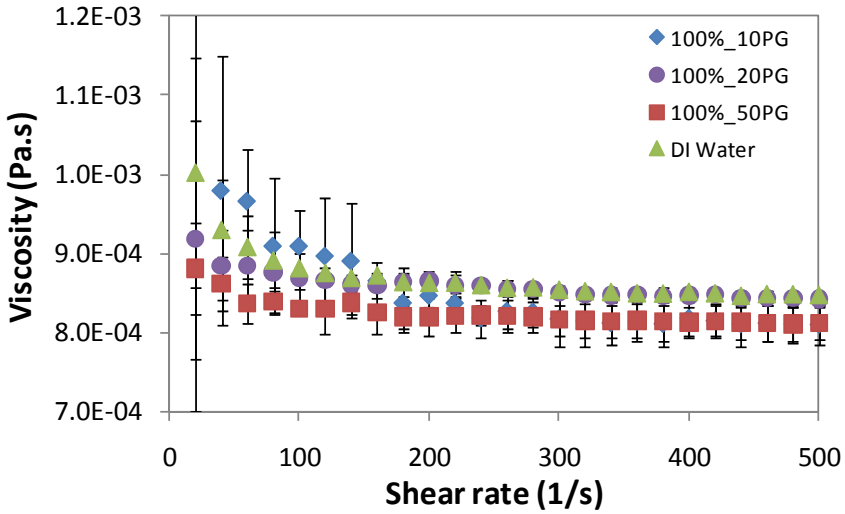


Figure 60 Dynamic viscosity of positive gold nanoparticle solutions (NP suspended in DI water)

The 10NG, 20NG and 10PG solutions changed in color from light pink to light purple, similar to the 10PG and 10NG shown in Figure 61. These NP solutions could cause agglomeration issues for NP/amino acid solutions as well.

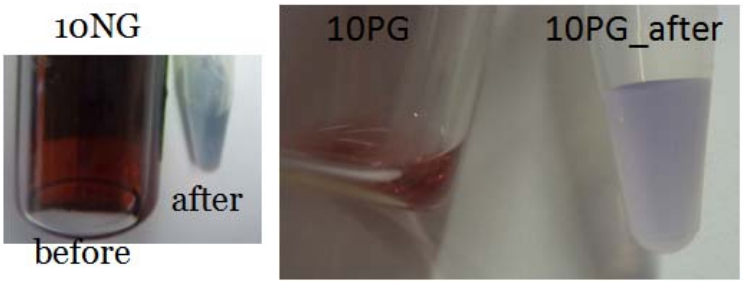


Figure 61 The 10nm positive gold solution changed color from light pink to light purple

According to nanofluid theories, the viscosity of the nanoparticle solutions increases with increasing nanoparticle size (67, 70, 166, 167). In the present study, the measured viscosities for positive and negative solutions indicate otherwise. The reason for this is the small %volume of solid nanoparticles in the solution. Based on the average nanoparticle size and concentration, the estimated % of solid volume occupied by the gold nanoparticles in the solution is <<1% (maximum estimated at 0.001% for the 10nm positive solution). The existing nanofluid viscosity theories have been proven effective only for nanoparticle solid volumes of 0.1% or higher (118). For such a diluted solid NP volume, the viscosity of the nanoparticle solutions were supposed to be equal to that of DI water, which is only true for the 20nm positive gold solution in Figure 58 above. This shows the high sensitivity of our test system. Most importantly, the differences in viscosity values seem to be independent of the nanoparticle size.

Now we examine the viscosity of the NP/bovine serum. The results for the 10, 20, and 50nm NG in bovine serum are summarized in Figures 62a-c. The results for the 10, 20 and 50nm PG in bovine serum are summarized in Figures 63a-c.

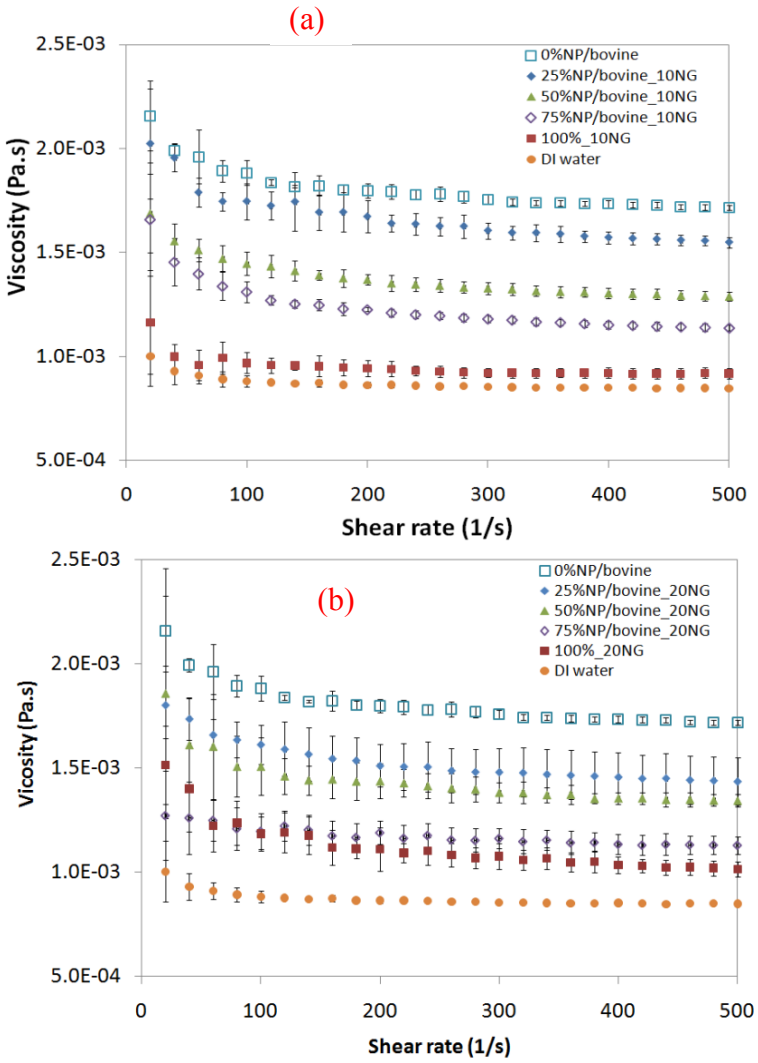


Figure 62 Viscosity of (a)10, (b)20, and (c)50 nm negative gold nanoparticles in bovine serum

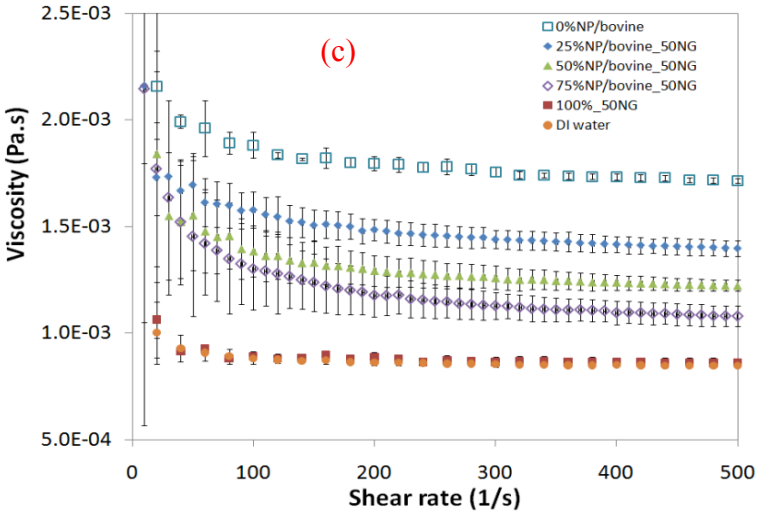


Figure 62 Continued

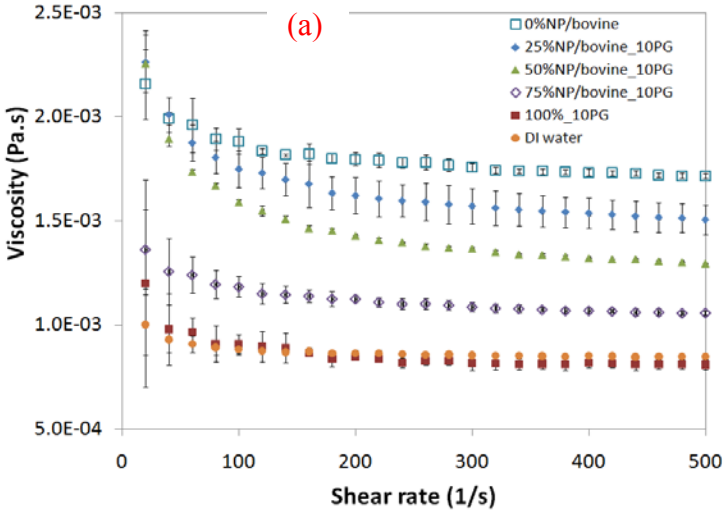


Figure 63 Viscosity of (a)10, (b)20, and (c)50nm positive gold nanoparticles in bovine serum

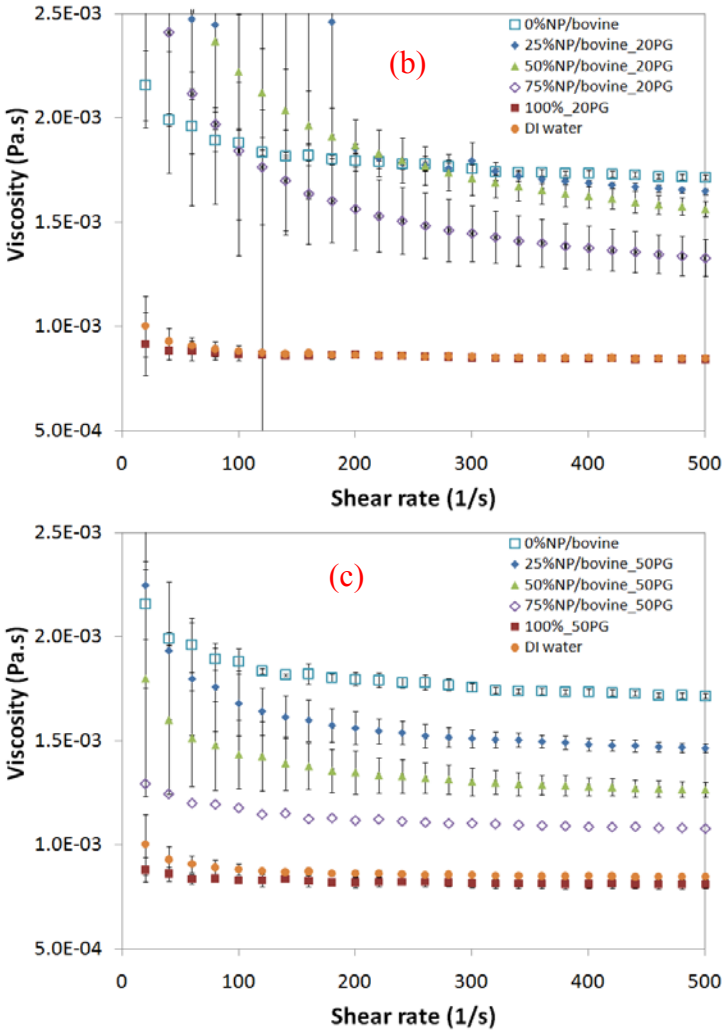


Figure 63 Continued

### 5.1.2. NP-bovine viscosity model

The results show that, in general, the viscosity of the mixed solutions falls within that of the nanoparticle solution (100%_XXNG) and the bovine serum (0%NP/bovine). The viscosity values are analyzed with respect to the % NP solution volume. The NP solution refers to the NPs suspended in DI water. The viscosity values reported are the

average of the values recorded for 200-500 $s^{-1}$ applied shear rate. The results are summarized in Figures 64a-c and 65a-c for NG and PG respectively.

The models used to predict the viscosity of liquid mixtures are generally exponential or logarithmic (168). On the contrary, our results showed a linear behavior for most mixtures, with the exception of the 20PG. The viscosity values of the mixtures (25, 50, and 75%) clearly show a linear viscosity behavior falling between those of the constituents (100%NP/bovine and 0%NP/bovine).

The linear viscosity behavior can be modeled with the simple equation used to calculate other properties, like density, of mixed liquid solutions. The viscosity of the mixture depends on the volume fractions and viscosity of the components.

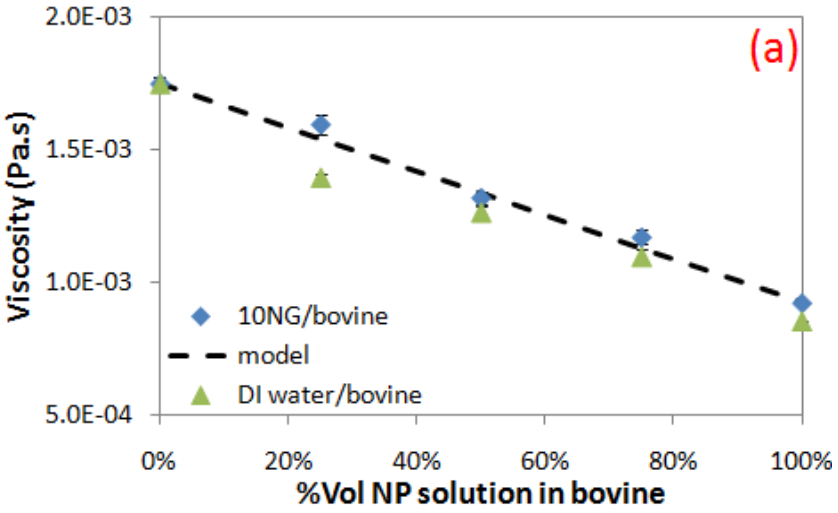


Figure 64 Viscosity changes linearly with respect to the % of nanoparticle solution. The dashed line is the model based on equation

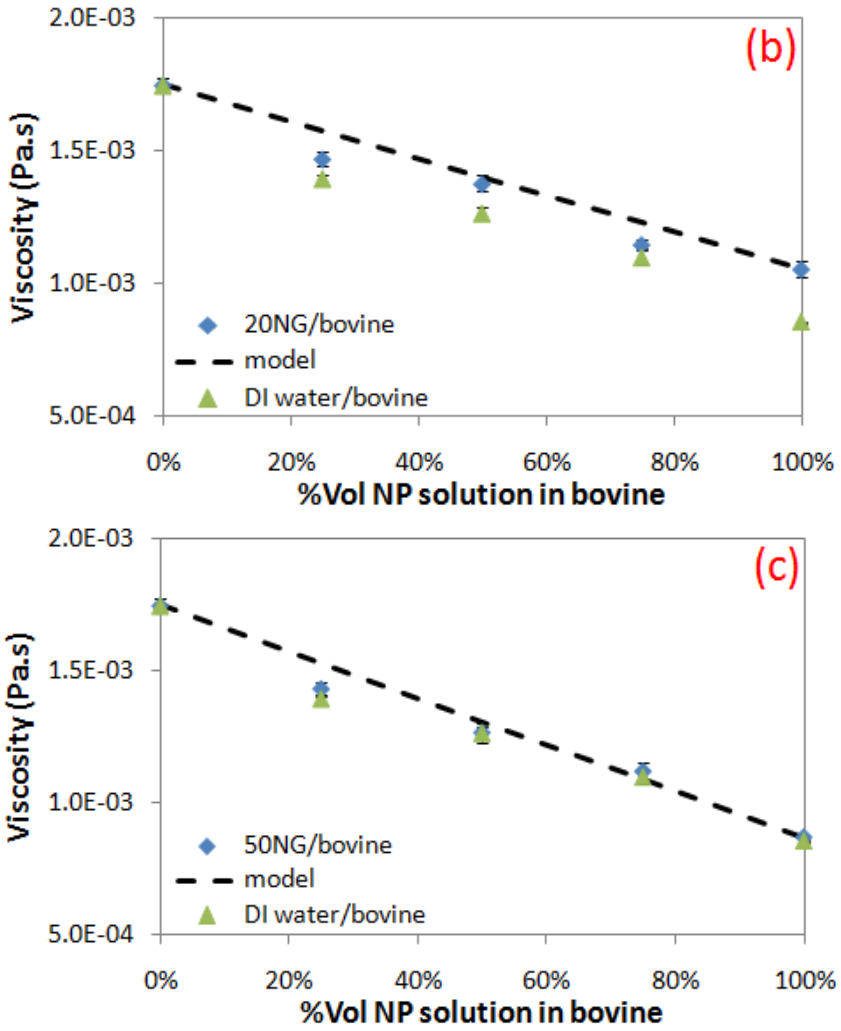


Figure 64 Continued

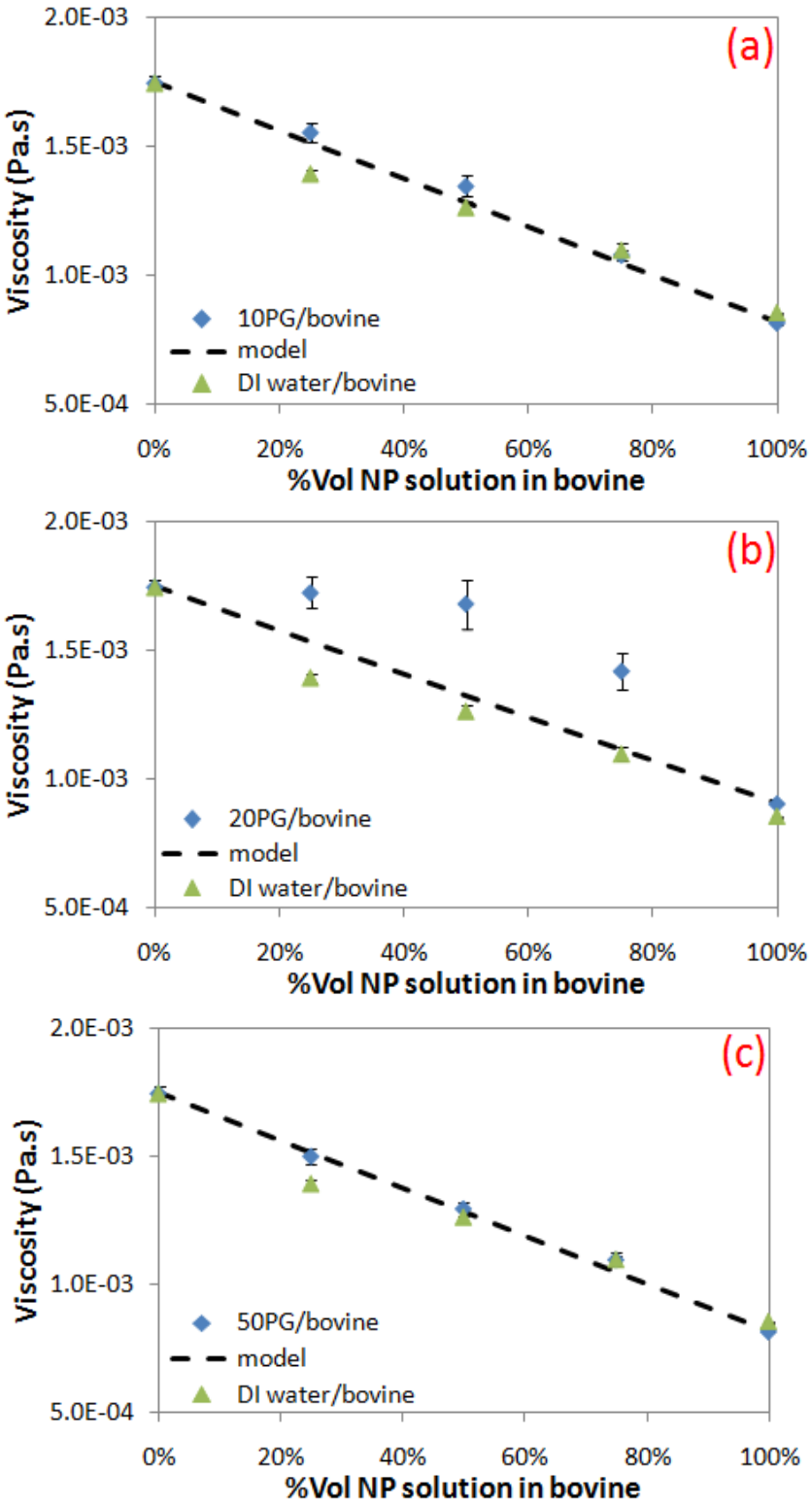


Figure 65 Viscosity changes linearly with respect to the % of nanoparticle solution, except for the 20PG solution. The dashed line is the model based on equation

The model is represented in Equation 10. This model is the one used for Figures 64 and 65.

$$\eta_{solution} = \eta_{NP} v_{NP} + \eta_{aa} v_{aa} \quad [10]$$

where $\eta_{NP}$ is the viscosity of the nanoparticle solution, $\eta_{aa}$ is the viscosity of the amino acid solution, $v_{NP}$ is the % nanoparticle solution volume, and $v_{aa}$ is the % amino acid solution volume. It means that the viscosity of the solution ($\eta_{solution}$) depends on the constituents.

Furthermore, the viscosity of the NP/bovine solutions is similar to that of the DI water/bovine solutions, also shown in Figures 64 and 65. This indicates that for the complex system used (bovine serum), the nanoparticle has little effect on the viscosity. The flow behavior depends largely on the dilution of the bovine serum by the DI water from the NP solutions. The reason for this behavior is due to the complex composition of the bovine serum discussed in Chapter III, section 3.1.3.2.2.

The only mixtures that do not follow the linear behavior according to Equation 10 are those of the 20PG/bovine solutions. The viscosity of the mixture follows the behavior identified by Kuleznev and colleagues for mixtures of polymers with low molecular weight distribution, i.e. a polydispersity index (PDI) approximately equal to 1 (168). It is well known that proteins have a PDI≡1.0 (169) According to Kuleznev's work, the viscosity of the mixture can be calculated as follows:

$$\eta_{mixture} = \left(\eta_1^{\frac{1}{\alpha}} w_1 + \eta_2^{\frac{1}{\alpha}} w_2\right)^{\alpha} \quad [11]$$

In this equation, $\eta_1$ and $\eta_2$ represent the viscosities of the solutions (NPs and bovine), $w_1$ and $w_2$ indicate the constituent weight fractions (NPs and bovine), and $\alpha$ is the dependence of the melt viscosity on the molecular weight according to: $\eta = KM^{\alpha}$ (168). For this study, the value of $\alpha$ was calculated using Equation 11 on the measured viscosity of the 20PG/bovine mixtures. Based on Equation 11, our calculated $\alpha \approx 0.12$ but the $\alpha$ value is typically 1 or 3.4 for polymeric materials.(169)

The physical meaning of α depends on the conformation of the polymer chain, where $\alpha$=1 indicates linear polymerization of the polymer and for $\alpha$=3.4 is due to polymer chain entanglements (169). The lower α value is likely attributed to protein conformation changes caused by their interaction with the nanoparticle.

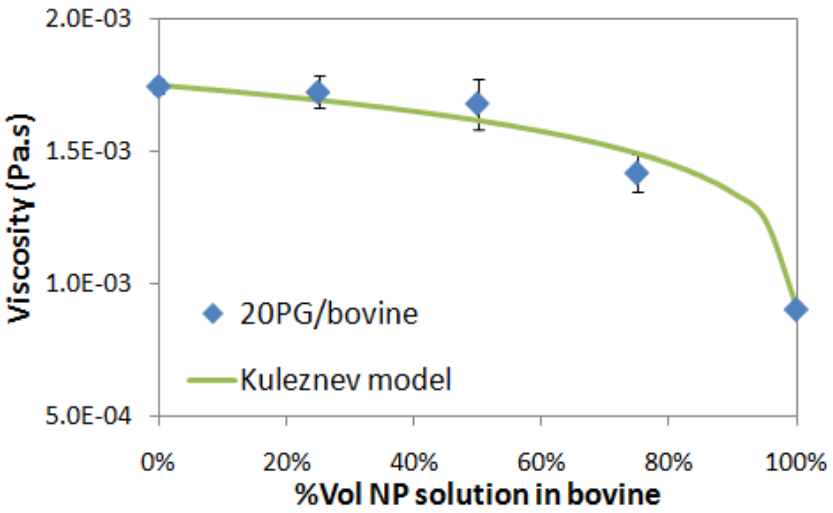


Figure 66 Viscosity model for polymer mixtures with low PDI provide a better fit to the 20PG/bovine mixture

The results indicate that the NP/protein interactions might be present and these affect the protein conformation, as shown in Figure 66. However, given the small solid

volume of nanoparticles present (<0.001%), the NP/protein interactions are generally overpowered by the complex composition of the bovine serum and the observed flow behavior, as shown in Figures 64a-c and 65a and c, only depends on the dilution of the bovine serum. This is further evidenced by the significant size difference between the bovine serum components and the nanoparticles. Figure 67 is a TEM image of the NP/bovine serum solution. The arrows indicate the location of some nanoparticles.

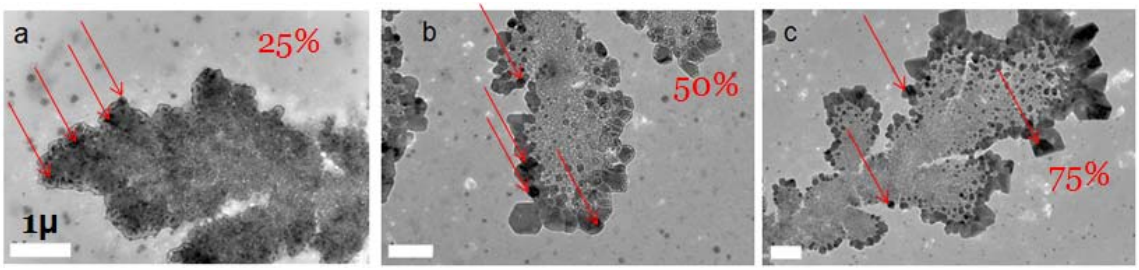


Figure 67 TEM image of NP/bovine serum solutions. The arrows indicate the location of NPs in the solution (courtesy of Subrata Kundu and Juhi Baxi)

It is clear that the nanoparticle size is significantly smaller than the proteins and salts present in the bovine serum solution. In order to study the NP/protein interactions, the system of study must be simplified. We will address this by using amino acids (those discussed in section 3.1.3.3. in Chapter III).

### 5.2. Nanoparticle-amino acid flow properties

The flow properties of single amino acid /NP solutions are studied. The amino acids selected are L-lysine, L-arginine, L-glutamic acid, and L-aspartic acid which are the main building blocks of albumin. The details of the amino acids selected are given in Chapter III, section 3.1.3.3.

The limitation of the NP/bovine serum studies was the discrepancy in size of its components. The spherical NPs used are 10, 20, and 50nm in diameter while the proteins in the bovine serum are in the micron size according to Figure 67. We calculated that a single amino acid molecule is approximately 1nm in length for the ones selected for this study. The proximity in NP/amino acid size is expected to encourage a stronger interaction. Furthermore, two amino acids selected are positively charged (L-lysine and L-arginine) and two are negatively charged (L-glutamic acid and L-aspartic acid), which are expected to interact with the negatively and positively charged nanoparticles respectively. The material combinations that will be tested are detailed in Table 6 of Chapter III.

### 5.2.1. Viscosity of amino acid

The viscosity was tested using the same method as for NP/bovine solutions. The viscosities of the NP solutions have been presented in Figure 59 for all NG and in Figure 60 for all PG nanoparticles. The viscosity of the amino acid solutions are summarized in Figures 68a-d for the selected amino acid concentrations, $1x10^{-2}$ and $1x10^{-4}$ mol/L labeled as 02 and 04 respectively. The amino acids are identified as follows: L for L-lysine, A for L-arginine, GA for L-glutamic acid, and AA for L-aspartic acid. Sample labeling is explained in detail in section 3.2.2 in Chapter III.

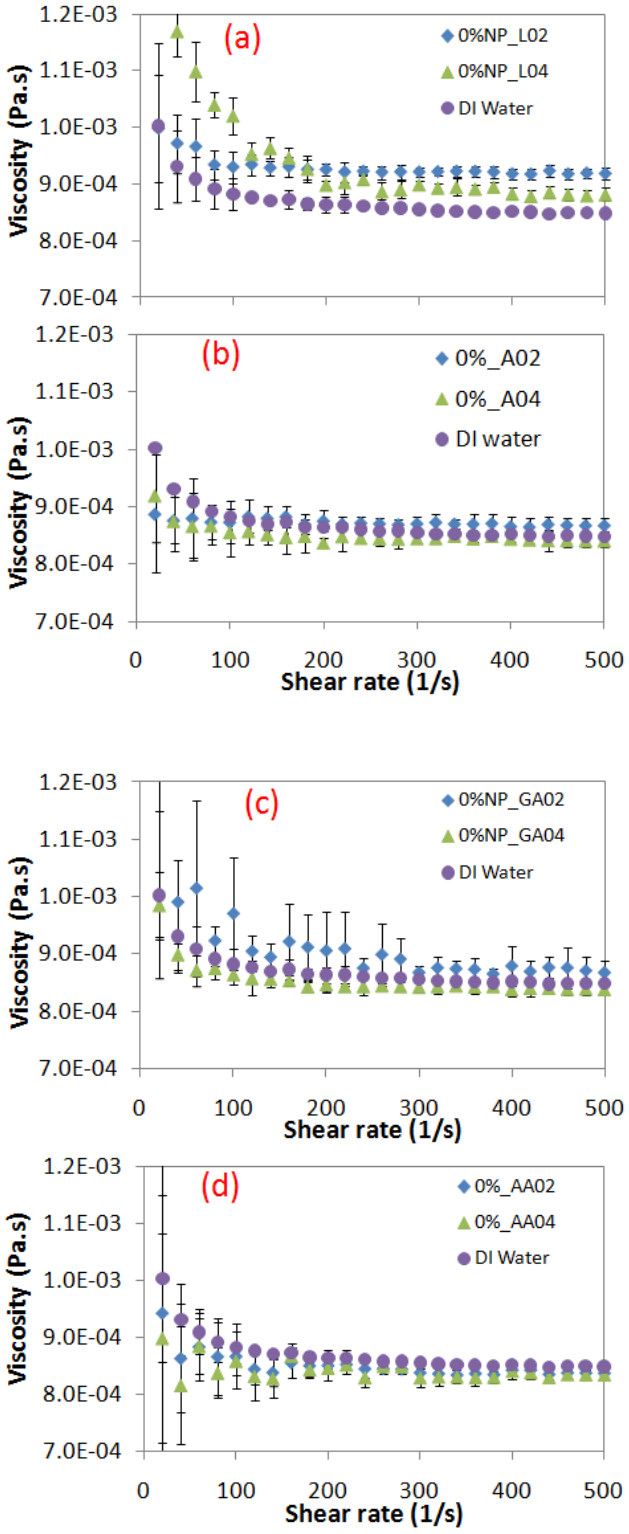


Figure 68 Viscosity for (a) L-lysine, (b) L-arginine, (c) L-glutamic acid, and (d) L-aspartic acid at the two concentrations: $1x10^{-2}$ and $1x10^{-4}$ mol/L. The values are compared to DI water

The viscosity of all the amino acid solutions is different than the viscosity of the DI water. Temperature and pH have been identified as the two main factors that affect viscosity (67, 71, 170-172). The effect of temperature is eliminated by testing all samples at 25$^{o}$C. The amino acid viscosity is analyzed with respect to its pH. The results are presented in Figure 69. The viscosity values are an average of the viscosity measured for the shear rates from 200 to 500 $s^{-1}$; the same used for bovine serum analysis.

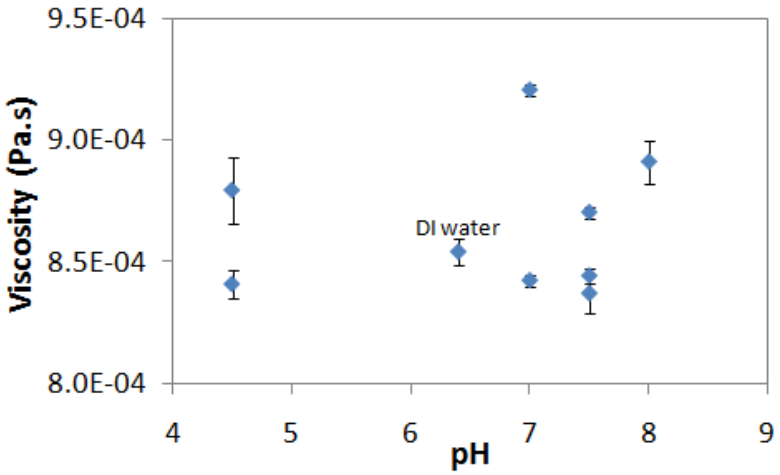


Figure 69 The amino acid viscosity is independent of its pH

Although Figure 69 clearly demonstrates the amino acid viscosity is independent of its pH, we must keep in mind that the amino acid solutions with low pH will generally be more unstable (i.e. the materials in these solutions will be more likely to agglomerate). The solutions with low pH values are the GA02 and AA02.

### 5.2.2. Viscosity of negative gold/L-lysine

The measured viscosity for the NG/L solutions are summarized in Figures 70a-c for the 10, 20, and 50nm negatively charged gold nanoparticles. The results indicate an

increase in viscosity with increasing NP size where the solutions mixed with 50NG are the most stable. The viscosity of the 10NG/L samples is similar to that of DI water (Figure 70a). The viscosity of the 20NG/L samples, Figure 70b, show a slightly higher but clear increase in viscosity while the 50NG/L samples in Figure 70c show a significant increase in viscosity.

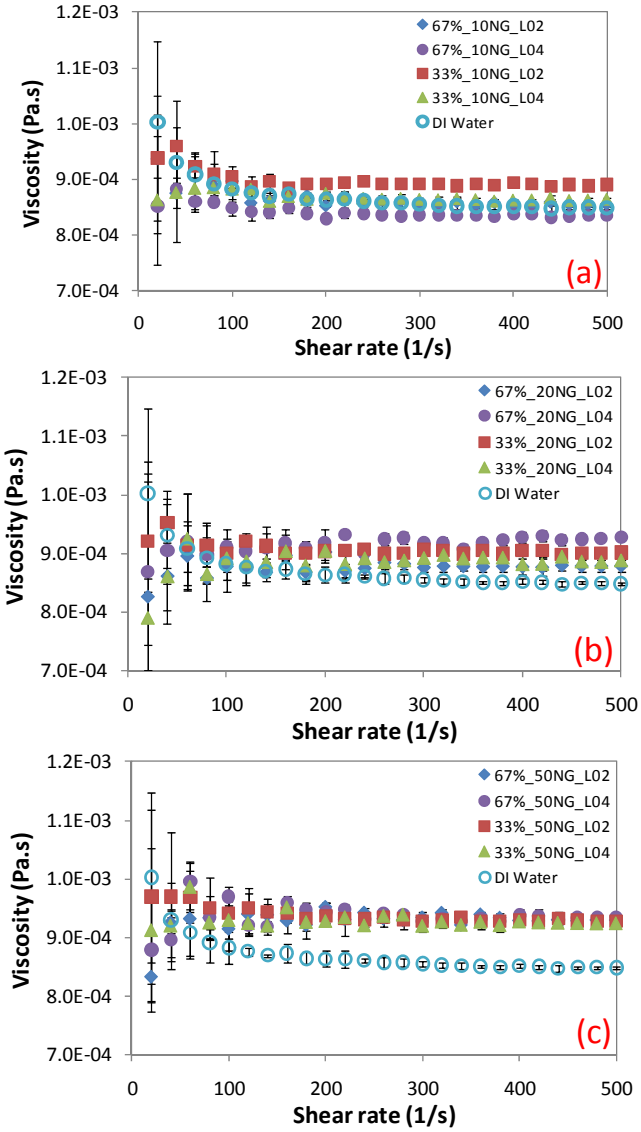


Figure 70 L-lysine solutions with (a) 10nm, (b) 20nm, and (c) 50nm NG solution viscosities

We must point out that most solutions aggregated before or during the viscosity test (i.e., the solutions changed from pink to light purple). These solutions are listed in Table 10. In general, the solutions with the highest amino acid concentration (L02= 0. 01 mol/L) are the ones with higher tendency to agglomerate.

Table 10 Solutions that agglomerated before or during testing

| sample | NP (nm) | Amino acid concentration (mol/L) | NP solution concentration (% soln vol) |
|---|---|---|---|
| 33%_10NG_L02 | 10 | 0.01 | 33% |
| 67%_10NG_L02 | 10 | 0.01 | 67% |
| | | | |
| 33%_20NG_L02 | 20 | 0.01 | 33% |
| 33%_20NG_L04 | 20 | 0.0001 | 33% |
| 67%_20NG_L02 | 20 | 0.01 | 67% |
| 67%_20NG_L04 | 20 | 0.0001 | 67% |
| | | | |
| 33%_50NG_L02 | 50 | 0.01 | 33% |
| 33%_50NG_L04 | 50 | 0.0001 | 33% |
| 67%_50NG_L02 | 50 | 0.01 | 67% |
| 67%_50NG_L04 | 50 | 0.0001 | 67% |

### 5.2.3. Viscosity of negative gold/L-arginine

The measured viscosity for the NG/A solutions are summarized in Figures 71a-c for the 10, 20, and 50nm negatively charged gold nanoparticles. With the exception of the 33%_10NG_A04, all others have a consistently higher viscosity than DI water. Figure 72 indicates that agglomeration of the 33%_10NG_A04 happened during testing given the change in solution color.

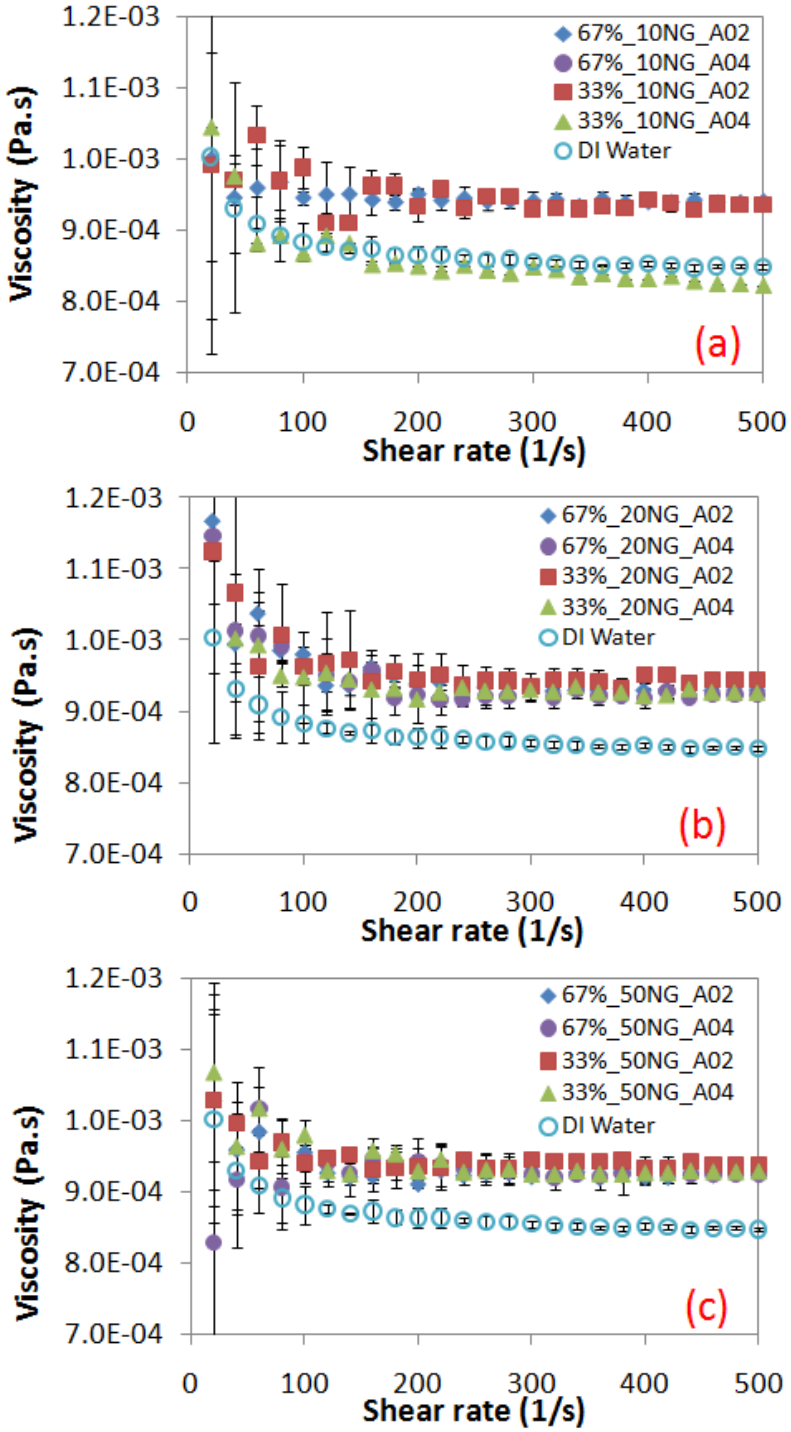


Figure 71 Viscosity of L-arginine solutions with (a) 10nm, (b) 20nm, and (c) 50nm NG solutions

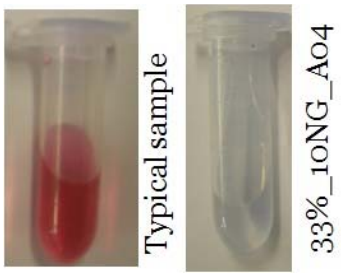


Figure 72 NP agglomeration in evidenced by the change in solution color after testing

Other solutions agglomerated when mixed. Table 11 summarizes all NG/A that agglomerated when mixed (i.e. prior to viscosity testing).

Table 11 List of solutions that agglomerated when mixed

| sample | NP (nm) | Amino acid concentration (mol/L) | NP solution concentration (% soln vol) |
|---|---|---|---|
| 67%_10NG_A02 | 10 | 0.01 | 67% |
| 67%_10NG_A04 | 10 | 0.0001 | 67% |
| 33%_20NG_A02 | 20 | 0.0001 | 33% |
| 33%_50NG_A02 | 50 | 0.01 | 33% |
| 33%_50NG_A04 | 50 | 0.0001 | 33% |
| 67%_50NG_A02 | 50 | 0.01 | 67% |
| 67%_50NG_A04 | 50 | 0.0001 | 67% |

### 5.2.4. Viscosity of positive gold/L-glutamic acid

The measured viscosity for the PG/GA solutions are summarized in Figures 73a-c for the 10, 20, and 50nm positively charged gold nanoparticles. The results show no clear trend with respect NP size, NP concentration, or GA concentration. It can be pointed out, however that there are samples with higher and lower viscosities than DI water. In

general, the 50nm PG solutions are the ones that show a lower viscosity values with respect to DI water.

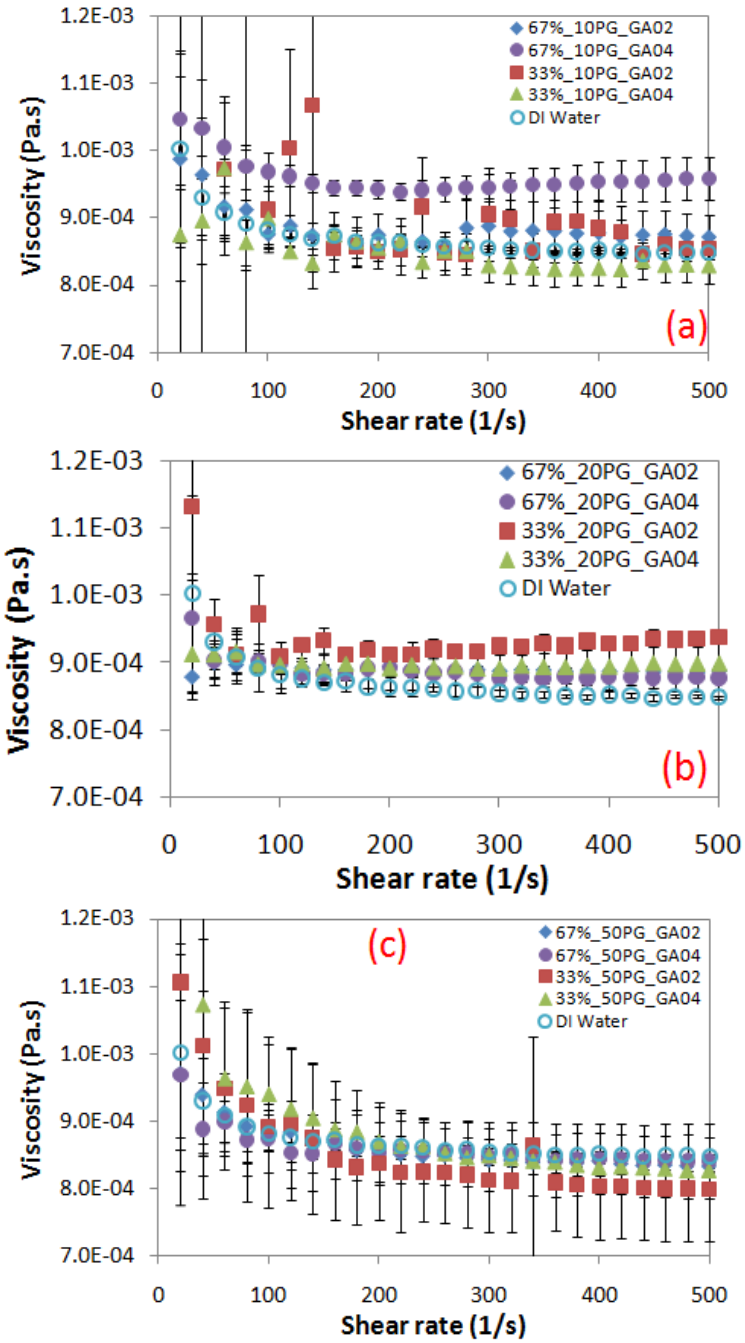


Figure 73 Viscosity of L-glutamic acid solutions with (a) 10nm, (b) 20nm, and (c) 50nm PG solutions

The only samples that agglomerated are the 33%_10PG_GA02 and the 67%_10PG_GA02, which according to Figure 73a, are the ones with the highest variation in measured viscosity because, as shown in Figure 68, GA02 is the least stable of all the amino acid solutions.

### 5.2.5. Viscosity of PG/L-aspartic acid

The measured viscosity for the PG/AA solutions are summarized in Figures 74a-c for the 10, 20, and 50nm positively charged gold nanoparticles. The 10 and 20nm PG solutions have the highest variation in viscosity with some samples above and some below the viscosity of DI water. The 10PG and 20PG solutions agglomerated during test which explains the inconsistent viscosity behavior. The samples that agglomerated are the 33%_10PG_AA02, 33%_10PG_AA04, and 67%_10PG_AA02.

Previous research shows gold nanoparticles are bonded with the CTAB surfactant through covalent Au-N bonding (173). The CTAB surfactant is used to make the negative gold nanoparticles. Tri-sodium citrate is the surfactant used to make the positively charged gold nanoparticles. Previous study has reported that there is a weak bonding for NP/citrate interaction, mainly  van der Waals or electrostatic forces (174).

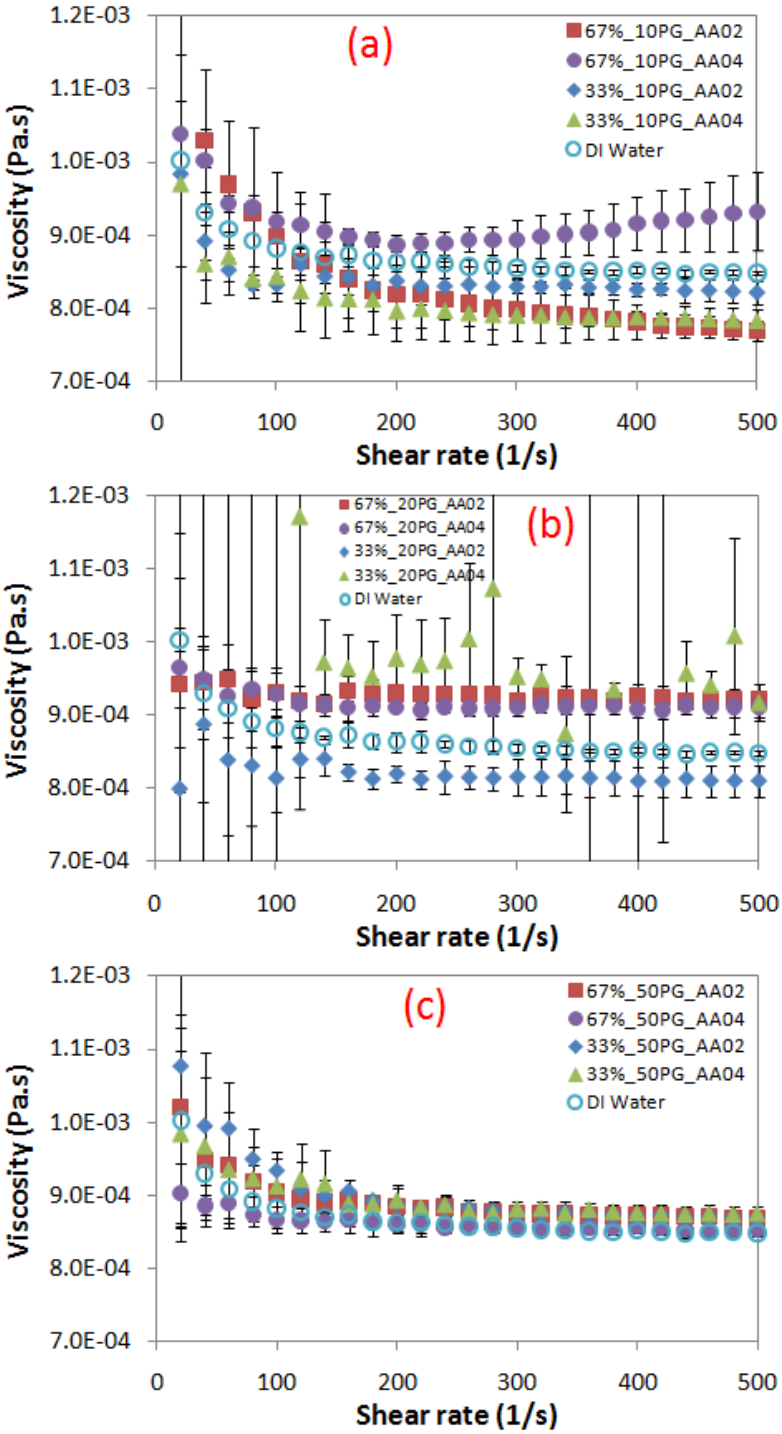


Figure 74 Viscosity of L-aspartic acid solutions with (a) 10nm, (b) 20nm, and (c) 50nm PG solutions

We conducted structural analysis of the molecules. XPS was performed after viscosity measurement. The samples were tested at the SSNL beam line 8.0. The results were analyzed with XPS Peak. Shirley background correction was used. The organic peaks were fitted according to the values reported by Ratner and Castner (175).

Figure 75a is the XPS results for the 67%_20NG_L02. This sample showed a viscosity of $8.8 \times 10^{-4}$ Pa.s, 3.0% higher than DI water. The peaks found correlate well with the composition of the amino acid (lysine) and the surfactant (citrate) used to provide the nanoparticle's negative surface charge. The structure of the amino acid and surfactant are given in Figures 75 b and c respectively. The peak analysis is summarized in Table 12. The % area for each peak correlates to the number of bonds present in the solution where a higher percentage indicates this molecule (i.e. bonding) is the most abundant. The results for the Peak 2 with 34% peak area at 286.5eV for –C–O–C– bonding show that it is the most abundant. This, however, is not a molecule present in lysine or citrate, we can infer this is due to citrate polymerization.

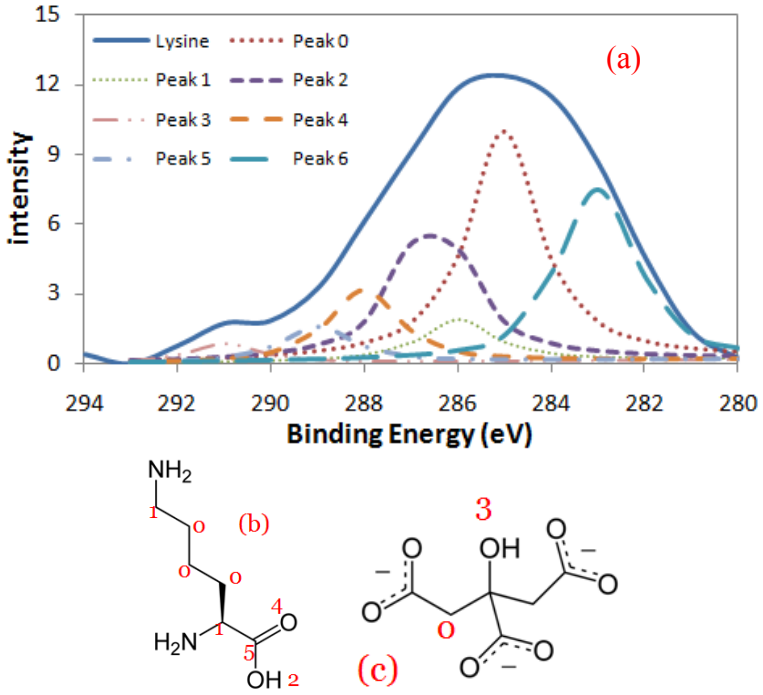


Figure 75 (a) XPS results for negative gold/ lysine solution, (b) lysine molecule, (c) NP surfactant molecule (citrate)

Table 12 Peak analysis for negative gold/lysine solution

| Peak | Position (eV) | Area | % area | FWHM (eV) | %GL | | |
|---|---|---|---|---|---|---|---|
| 0 | 285 | 16.521 | 22% | 1.8 | 100 | C-C | C-H |
| 1 | 286 | 2 | 3% | 1.8 | 100 | C-N | |
| 2 | 286.5 | 25.808 | 34% | 1.8 | 100 | -C-O-H, | -C-O-C |
| 3 | 283 | 19.309 | 25% | 2.3 | 0 | | |
| 4 | 288 | 8.624 | 11% | 1.8 | 80 | C=O | |
| 5 | 289 | 1.442 | 2% | 1.8 | 80 | O-C=O, | N<br>N-C=O |
| 6 | 291 | 2.595 | 3% | 1.8 | | | |

Figure 76a shows the XPS peaks for 67%_20NG_A02. This sample showed a viscosity of $9.3 \times 10^{-4}$ Pa.s, 9.2% higher than DI water. The structure of the amino acid and surfactant are given in Figures 76 b and c respectively. The peak analysis is summarized

in Table 13. The results for the Peak 3 with 14% peak area at 286.5eV for –C–O–C– indicates a decrease in the citrate polymerization compared to the lysine solution.

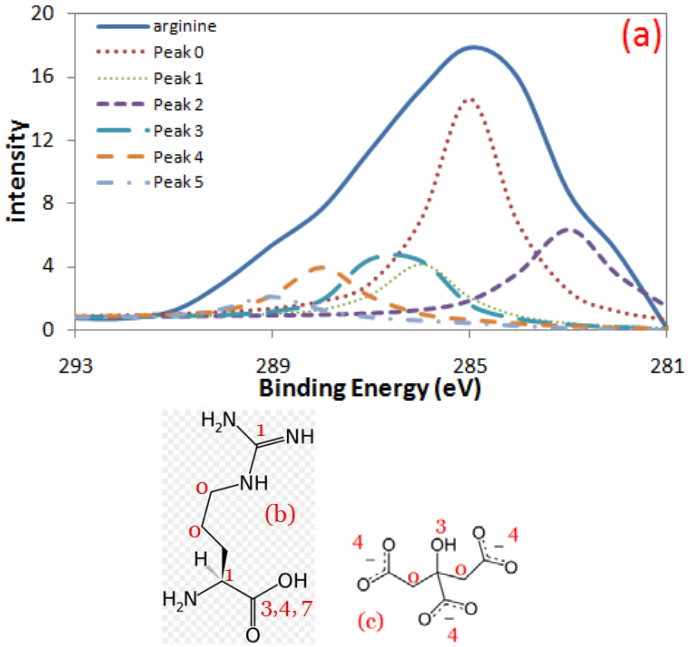


Figure 76 (a) XPS results for negative gold/ arginine solution, (b) arginine molecule, (c) NP surfactant molecule (citrate)

Table 13 Peak analysis for negative gold/arginine solution

| Peak | Position (eV) | Area | % | FWHM (eV) | %GL | | |
|---|---|---|---|---|---|---|---|
| 0 | 285 | 40.23 | 41% | 1.8 | 100 | C-C | C-H |
| 1 | 286 | 10.381 | 11% | 1.8 | 100 | C-N | |
| 2 | 283 | 21.627 | 22% | 2.204 | 100 | | |
| 3 | 286.5 | 13.455 | 14% | 1.8 | 80 | -C-O-H, | -C-O-C |
| 4 | 288 | 8.696 | 9% | 1.8 | 80 | C=O | |
| 5 | 289 | 3.672 | 4% | 1.8 | 80 | O-C=O, | N<br>N-C=O |

Figure 77a shows the XPS peaks for 67%_50PG_GA02. This sample showed a viscosity of $8.4x10^{-4}$ Pa.s, a 0.7% decrease in viscosity compared to DI water. The structure of the surfactant and amino acid are given in Figures 77 b and c respectively. The peak analysis is summarized in Table 14. The results for the Peak 3 with 22% peak area at 286.5eV for C–O–H indicates can be attributed to the COH at both ends of the glutamic acid molecule. Additionally, the 34% of Peak 1 at 285eV for the C-C bond is due to the long CTAB backbone structure. The results indicate a poor interaction between the NP surfactant and amino acid potentially contributing to the drop in viscosity.

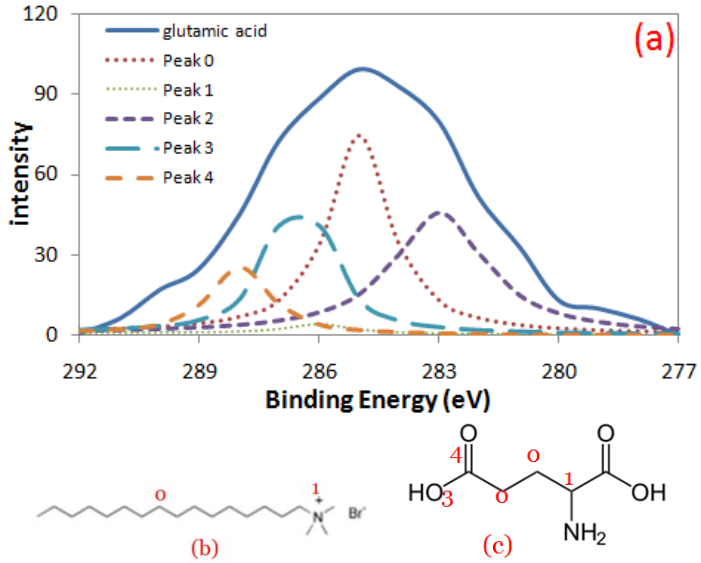


Figure 77 (a) XPS results for positive gold/ glutamic acid solution, (b) NP surfactant molecule (CTAB), (c) glutamic acid molecule

Table 14 Peak analysis for positive gold/glutamic acid solution

| Peak | Position (eV) | Area | % | FWHM (eV) | %GL | | |
|---|---|---|---|---|---|---|---|
| 0 | 285 | 210 | 34% | 1.8 | 100 | C-C | C-H |
| 1 | 286 | 10 | 2% | 1.8 | 100 | C-N | |
| 2 | 283 | 200 | 32% | 2.204 | 100 | | |
| 3 | 286.5 | 140.72 | 22% | 1.8 | 80 | -C-O-H, | -C-O-C |
| 4 | 288 | 65.023 | 10% | 1.8 | 80 | C=O | |

Figure 78a shows the XPS peaks for 67%_50PG_AA02. This sample showed a viscosity of $8.8 \times 10^{-4}$ Pa.s, 3.0% rise in viscosity compared to DI water. The structure of the surfactant and amino acid are given in Figures 78 b and c respectively. The peak analysis is summarized in Table 15. The results show no sign of amino acid/surfactant bonding.

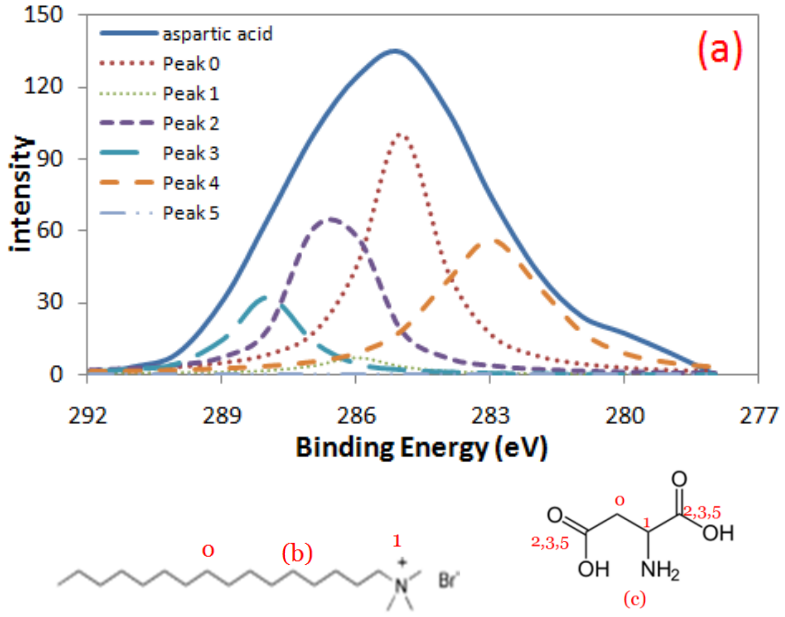


Figure 78 (a) XPS results for positive gold/ aspartic acid solution, (b) NP surfactant molecule (CTAB), (c) aspartic acid molecule

Table 15 Peak analysis for positive gold/aspartic acid solution

| Peak | Position (eV) | Area | % | FWHM (eV) | %GL | | |
|---|---|---|---|---|---|---|---|
| 0 | 285 | 284.26 | 34% | 1.8 | 100 | C-C | C-H |
| 1 | 286 | 18.522 | 2% | 1.8 | 100 | C-N | |
| 2 | 286.5 | 200.3 | 24% | 1.8 | 80 | -C-O-H, | -C-O-C |
| 3 | 288 | 84.696 | 10% | 1.8 | 80 | C=O | |
| 4 | 283 | 236.935 | 29% | 2.87 | 80 | | |
| 5 | 289 | 0.1 | 0.01% | 1.8 | 80 | O-C=O, | N<br>N-C=O |

The physical models and XPS results help determine the NP/amino acid interactions but the question of why the NPs and amino acids interact this way still remains unanswered.

### 5.3. Thermodynamic analysis of the NP/amino acid solutions

It is well known that materials maintain the lowest energy possible to exist. The NP and amino acid molecules will interact in solution until equilibrium is achieved. When materials are mixed this equilibrium is disrupted. The interaction of the mixed materials will depend on their energies. The thermodynamics of the NP/amino acid solutions are now analyzed to understand the energy changes that mixing brings to the system. We assume that the NPs-amino acid solutions are a closed system. The main focus will be the entropy change of the solutions ($\Delta S_{solution}$) and the number of possible NP/amino acid arrangements ($\Omega$).

Form the statistical thermaldynamics point of view, entropy (S) is the randomness in a system. For a material with a crystalline structure (highly organized molecules), the entropy will be low while the entropy of a gas (unorganized molecular arrangement) the

entropy will be high (169, 176). The entropy of a system is always positive. However, the change in entropy of a system can be negative if it goes from highly unorganized to highly organized (176-178).

The entropy of the amino acid solution will be altered as a result of the NP interaction. The change in entropy of the NP/amino acid system can be calculated based on the measured viscosity (71). First, the *B*-viscosity factor is determined with Equation 12. In this equation, $\eta_{rel}$ is the relative viscosity, $\eta_{solution}$ is the NP/amino acid solution viscosity, and $\eta_{NP}$ is the viscosity of the NP solution, *B* is the viscosity coefficient, and *c* is the amino acid concentration (mol/L). The *B*-coefficient is a measure of how much the viscosity of a solvent (i.e. the amino acid) is affected by a solute (i.e. the NP).

$$\eta_{rel} = \frac{\eta_{Solution}}{\eta_{NP}} = 1 + Bc \qquad [12]$$

Another important aspect is the Gibbs free energy ($\Delta G_{system}$), which can be considered the potential energy a system. For the system under study, there are two contributors to the $\Delta G$. The first is the NP. When the NP is dissolved in the amino acid solution, the NP brings some potential energy for its interaction with the amino acid. The second is the energy that the solution needs to flow. The viscosity is due to fluid molecule motion from one location to the next (i.e. flow), the energy required for this process can be interpreted as a form of $\Delta G$. Next, the Gibbs activation energy ($\Delta G_{NP}$) of one mole of pure solvent is calculated with Equation 13. In this equation, *R* (gas constant) = 8.314 J/mol.K, *T* is the temperature in Kelvin, $V_1$ is the partial molar volume of the solvent, *h* (Plank's constant) = $6.626 \times 10^{-34}$ J.s, and $N_A$ (Avogadro's number) = $6.022 \times 10^{23}$

molecules/mol. The $\Delta G_{NP}$ is the energy that the solvent (NP) must bring to initiate a reaction with the solute.

$$\Delta G_{NP}\,\frac{\mathrm{J}}{\mathrm{mol}} = RTln\left(\frac{\eta_{NP}V_1}{hN_A}\right) \quad [13]$$

The Gibbs activation energy per mole of solute ($\Delta G_{solution}$) is calculated with Equation 14. The effects of the solvent are also considered in this equation. $V_2$ indicates the partial molar volume of the solute. The $\Delta G_{solution}$ is the energy barrier that the fluid particle must overcome to flow.

$$\Delta G_{Solution}\,\frac{\mathrm{J}}{\mathrm{mol}} = \Delta G_{NP} + \frac{RT}{V_1}\left[B - (V_1 - V_2)\right] \quad [14]$$

The change in entropy of the solution ($\Delta S_{solution}$) is determined with Equation 15. The change in entropy refers to the organization of the NP and the amino acid from before to after mixing.

$$\Delta S_{Solution}\,\frac{\mathrm{J}}{\mathrm{mol.K}} = -\left(Rln\left(\frac{\eta_{NP}V_1}{hN_A}\right) + \frac{R}{V_1}\left[B - (V_1 - V_2)\right]\right) \quad [15]$$

Finally, the number of possible NP/amino acid arrangements (Ω) can be calculated using a variation of Boltzmann's approximation (169). In order to understand the meaning of Ω, assume we have 10 amino acid molecules and 10 nanoparticles. Also assume we have a total of 100 spaces where they can be placed. The Ω represents all the possible arrangements these NPs and amino acid molecules can take in the 100 spaces available. The higher Ω is, the less ordered the system will tend to be, making interactions more favorable. Equation 16 is used to calculate Ω, where k is Boltzmann's constant (1.380 x $10^{-23}$ J/K). This approximation can be used to calculate Ω for the entire solution.

$$\Delta S \frac{J}{K} = -k \ln \Omega \quad [16]$$

Our analysis, however, is based on one mole of solution. The correction to the equation comes from the relation between Boltzmann's constant ($k$) and the gas constant ($R$), $R=kN_A$. Using $R$ instead of $k$ allows us to calculate the Ω for one mole of solution. Therefore, Boltzmann's approximation is changed as follows:

$$\Delta S_{Solution} = -Rln\Omega \quad [17]$$

Proteins form organized structures that are highly dependent on their chemical composition. The ionic amino acids aid in the formation of the structure. This organization can be disrupted when an ionic solvent is added to the protein solution because the ionic amino acids will interact with the ionic solvent. This opening of the protein structure is a process called denaturation (71, 179-181).

The denaturation of proteins and amino acids by nanoparticles is a recent topic of study (19, 182, 183). Few reports have been found explaining how the amino acid denaturation affects its flow properties. This is an area that deserves attention because functionalized nanoparticles are usually delivered via the blood stream and the NPs can interact with the proteins found in blood.

The $\Delta S_{solution}$ of the NG/ lysine solutions are presented in Figure 79. The figure 79a shows the $\Delta S_{solution}$ is independent of viscosity for the solutions with low amino acid concentration (33%_L04 and 67%_L04). These solutions show $\Delta S_{solution}$ values as low as -1200 J/mol.K. The solutions with higher lysine concentration (33%_L02 and 67%_L02)

show a clear decreasing $\Delta S_{solution}$ trend with increasing viscosity. These solutions have $\Delta S_{solution}$ values ranging from -100 to -200 J/mol.K.

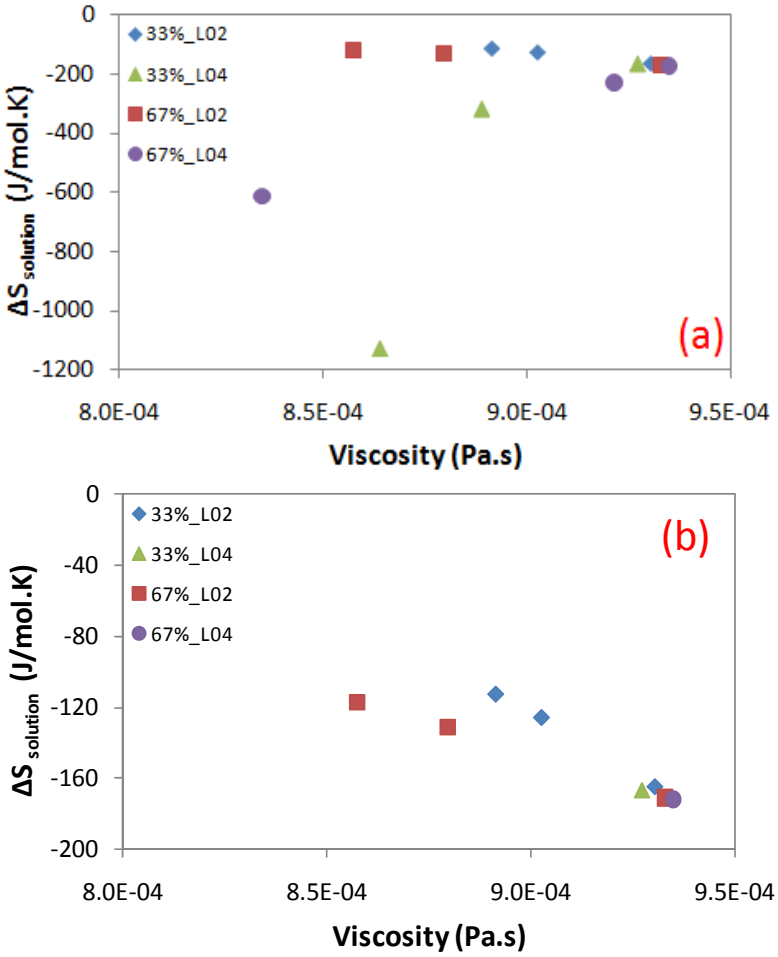


Figure 79 (a) Change in enthalpy of the negative gold/lysine solution (b) is a close up to enhance the trend at the lower ΔS values.

Figure 80 summarizes the calculated $\Delta S_{solution}$ for the NG/arginine solutions. The results show a slightly increasing trend in $\Delta S_{solution}$ with increasing viscosity. This system is the most stable and all calculated $\Delta S_{solution}$ values range from -100 to -140 J/mol.K.

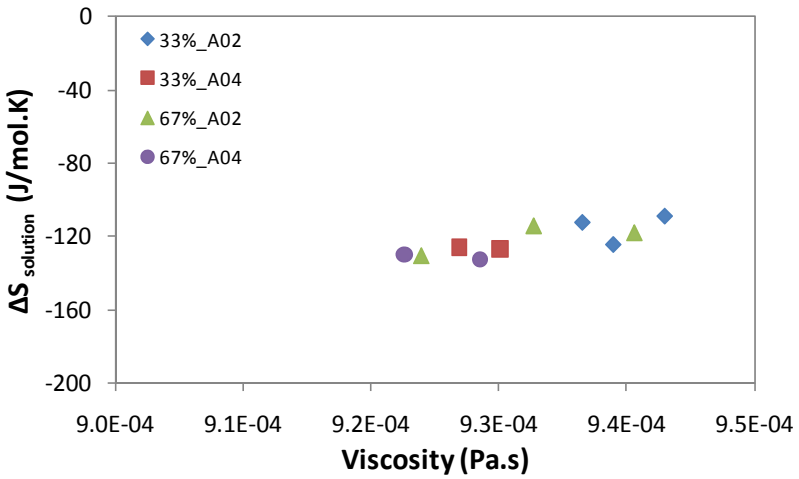


Figure 80 Change in entropy for the negative gold/L-arginine solution

Figure 81a shows the calculated $\Delta S_{solution}$ for the PG/glutamic acid solutions. Most calculated $\Delta S_{solution}$ values range from -100 to -200 J/mol.K. There are a few exceptions for the low amino acid concentration solutions (33%_GA04 and 67%_GA04), a behavior similar to that of NG/lysine. Figure 81b shows the $\Delta S_{solution}$ is independent of viscosity.

The calculated $\Delta S_{solution}$ for PG/aspartic acid solutions are summarized in Figure 82a. Most calculated $\Delta S_{solution}$ values range from -100 to -200 J/mol.K, Figure 82b is a close up to observe the lower $\Delta S_{solution}$ values. There is a clear decreasing trend with increase in viscosity. There are a few exceptions for the low amino acid concentration solutions (33%_AA04 and 67%_AA04), a behavior similar to that of NG/lysine and PG/GA.

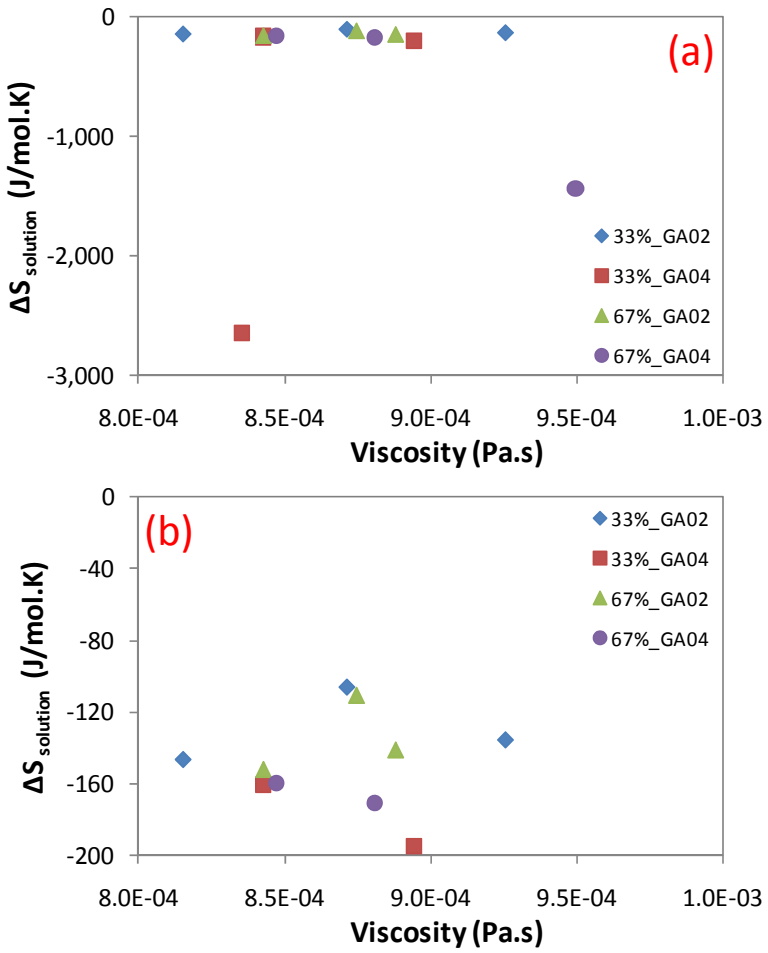


Figure 81 (a) Change in entropy for the positive gold / L-glutamic acid solutions (b) is a close up to enhance the trend at the lower ΔS values.

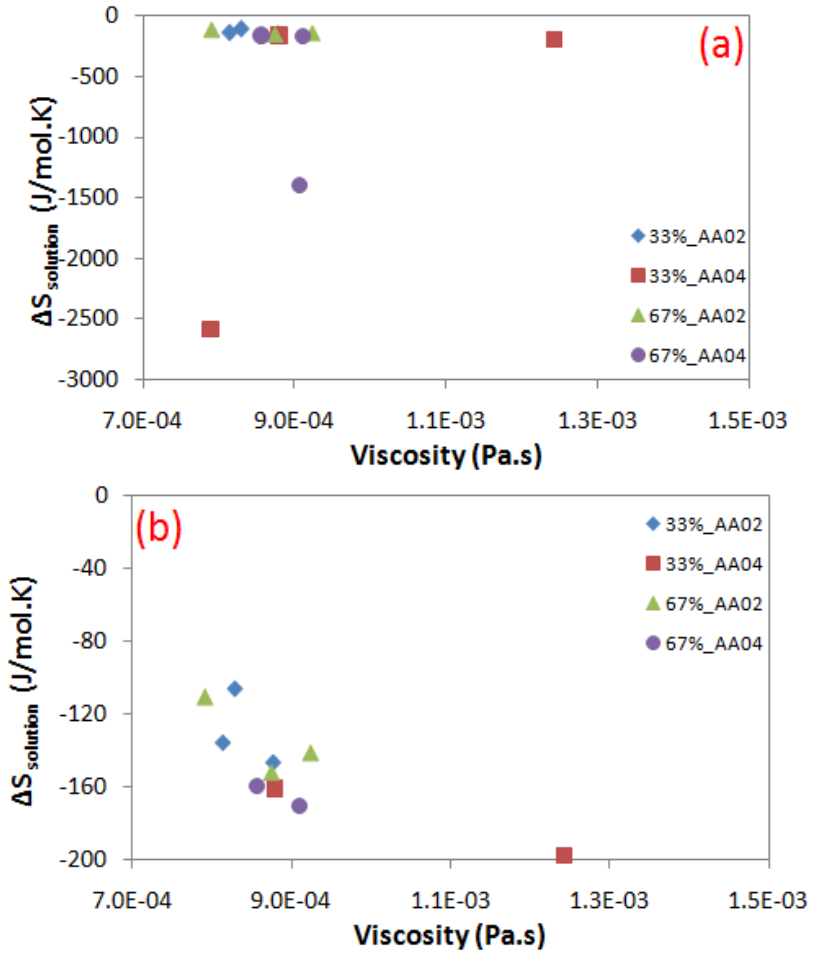


Figure 82 Change in entropy for the positive gold / L-aspartic acid solutions

The change in entropy is negative for all solutions, meaning that the systems become more organized due to the addition of NPs to amino acids. Most solutions have $\Delta S_{solution}$ ranging between -100 and -200 J/mol.K. The L-lysine, L-glutamic acid, and L-aspartic acid have a few samples with a $\Delta S_{solution}$ over -1000 J/mol.K. The minus sing means a reduction in entropy.

The Ω of the NP/ amino acid solutions are presented in Figures 83 to 85 for lysine, arginine, glutamic acid, and aspartic acid respectively. The Ω represents the many

different options in which nanoparticles and amino acid molecules can be distributed within the solution.

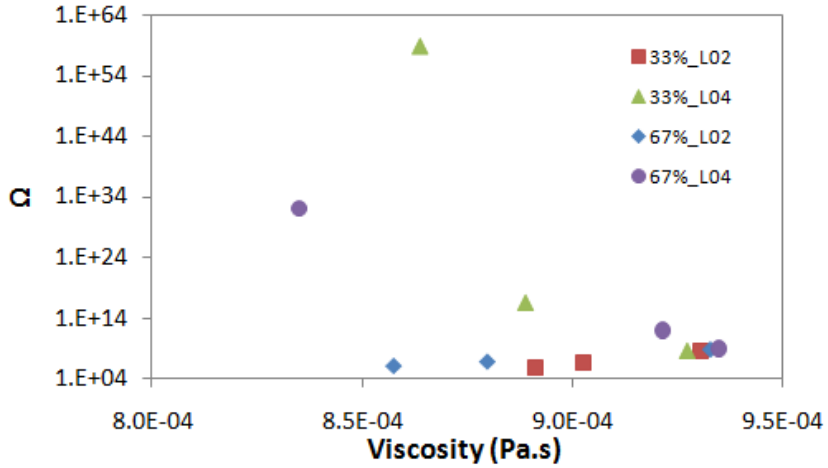


Figure 83 Number of possible NP/amino acid arrangements for negative gold/lysine solutions

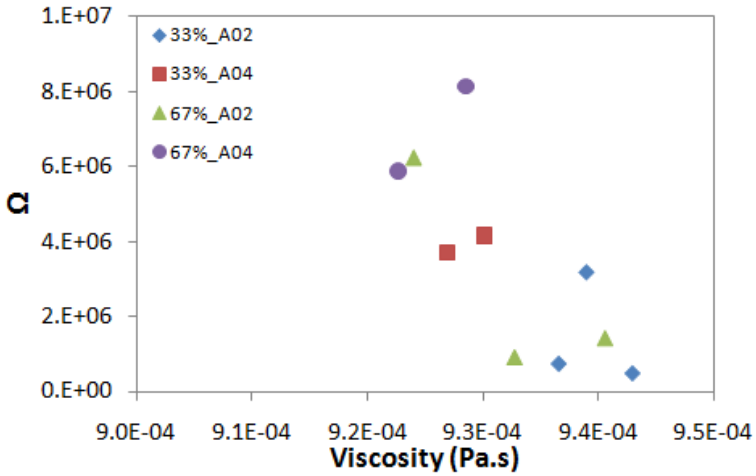


Figure 84 Number of possible NP/amino acid arrangements for negative gold/arginine solutions

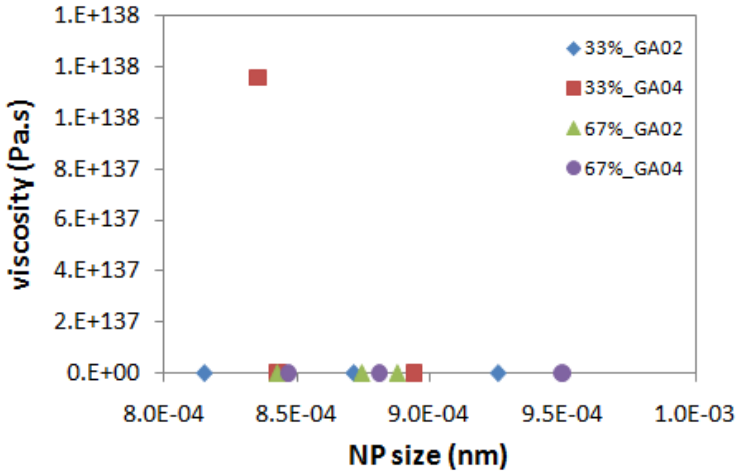


Figure 85 Number of possible NP/amino acid arrangements for positive gold/glutamic acid solutions

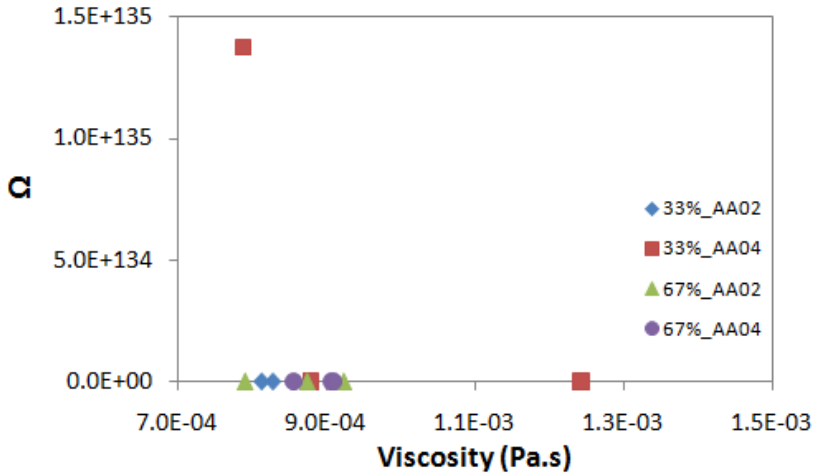


Figure 86 Number of possible NP/amino acid arrangements for positive gold/aspartic acid solutions

For most solutions, the number of potential nanoparticle/amino acid arrangements (Ω) range between $1x10^4$ to $1x10^{10}$. There are a few exceptions for lysine, glutamic acid, and aspartic acid where Ω values up to $1x10^{138}$ are calculated.

The solutions with high $\Delta S_{solution}$ and Ω have been analyzed with respect to NP size and concentration, amino acid concentration, and solution pH to identify the potential

reasons for this behavior. Two factors identify these solutions. The first is the 10nm sized nanoparticles (the smallest used in this study). Small nanoparticles are generally associated with higher surface to volume ratios which translate to higher total potential of the system. The second factor is the large # of NPs with respect to amino acid molecules. The samples that exhibit this behavior are identified in Table 16.

This behavior can be attributed to the strong nanoparticle effect on the amino acid structure and the higher surface energy of the 10nm sized particles leading to the higher total potential of the solutions. Furthermore, a low amino acid molecule/for each nanoparticle ratio, the more likely the solution is to interact, giving higher change in entropy ($\Delta S_{solution}$) and a higher number of possible nanoparticle/amino acid molecule arrangements ($\Omega$).

Table 16 Samples that exhibit large changes in entropy and number of possible arrangements

| sample | NP (nm) | # of NP/mL | Amino acid concentration (mol/L) |
|---|---|---|---|
| 33%_10NG_L04 | 10 | $2x10^{13}$ | 0.0001 |
| 67%_10NG_L04 | 10 | $2x10^{13}$ | 0.0001 |
| 33%_10PG_GA04 | 10 | $2x10^{13}$ | 0.0001 |
| 67%_10PG_GA04 | 10 | $2x10^{13}$ | 0.0001 |
| 67%_10PG_AA04 | 10 | $8x10^{12}$ | 0.0001 |
| 33%_10PG_AA04 | 10 | $8x10^{12}$ | 0.0001 |

## 5.4. NP/amino acid interaction mechanisms

The viscosity results presented in section 5.2 show independence from NP size, NP concentration, and amino acid concentration. Some solutions show viscosities higher than DI water and other show viscosities lower than DI water. Furthermore, the change in entropy of the solutions show different trends with respect to viscosity. What could be causing this behavior?

To address this question, we need to remember that viscosity is the drag force, i.e., the resistance, of the molecular layers in the liquid to move past each other and flow. The higher the resistance, the higher the measured viscosity will be. We propose physical models for this behavior.

There are three possible scenarios for the interaction between the NP and the amino acid. In the first model, the spherical model, we assume the polar amino acids selected interact with the charged NP by encapsulating it. This would form a self-assembled core of agglomerated NPs, surrounded by an amino acid layer, as illustrated in Figure 87a. A phenomenon identified as a protein corona (87).

In the second model, the agglomeration model, there are only NP-NP interactions (i.e. NP agglomeration) and amino acid-amino acid interactions (amino acid polymerization). The amino acid does not interact with the NPs. Instead, the amino acid polymerizes forming long, entangled chains instead of surrounding the nanoparticles, as illustrated in Figure 87b.

For the third model, the entangled model, the behavior is a mixture of models 1 and 2. The amino acid polymerizes forming long, entangled chains with few nanoparticles

dispersed in the amino acid chains. There are few NP-amino acid interactions. The organized molecule spreads further than that shown in Model 1 due to the excessive amino acid polymerization. The model is presented in Figure 87c.

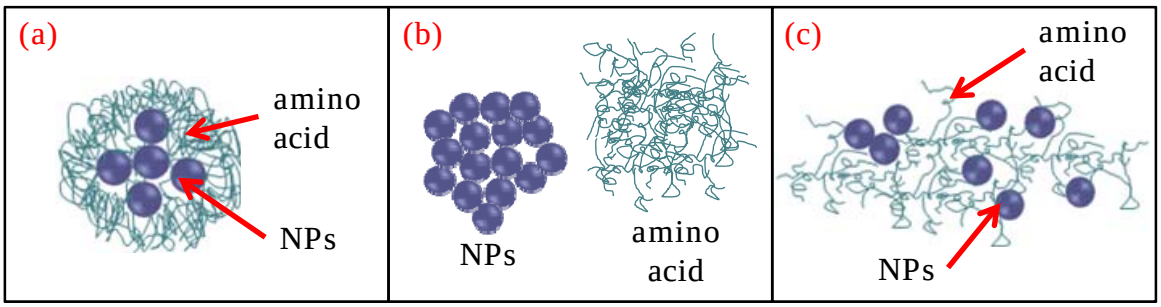


Figure 87 NP/amino acid interaction models (a) Model 1–sphere and (b) Model 2–agglomeration, (c) Model 3 entanglements

The viscosity of Model 1, spherical, is due to the NP/amino acid spheres trying to go past each other allowing the solution to flow. This interaction increases the viscosity because these larger spheres are more difficult to move past each other. This is a behavior that has been observed in nanofluids and cause up to 60 to 80% increase in viscosity even at 0.1% NP solid volumes (66-70, 118, 171). TEM was conducted to verify the NP/amino acid interaction mechanism. The images in Figure 88 are of sample 33%_10NG_L02 whose viscosity is 8.91 $x10^{-4}$ Pa.s (4.4% higher than DI water). The spherical structure is clearly seen with a sphere diameter ranging from 5 to 12µm. Furthermore, the $\Delta S_{solution}$ was -112.5 J/mol.K and the Ω is $7.5x10^{5}$. This solution has among the smallest changes in entropy. With such a small change in entropy (compared to other solutions) the solution is in no hurry to minimize its energy and opts for the most efficient interaction and shape – a sphere.

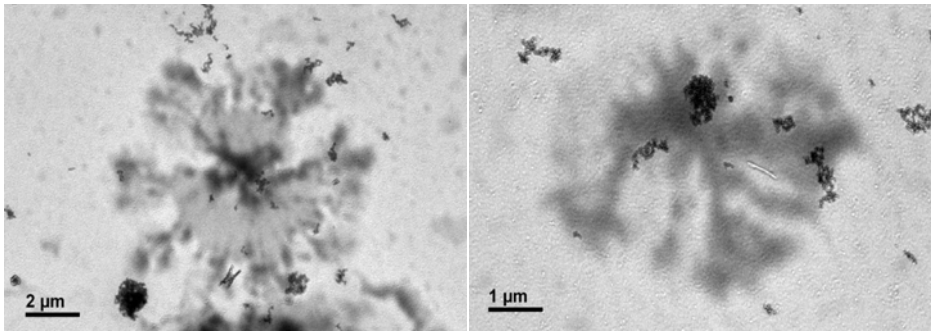


Figure 88 TEM of sample with higher viscosity (model 1) 33%_10NG_L02

For model 2 (agglomerations), the viscosity is expected to decrease significantly. The agglomeration of NPs and excessive amino acid polymerization is expected to leave free ions in the solution. The free ions are due to the surfactant and the amino acid ends. These ions act as structure-breakers, i.e., the water molecules are bound together through hydrogen bonds. The hydrogen bonds are disrupted decreasing the viscosity (184, 185). In Figure 89, the TEM images of sample 33%_10PG_AA04 with viscosity of 7.79 $x10^{-4}$ Pa.s (7.1% lower than DI water) show the extensive amino acid polymerization and minimum to null NP/amino acid interactions. The $\Delta S_{solution}$ for was -2587.1 J/mol.K and the $\Omega$ is $1.38x10^{135}$. The significant change in entropy means the solution has high potential when mixed and it minimizes its energy in the quickest way possible – agglomeration.

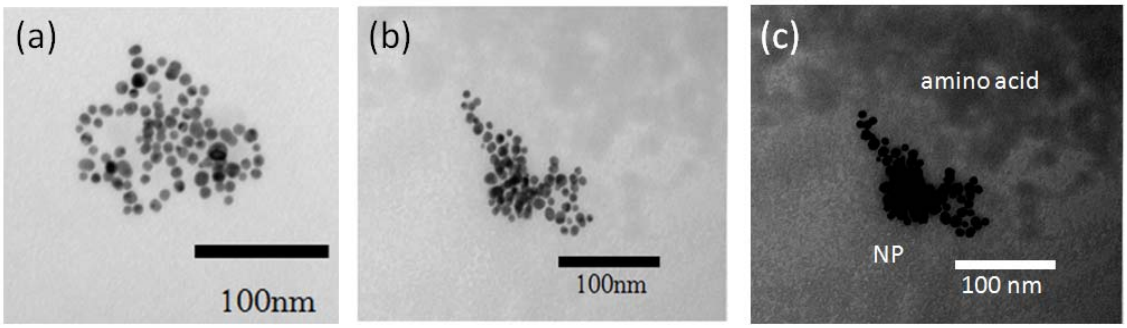


Figure 89 TEM of 33%_10PG_AA04 with 7.1% drop in viscosity. No NP/ acetic acid interactions were found. (c) is the (b) image with contrast adjusted to enhance the amino acid cloud

For Model 3, entanglements, the viscosity is expected to decrease. The polymerized and highly entangled amino acid chains would constrain and "fix" the distribution of the fluid layers with respect to each other. The highly entangled chains would be simply dragged along instead of opposing the fluid layer motion resulting in a drop in viscosity. This is a behavior that has been observed in polymer rheology where the viscosity of the polymer suspension decreases due to chain entanglements (186, 187). Figure 90 shows the TEM image of sample 67%_50PG_GA04 with viscosity of 8.43 $x10^{-4}$ Pa.s (0.7% lower than DI water) shows the amino acid polymerization and entanglements and its interaction with the NPs. The $\Delta S_{solution}$ for was -152.1 J/mol.K and the $\Omega$ is 8.82 $x10^{7}$.

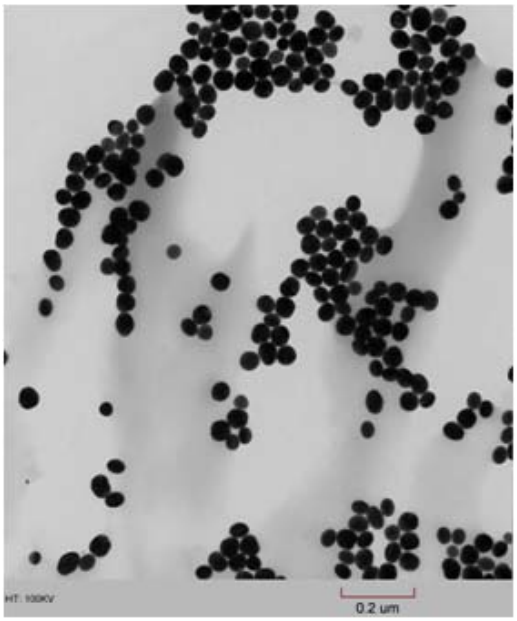


Figure 90 TEM of 67%_50PG_AA02 with a 0.7% drop in viscosity. Amino acid polymerization is evident

## 5.5. The nanoparticle-amino acid interactions

The nanoparticle-amino acid interaction is a poorly understood subject. This research has addressed some of the main factors that have been considered to affect the flow properties of nanofluids: nanoparticle size, nanoparticle concentration, and fluid pH. However, the system gets further complicated when the proteins are included in the solution.

The flow properties of the NP/amino acid solutions do not follow the theories developed for nanofluids. Our results indicate that the flow properties greatly depend on the energy of the system. High decrease in entropy was found for the addition of the smallest nanoparticles (10nm) because these are the ones with highest surface energy (based on the surface–to-volume ratio of the nanoparticle), leading to high total potential

of the system. In addition, if the system has excessive energy the nanoparticles will agglomerate. This is the easiest solution to minimize the energy and reach equilibrium.

We introduced three physical models on the NP/amino acid interaction: spherical, agglomerated and entangled which have been confirmed by TEM. In addition, we have applied a thermodynamic approach to study the energy of the system and identify the potential interaction of the solutions.

The most important finding of this research is that we are able to predict that in our bodies, the nanoparticles will interact with the proteins resulting in the change of protein shapes and properties. The method of particle evaluation presented here is simple yet provides great insights into the NP/amino acid interaction and flow behavior.

# CHAPTER VI

## *IN VIVO* INTERACTION OF NANOPARTICLES AND THE CENTRAL NERVOUS SYSTEM*

This chapter discusses the interactions between nanoparticles and biological systems. Nanomedicine can reach places that traditional medicine cannot such as the central nervous system (CNS). In this study, the CNS of the *Blaberus discoidalis*, a neotropical cockroach is used as the model system. The main focus is to study the interactions of negatively charged gold nanoparticles (NGs) with the cockroaches CNS *in vivo*. The authors refer to the nervous system as the brain and the nerve cord as described in the American Cockroach by Bell (125). Negatively charged spherical nanoparticles with 50nm diameter were used. The negative charge was selected to enhance nanoparticle interaction with the nervous system during signal transfer i.e. during a nerve impulse. The interaction is first monitored with the insect's activity (quantifying locomotion) and the extracted insect's CNS is then used to analyze the physical interactions with the biological system (188).

---

* Part of the information reported in this chapter is reprinted with permission from "*In vivo* observation of gold nanoparticles in the central nervous system of *Blaberus discoidalis*" A. Rocha, Y. Zhou, S. Kundu, J.M. Gonzalez, S.B. Vinson, H. Liang, 2011. *Journal of Nanobiotechnology*, 9 (1):5-13, Copyright 2011 by BioMed Central.

### 6.1. The cockroach as a CNS study model

The use of nanoparticles in biological systems is a subject that has been under scrutiny for some time. The use of nanoparticles for imaging and drug delivery has been extensively studied in mice. Hainfeld and colleagues have used gold nanoparticles to enhance radiotherapy in mice and as a contrast agent for X-ray imaging (20, 21). Metallic nanoparticles, gold in particular, for drug delivery and imaging is a promising field. Gold is one of the main materials selected for this type of application due to their great stability, biocompatibility (189), ease of manufacture (94), and their outstanding imaging capability due to their fluorescence (62, 190). Functionalized gold nanoparticles have also been used to investigate targeted drug delivery (56, 191, 192). However, these *in vivo* methods have not been applied for simpler and inexpensive biological systems like insects.

### 6.2. Cockroach activity after treatment

The cockroach activity was recorded by measuring the total distance walked by each group daily. Two-minute video recordings were performed at the beginning of the light cycle (at 8:00am) for two months. Only six weeks of insect activity are reported because no change in activity was observed after day 17. The motion of each cockroach was traced with Image Tool and the distance walked was calculated by comparing with a fixed reference of known size in the container. The results of cockroach activity are summarized in Figure 91. The days not shown in the summary are due to video recording device failure or due to corrupt video files. After two months, 7 cockroaches from the control and 6 cockroaches from the treated group were alive, giving 78% and 67% survival rates respectively. The activity recording was stopped at two months and two

cockroaches from the NGs treated group and two from the control group were sacrificed and dissected. The remaining cockroaches from each group were sacrificed by freezing at -80$^{o}$C.

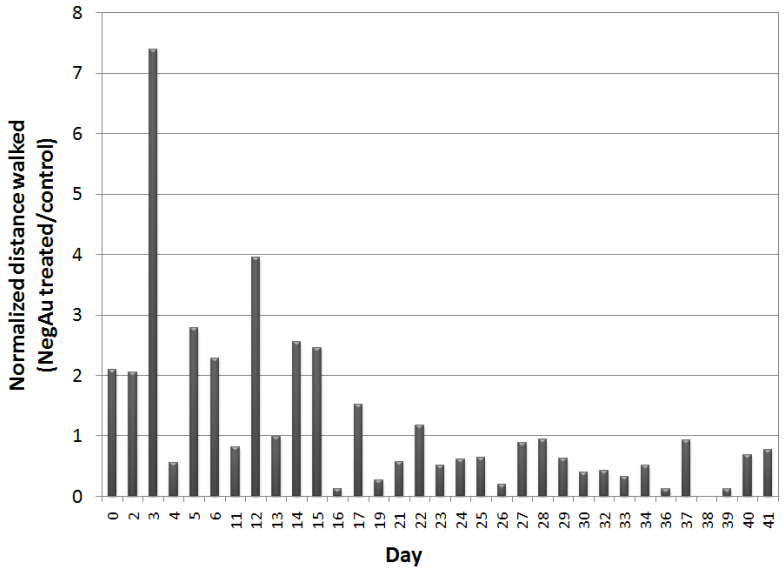


Figure 91 Normalized (NGs treated/untreated) activity

There are several possible factors affecting insects' activity. Reproductive cycle, age, temperature, humidity, wind, noise, vibration, and changes in weather are just a few examples (125). The variation due to the reproductive cycle and age was eliminated by using only young males in this study. The effects of temperature, humidity, and wind were diminished by maintaining them in a controlled environment. However, the fluctuations in noise, vibration and changes in weather affect the activity of both groups. The effects of these variables are diminished by presenting the activity ratio of the treated to the untreated group. Although the treated/untreated ratio still shows variations (days 4, 11, and 13 in particular), Figure 91 indicates an increased activity for the NGs treated

group for 17 days following treatment. After 17 days, their activity falls below that of the control group. The activity monitoring was terminated at 2 months since no significant differences in the cockroaches' behavior after day 17 were observed.

### 6.3. Characterizing nanoparticle/CNS interactions

To understand the effects of NGs on the insects' behavior, a series of characterization experiments were conducted to identify. Spectroscopic and morphologic analyses were conducted using hyperspectral imaging, XPS, Confocal microscopy, and TEM, as described in Chapter III. Using these tools, the location and interactions of the NGs with the cockroach's CNS were identified.

#### 6.3.1. Spectroscopic analysis

The hyperspectral imaging system from CitoViva was utilized to trace the NG nanoparticle distribution in the treated roach. The NGs treated tissue was then scanned and the spectral imaging was compared to that of the library. From the scanned tissues, only the spectra recorded from the brain and nerve cord matched to that of the library generated from the NGs/DI water solution as introduced in Chapter III. The results are shown in the Figure 92. The image on the left is the hyperspectral results. The image on the right is the optical image of the scanned cockroach brain.

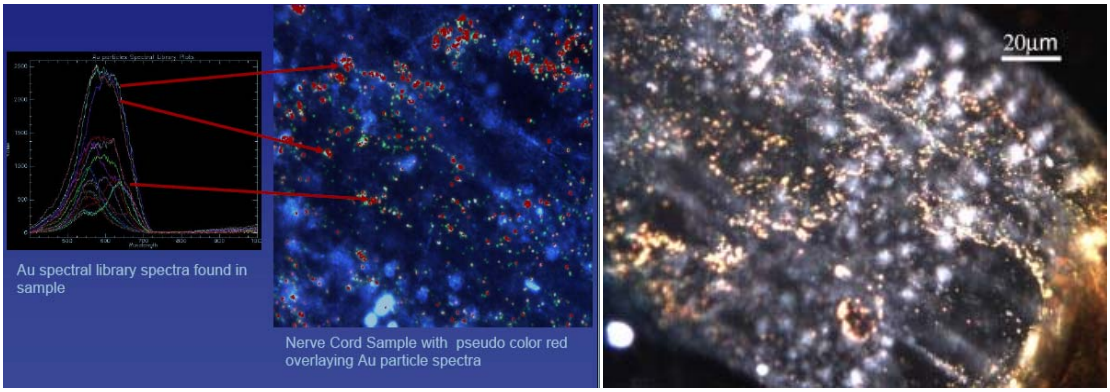


Figure 92 The hyperspectral scan from extracted cockroach brains. The bright red spots (left) are nanoparticles

The XPS system was used to verify the presence of gold nanoparticles inside the brain. Figure 93a shows the results for the control sample (untreated) and Figure 93b for the NGs treated brain which shows the binding energy for gold at 85 eV. The high signal-to-noise ratio of the XPS scans was caused by too few particles on the scanned surface. The XPS could only scan to a few nanometers (<10nm) deep from the surface. This limited the number of NGs present in the scanned region since only a few nanoparticles were exposed within 10nm from the surface. However, the difference between the control and the NGs treated samples were seen around 85 eV. The curve fitting obtained for Figure 93b was obtained by averaging of 21 consecutive intensity readings (10 above and 10 below) for each binding energy value recorded. This allows for a moving average and smoothing of the fitted curve. The XPS results indicated that the gold nanoparticles were dispersed inside the insect's brain.

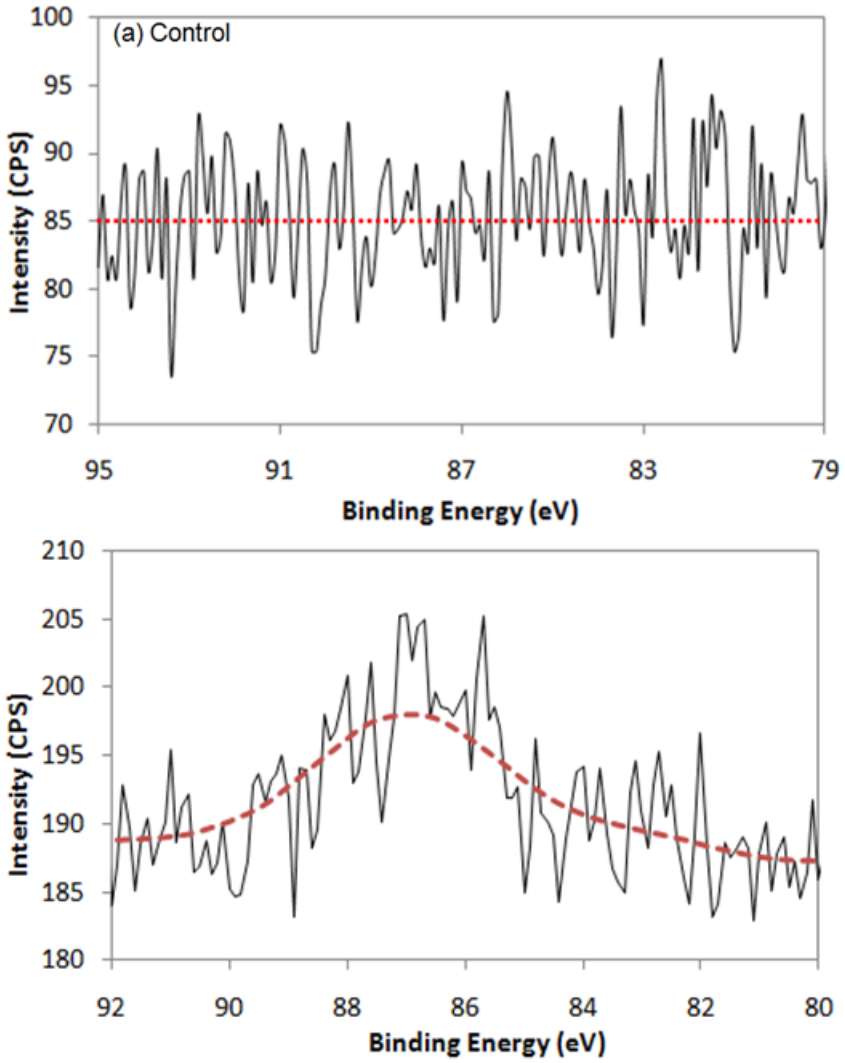


Figure 93 Gold has a bonding energy of 85eV. (uppper) XPS results for control cockroach brain. (lower) XPS results for NGs treated cockroach brain

### 6.3.2. Morphological analysis

Confocal microscopy was employed. In the transmission images, Figure 94a and 94b, exhibited visible differences in the tissues of the NGs treated and untreated brains respectively. The darker regions were an indication of nanoparticle dispersion within the tissue. The electron transmission microscopic image showed a clear difference between

the treated and untreated cockroach brains. The NGs treated brain had an abnormal tissue (dark) due to the embedded nanoparticles. This further proved the existence NGs inside the cockroach's brain. Figure 94c and 94d show the fluorescence of the treated and untreated brains respectively. The main challenge of the fluorescent images was the self fluorescence of the cockroach brain tissues. The self fluorescence was absorbed and emitted at a wavelength close to the gold nanoparticles. However, the results clearly showed the NGs treated brain had stronger fluorescence intensity than the control. The horizontal yellow line on the top images of Figures 94c and 94d showed the location of the intensity profile below. These locations were selected because they exhibit the highest intensity. The fluorescence of the treated brain was significantly higher than the untreated. The intensity difference was further enhanced because the laser power was set at 30% for the treated brain and 50% for the untreated brain, i.e. the fluorescent signal recorded for the untreated brain was partially due to the higher laser power and the self fluorescence of the tissue.

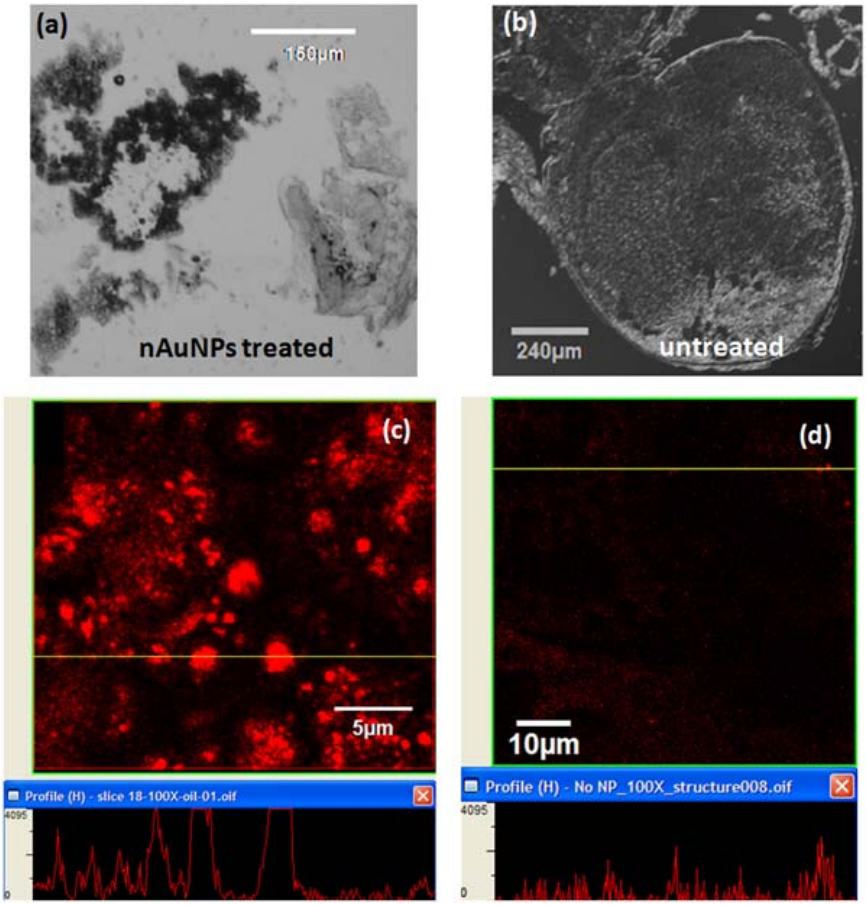


Figure 94 Transmission light image of (a) NGs treated dissected cockroach brain and (b) control. Darker tissue is a sign of nanoparticles. A clear difference can be observed in the treated tissue (a) while the untreated (b) shows no difference in the tissue. Fluorescent image of (c) NGs trated and (d) untreated samples. The lower window shows the fluorescent intensity at the location of the yellow line on the upper windows

### 6.3.3. Nanoscopic analysis

Upon closer inspection of the treated brain tissue, there was evidence of nanoparticle encapsulation. Figure 95a showed well-defined 2-5µm (2000 to 5000 nm) diameter spheres. Upon inspection of the fluorescent image of this view, Figure 95b, hundreds of small nanoparticles were found dispersed or agglomerated (indicated with green arrows) inside these spheres. Figure 95c, an overlay of the transmission (95a) and

fluorescent (95b) images further proved the agglomeration of nanoparticles inside the spherical structures.

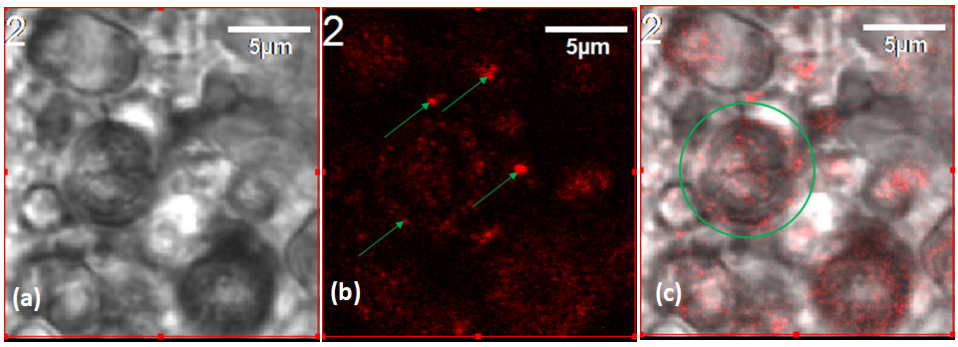


Figure 95 (a) Transmission, (b) fluorescent, and (c) overly image of NGs treated brain. Particle encapsulation is evident. The arrows in (b) indicate particle agglomerations

The NP morphology in the cockroaches' brain was characterized with a JEOL-JEM 2010 TEM. Figure 96 showed NGs (in dark) surrounded by light colored spheres, i.e., the nanoparticles were encapsulated. The spheres in Figure 96 ranged from 200 to 500 nm in diameter.

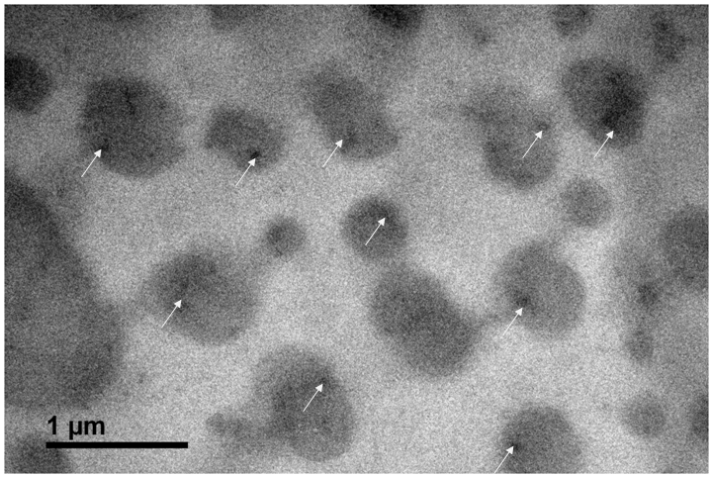


Figure 96 TEM image of NGs treated brain confirms nanoparticle encapsulation by the brain tissue. The arrows indicate the nanoparticle inside the protein capsule

This value disagreed with by one order of magnitude to that observed in Figure 95. In Figure 96, we observed a single nanoparticle embedded in a sphere of 200-500 nm in diameter while Figure 95 shows an agglomeration of these smaller spheres into larger ones of approximately 2-5 μm in diameter. This indicates a multi-level self-arrangement of embedded nanoparticles. Based on our findings presented in Chapter V and on studies by Cedervall et al. (193) and Lundqvist and colleagues (194), it is known that the nanoparticles will interact with the proteins present in the biological system, i.e. the material surrounding the nanoparticles are proteins present in the nervous system of the cockroach.

### 6.4. Nanoparticle interaction with CNS

The results of characterization have repeatedly proven that the NGs were encapsulated. How did this process occur? There are two possible reasons, (1) a defense mechanism of the immune system of the cockroach against a foreign object, or (2) as a protein corona that surrounds the nanoparticles due to its negative surface charge. In terms of defense mechanisms, when a foreign object enters the biological system, the response of the immune system is to block further damage by encapsulating the object. This response has been readily found and studied in insects (74, 87), the immune system surrounds the foreign object by phagocytes to then be digested and/or destroyed. Some parasites avoid encapsulation due to an ionic surface. When these parasites were rinsed to remove the ions from the surface, encapsulation occurred (195). Once encapsulated, the foreign objects were expected to either reduce in size or change morphologically. In the present research, the nanoparticles are small enough (50nm) to be encapsulated by

phagocytosis. Through this process the immune system will excrete the nanoparticle from the cell. It is evidenced in Figure 93b that the NGs nanoparticles remain inside the brain after 2 months of injection. In the present research, we only observed nanoparticle encapsulation with no visible changes in particle size or morphology, as shown in Figure 96. It is seen that particles are well defined spheres of approximately 50nm diameter.

It has been reported that a protein corona is the encapsulation of charged particles by the polar amino acids in proteins (87, 193, 196). When the charged nanoparticles come in contact with live tissue, the proteins or amino acids of opposite charge will be attracted to the surface of the particle. This immediate attraction might affect the normal behavior of other proteins whose function or processes depended on the protein now in contact with the nanoparticle. This chain reaction may continue until equilibrium is reached. According to our results of roaches' behavior, the NGs treated roaches had a sudden increase in their activity during 17 days after treatment, followed by a decrease in their activity for the remaining of the observation period. This could be attributed to the affected signal transfer in the nervous system. Similar change in behavior based on ion transfer was reported Hoyle (197) and Luo et al. (198). This correlation of activity caused by the NGs on the CNS of the insect are attributed to how the brain of the cockroach controls its muscle response and locomotion (77). Although proteins do not break into ions, introducing charged particles into the nervous system causes an imbalance in the signal transmission that links to the insect's locomotion.

# CHAPTER VII

# CONCLUSIONS AND FUTURE RECOMMENDATIONS

This research investigated mechanisms of interfacial interactions between biological and synthetic materials at the bulk and nano scales. A novel method using rotational flow to quantify the material-biomolecule interactions was utilized. The adhesion of biomolecules to the bulk materials was measured with a rotational shear flow. Experimental and thermodynamic analyses were carried on four nanoparticle/amino acid solutions. A physical model based on entropy change was proposed to predict the behavior of nanoparticles inside a biological system. Below are the highlights of major results and discoveries in each study.

## 7.1. Interactions at the bulk scale

A parallel plate rotational flow was used to quantify the cell and protein adhesion to bulk materials. The results showed clear evidence that the synthetic materials' chemistry is the most influential factor in biomolecule adhesion. The fibroblast adhesion to PMMA was four times higher than to PC due to the highly polarized PMMA structure. The egg-white protein adhesion was 10 times higher to Si than Ti due to the higher electronegativity of Si. The adhesion of 12-day old chick embryo neurons on poly-D-lysine coated glass reached a maximum of 3.0 Pa. This plateau indicates a limit to cell strengthening.

Quantifying protein/cell adhesion to a substrate is one of the first steps in identifying the most suitable materials for every biological application. For a permanent, long term-implant, a strong protein/cell adhesion is essential in implant incorporation. It will also allow researchers to understand how variations in processing, coatings, or other substrate properties affect adhesion.

The main conclusions from this work are that protein or cell adhesion to a surface can be quantified and compared for many different biomolecules (fibroblasts, neurons, or proteins) to various substrates (polymers, glass, and metallic coatings). Also, material chemistry is the most influential factor affecting adhesion. The results obtained demonstrate the methodology developed provide repeatable and accurate results.

### 7.2. Interactions at the nano scale

A cone and plate geometry was used to measure the viscosity of NP/protein and NP/amino acid solutions. The selected NPs were positively and negatively charged spherical gold with 10, 20, and 50nm diameter. The protein solution used in this study was bovine serum, which is rich in albumin. The amino acids were selected based on the albumin chemistry, whose structure is rich in L-lysine, L-arginine, L-glutamic acid, and L-aspartic acid. The viscosity of the NP/protein solutions showed a linear dependence to %vol of NP solution due mainly to protein dilution.

The viscosity of the NP/amino acid solutions was measured and used to calculate its potential (change in entropy i.e. $\Delta S_{solution}$) and the possible number of NP/biomolecule arrangements ($\Omega$). Based on the results, three NP/amino acid interaction models were presented: spherical, agglomerated, and entangled.

The spherical model has the lowest calculated $\Delta S_{solution}$ and the lowest $\Omega$. In this model, agglomerated nanoparticles at the core are surrounded by amino acid molecules. The viscosity of the solutions increases. The agglomerated model is presented for solutions with high $\Delta S_{solution}$ and high $\Omega$. The nanoparticles in these solutions agglomerate while the amino acid molecules polymerize with minimum to null NP/amino acid interactions. The viscosity of these solutions decreases. The entangled model is expected for solutions with moderate $\Delta S_{solution}$ and moderate $\Omega$. The amino acid entanglements are expected to cause a slight drop in viscosity. Some nanoparticle/amino acid interactions are expected.

Overall, the NP/protein and NP/amino acid analysis presented here will help predict and identify how the nanoparticles, when used for medical applications, will interact and affect the body. This analysis is based on how the nanoparticles affect the energy balance of the protein or amino acid solution.

The first conclusion from this work is that there are nanoparticle/nanoparticle, amino acid/amino acid, and amino acid/nanoparticle interactions. The second conclusion is that the viscosity of the amino acid/nanoparicle solutions depends on the amino acid conformation and how this is affected by the potential energy the nanoparticles bring into the solution when mixed.

### 7.3. NP effect on CNS, an *in vivo* study

Once the NP/amino acid behavior was understood, the negatively charged, 50nm, gold NPs were used to observe their interaction with the central nervous system (CNS) of the cockroach *in vivo*. This study showed that the NPs form a multi-level encapsulation by

the proteins present in the CNS. Based on the changes in insect activity, we estimate that the encapsulation process took approximately 17 days. The insect's behavior was altered because the negatively charged NPs affected the positively charged communication channels ($Ca^{+}$ and $K^{+}$) of the CNS.

The first conclusion is that the cockroach is an appropriate subject to observe how surface charged nanoparticles affect the CNS. The second is that charged nanoparticles interact with the proteins present in the CNS and these interactions affect the signal transfer in the insect and this change can be monitored by the insects' locomotion.

Ultimately, all methods presented here will help design and identify materials that better fit our needs: enhance adhesion with cells and ensure a long-lasting implant, functionalize nanoparticles to avoid or better control its effects on the body, and to use a simple system to study the effects of NPs on the nervous system.

### 7.4. Future recommendations

- Investigate the effect of surface and materials treatment (UV exposure or other sterilizing techniques) on the cell adhesion to bulk materials.
- Study the effects of NP materials, NP shape, and change in temperature on the viscosity and thermodynamic equilibrium of NP/amino solutions.

## REFERENCES


1. Ratner BD, Hoffman AS, Schoen FJ, Lemons JE (2004) *Biomaterials Science - An Introduction to Materials in Medicine* (2nd edition) (Elsevier, Cambridge, MA).

2. Ratner BD, Bryant SJ (2004) Biomaterials: Where we have been and where we are going. *Annu Rev Biomed Eng* 6:41-76.

3. Long M, Rack HJ (1998) Titanium alloys in total joint replacement--a materials science perspective. *Biomaterials* 19(18):1621-1639.

4. Matsuno H, Yokoyama A, Watari F, Uo M, Kawasaki T (2001) Biocompatibility and osteogenesis of refractory metal implants, titanium, hafnium, niobium, tantalum and rhenium. *Biomaterials* 22(11):1253-1262.

5. Castleman LS, Motzkin SM, Alicandri FP, Bonawit VL, Johnson AA (1976) Biocompatibility of nitinol alloy as an implant material. *J Biomed Mater Res* 10(5):695-731.

6. Dee KC, Puleo DA, Bizios R (2002) *An Introduction to Tissue-Biomaterial Interactions* (John Wiley & Sons, Hoboken, New Jersey).

7. Mathur AB, Collier TO, Kao WJ, Wiggins M, Schubert MA*, et al.* (1997) *In vivo* biocompatibility and biostability of modified polyurethanes. *J Biomed Mater Res* 36(2):246-257.

8. Smeby LC, Widerøe TE, Balstad T, Jørstad S (1986) Biocompatibility aspects of cellophane, cellulose acetate, polyacrylonitrile, polysulfone and polycarbonate hemodialyzers. *Blood Purificat* 4(1-3):93-101.

9. Santavirta S, Nordstrom D, Metsarinne K, Kontinnen YT (1993) Biocompatibility of polyethylene and host response to loosening of cementless total hip replacement. *Clin Orthop Relat Res* 297:100-110.

10. Jansen JA, Wolke JGC, Swann S, Van Der Waerden JPCM, De Groof K (1993) Application of magnetron sputtering for producing ceramic coatings on implant materials. *Clin Oral Implan Res* 4(1):28-34.

11. Shchukin DG, Sukhorukov GB, Möhwald H (2003) Biomimetic fabrication of nanoengineered hydroxyapatite/polyelectrolyte composite shell. *Chem Mater* 15(20):3947-3950.

12. Neto MA, Silva EL, Fernandes AJS, Oliveira FJ, Silva RF (2009) Interfacing metallic ohmic contacts in biocompatible ceramic substrates with diamond surfaces for biosensing applications. *World Congress on Medical Physics and*

*Biomedical Engineering, September 7 - 12, 2009,* Munich, Germany*,* IFMBE Proceedings, eds Dössel O, Schlegel WC (Springer Berlin), Vol 25/8, pp 336-338.

13. Salehi R, Arami M, Mahmoodi NM, Bahrami H, Khorramfar S (2010) Novel biocompatible composite (chitosan-zinc oxide nanoparticle): Preparation, characterization and dye adsorption properties. *Colloid Surface B: Biointerface* 80(1):86-93.

14. Park S, Mohanty N, Suk JW, Nagaraja A, An J*, et al.* (2010) Biocompatible, robust free-standing paper composed of a tween/graphene composite. *Adv Mater* 22(15):1736-1740.

15. Nath S, Tripathi R, Basu B (2009) Understanding phase stability, microstructure development and biocompatibility in calcium phosphate-titania composites, synthesized from hydroxyapatite and titanium powder mix. *Mater Sci Eng: C* 29(1):97-107.

16. Salata O (2004) Applications of nanoparticles in biology and medicine. *J Nanobiotechnol* 2(1):1-6.

17. Kubik T, Bogunia-Kubik K, Sugisaka M (2005) Nanotechnology on duty in medical applications. *Curr Pharm Biotechno* 6:17-33.

18. Alexiou C, Jurgons R, Seliger C, Iro H (2006) Medical applications of magnetic nanoparticles. *J Nanosci Nanotechnol* 6:2762-2768.

19. Aubin-Tam ME, Hamad-Schifferli K (2008) Structure and function of nanoparticle–protein conjugates. *Biomed Mater* 3(3):034001.

20. Hainfeld JF, Slatkin DN, Smilowitz HM (2004) The use of gold nanoparticles to enhance radiotherapy in mice. *Phys Med Biol* 49(18):309-315.

21. Hainfeld JF, Slatkin DN, Focella TM, Smilowitz HM (2006) Gold nanoparticles: A new x-ray contrast agent. *Br J Radiol* 79(939):248-253.

22. Bokhari MA, Akay G, Zhang S, Birch MA (2005) The enhancement of osteoblast growth and differentiation *in vitro* on a peptide hydrogel--polyhipe polymer hybrid material. *Biomaterials* 26(25):5198-5208.

23. Mistry AS, Mikos AG (2005) Tissue engineering strategies for bone regeneration. *Regenerative Medicine II,* Advances in biochemical engineering/biotechnology, ed Yannas IV (Springer Berlin), Vol 94, pp 129-129.

24. Yu LMY, Leipzig ND, Shoichet MS (2008) Promoting neuron adhesion and growth. *Mater Today* 11(5):36-43.

25. Pan J, Leygraf C, Thierry D, Ektessabi AM (1997) Corrosion resistance for biomaterial applications of $TiO_2$ films deposited on titanium and stainless steel by ion-beam-assisted sputtering. *J Biomed Mater Res* 35(3):309-318.

26. Witte F, Fischer J, Nellesen J, Crostack H-A, Kaese V*, et al.* (2006) *In vitro* and *in vivo* corrosion measurements of magnesium alloys. *Biomaterials* 27(7):1013-1018.

27. Khan MA, Williams RL, Williams DF (1996) *In vitro* corrosion and wear of titanium alloys in the biological environment. *Biomaterials* 17(22):2117-2126.

28. Karageorgiou V, Kaplan D (2005) Porosity of 3D biomaterial scaffolds and osteogenesis. *Biomaterials* 26(27):5474-5491.

29. Wang Y, Kim H-J, Vunjak-Novakovic G, Kaplan DL (2006) Stem cell-based tissue engineering with silk biomaterials. *Biomaterials* 27(36):6064-6082.

30. Harrison BS, Atala A (2007) Carbon nanotube applications for tissue engineering. *Biomaterials* 28(2):344-353.

31. Anderson AA (2005) A hybrid mathematical model of solid tumour invasion: The importance of cell adhesion. *Math Med Biol* 22:163–186.

32. Curtis ASG, Lackie JM (1991) *Measuring Cell Adhesion* (John Wiley & Sons, New York).

33. Garcia AJ, Ducheyne P, Boettiger D (1997) Quantification of cell adhesion using a spinning disc device and application to surface-reactive materials. *Biomaterials* 18(16):1091-1098.

34. Hu L, Zhang X, Miller P (2006) Cell adhesion measurement by laser-induced stress waves. *J Appl Phys* 100(8):84701-84705.

35. Kirkpatrick CJ, Bittinger F, MWagner, Kohler H, Kooten TG*, et al.* (1998) Current trends in biocompatibility testing. *Proc Inst Mech Eng* 212(H):75-84.

36. Martines E, McGhee K, Wilkinson C, Curtis A (2004) A parallel-plate flow chamber to study initial cell adhesion on a nanofeatured surface. *IEEE Trans on Nanobiosci* 3(2):90-96.

37. Pizzoferrato A, Ciapetti G, Stea S, Cenni E, Arciola CR*, et al.* (1994) Cell culture methods for testing biocompatibility. *Clin Mater* 15(3):173-190.

38. Shi B, Liang H (2001) Tribological applications of biomaterials: An overview. *Sci China Ser A* 44: 297-306.

39. Rocha A, Hahn M, Liang H (2010) Critical fluid shear stress analysis for cell–polymer adhesion. *J Mater Sci* 45(3):811-817.

40. Rocha A, Jian K, Ko G, Liang H (2010) Neuron adhesion and strengthening. *J Appl Phys* 108(2):024702.

41. Hallab NJ, Bundy KJ, O'Connor K, Moses RL, Jacobs JJ (2001) Evaluation of metallic and polymeric biomaterial surface energy and surface roughness characteristics for directed cell adhesion. *Tissue Eng* 7:55-71.

42. Bongrand P, Claesson PM, Curtis ASG (1994) *Studying Cell Adhesion* (Springer - Verlag Berlin).

43. Bundy KJ, Harris LG, Rahn BA, Richards RG (2001) Measurement of fibroblast and bacterial detachment from biomaterials using jet impingement. *Cell Biol Int* 25(4):289–307.

44. Channavajjala LS, Eidsath A, Saxinger WC (1997) A simple method for measurement of cell-substrate attachment forces:Application to HIV-1 TAT. *J Cell Sci* 110:249-256.

45. Lu H, Koo LY, Wang WM, Lauffenburger DA, Griffith LG*, et al.* (2004) Microfluidic shear devices for quantitative analysis of cell adhesion. *Anal Chem* 75:5257-5264.

46. Brown TD (2000) Techniques for mechanical stimulation of cells *in vitro*: A review. *J Biomech* 33:3-14.

47. Buschmann MH, Dieterich P, Adams NA, Schnittler HJ (2005) Analysis of flow in a cone-and-plate apparatus with respect to spatial and temporal effects on endothelial cells. *Biotechnol Bioeng* 89(5):493-502.

48. Blackman BR, Barbee KA, Thibault LE (2000) *In vitro* cell shearing device to investigate the dynamic response of cells in a controlled hydrodynamic environment. *Ann Biomed Eng* 28:363–372.

49. Malek AM, Ahlquist R, Gibbons GH, Dzau VJ, Izumo S (1995) A cone-plate apparatus for the *in vitro* biochemical and molecular analysis of the effect of shear stress on adherent cells. *Method Cell Sci* 17:165-176.

50. Schnittler H-J, Franke RP, Akbay U, Mrowietz C, Drenckhahn D (1993) Improved *in vitro* rheological system for studying the effect of fluid shear stress on cultured cells. *Am J Physiol* 256:C289-C298.

51. Reutelingsperger CPM, Gool RGJV, Heijnen V, Frederik P, Lindhout T (1994) The rotating disc as a device to study the adhesive properties of endothelial cells under differential shear stresses. *J Mater Sci: Mater Med* 5:361-367.

52. Orsello CE, Lauffenburger DA, Hammer DA (2001) Molecular properties in cell adhesion: A physical and engineering perspective. *Trends Biotechnol* 19(8):310-316.

53. Young BR, Pitt WG, Cooper SL (1988) Protein adsorption on polymeric biomaterials I. Adsorption isotherms. *J Colloid Interf Sci* 124(1):28-43.

54. Lu DR, Park K (1991) Protein adsorption on polymer surfaces: Calculation of adsorption energies. *J Biomater Sci Polym Ed* 2(4):317-322.

55. Norde W, Lyklema J (1978) The adsorption of human plasma albumin and bovine pancreas ribonuclease at negatively charged polystyrene surfaces : I. Adsorption isotherms. Effects of charge, ionic strength, and temperature. *J Colloid Interf Sci* 66(2):257-265.

56. Paciotti GF, Myer L, Weinreich D, Goia D, Pavel N*, et al.* (2004) Colloidal gold: A novel nanoparticle vector for tumor directed drug delivery. *Drug Deliv* 11(3):169-183.

57. Han G, Ghosh P, Rotello VM (2007) Functionalized gold nanoparticles for drug delivery. *Nanomedicine* 2(1):113-123.

58. Cheng J, Teply BA, Sherifi I, Sung J, Luther G*, et al.* (2007) Formulation of functionalized PLGA-PEG nanoparticles for *in vivo* targeted drug delivery. *Biomaterials* 28(5):869-876.

59. Cedervall T, Lynch I, Lindman S, Berggård T, Thulin E*, et al.* (2007) Understanding the nanoparticle–protein corona using methods to quantify exchange rates and affinities of proteins for nanoparticles. *Proc Natl Acad Sci USA* 104(7):2050-2055.

60. Lynch I, Elder A (2009) Disposition of nanoparticles as a function of their interactions with biomolecules *Nanomaterials: Risks and Benefits,* NATO science for peace and security series c: Environmental security, eds Linkov I, Steevens J (Springer, Netherlands), pp 31-41.

61. Lynch I, Dawson KA (2008) Protein-nanoparticle interactions. *Nano Today* 3(1-2):40-47.

62. Ghosh P, Han G, De M, Kim CK, Rotello VM (2008) Gold nanoparticles in delivery applications. *Adv Drug Deliver Rev* 60(11):1307-1315.

63. Cheng Y, C. Samia A, Meyers JD, Panagopoulos I, Fei B*, et al.* (2008) Highly efficient drug delivery with gold nanoparticle vectors for *in vivo* photodynamic therapy of cancer. *J Am Chem S* 130(32):10643-10647.

64. Chithrani BD, Chan WCW (2007) Elucidating the mechanism of cellular uptake and removal of protein-coated gold nanoparticles of different sizes and shapes. *Nano Lett* 7(6):1542-1550.

65. Morawski AM, Winter PM, Crowder KC, Caruthers SD, Fuhrhop RW*, et al.* (2004) Targeted nanoparticles for quantitative imaging of sparse molecular epitopes with mri. *Magnet Reson Med* 51(3):480-486.

66. Pozhar LA (2000) Structure and dynamics of nanofluids: Theory and simulations to calculate viscosity. *Phys Rev E* 61(2):1432.

67. Prasher R, Song D, Wang J, Phelan P (2006) Measurements of nanofluid viscosity and its implications for thermal applications. *Appl Phys Lett* 89(13):133108.

68. Murshed SMS, Leong KC, Yang C (2008) Investigations of thermal conductivity and viscosity of nanofluids. *Int J Therm Sci* 47(5):560-568.

69. Koo J, Kleinstreuer C (2005) Laminar nanofluid flow in microheat-sinks. *Int J Heat Mass Transfer* 48(13):2652-2661.

70. Routbort J, Singh D, Timofeeva E, Yu W, France D (2011) Pumping power of nanofluids in a flowing system. *J Nanopart Res* 13(3):931-937.

71. Wang J, Yan Z, Zhang H, Lu J (2000) Effect of temperature on viscosity properties of some [alpha]-amino acids in aqueous urea solutions. *Biophys Chem* 86(1):71-78.

72. Aubin-Tam M-E, Hamad-Schifferli K (2005) Gold nanoparticle−cytochrome c complexes: The effect of nanoparticle ligand charge on protein structure. *Langmuir* 21(26):12080-12084.

73. Provenzale JM, Silva GA (2009) Uses of nanoparticles for central nervous system imaging and therapy. *Am J Neuroradiol* 30(7):1293-1301.

74. Begley DJ (2004) Delivery of therapeutic agents to the central nervous system: The problems and the possibilities. *Pharmacol Therapeut* 104(1):29-45.

75. Huber I, Masler EP, Rao BR (1990) *Cockroaches as Models for Neurobiology: Applications in Biomedical Research* (CRC Press, Boca Raton, FL).

76. Scharrer B (1987) Insects as models in neuroendocrine research. *Annu Rev Entomol* 32(1):1-16.

77. Makoto M, Ryuichi O, Yongsheng L, Nicholas JS (1998) Mushroom bodies of the cockroach: Activity and identities of neurons recorded in freely moving animals. *J Comparat Neurol* 402(4):501-519.

78. Peterson RT, Nass R, Boyd WA, Freedman JH, Dong K*, et al.* (2008) Use of non-mammalian alternative models for neurotoxicological study. *NeuroToxicology* 29(3):546-555.

79. Eisemann CH, Jorgensen WK, Merritt DJ, Rice MJ, Cribb BW*, et al.* (1984) Do insects feel pain? A biological view. *Cell Mol Life Sci* 40(2):164-167.

80. Manfred E, Jürgen R, Asja N, Heinz P (1992) A new specific antibody reveals octopamine-like immunoreactivity in cockroach ventral nerve cord. *J Comparat Neurol* 322(1):1-15.

81. Colwell CS, Page TL (1990) A circadian rhythm in neural activity can be recorded from the central nervous system of the cockroach. *J Comp Physiol A:* 166(5):643-649.

82. Brown S, Strausfeld N (2009) The effect of age on a visual learning task in the american cockroach. *Learn Memory* 16(3):210-223.

83. Yamamoto A, Mishima S, Maruyama N, Sumita M (2000) Quantitative evaluation of cell attachment to glass, polystyrene, and fibronectin- or collagen-coated polystyrene by measurement of cell adhesive shear force and cell detachment energy. *J Biomed Mater Res* 50:114–124.

84. Alonso s, Lau J, Jaber BL (2008) Biocompatible hemodialysis membranes for acute renal failure (review). in *Cochrane Database of Systematic Reviews* (JohnWiley & Sons, Ltd, Hoboken, NJ), pp 1-38.

85. Li C, He Q, Lin G, Sun X, Tang W*, et al.* (2004) TiN/CrN multileyered coatings with TiCrN interlayer deposited by a filtered cathodic vacuum arc technique. *J Univ Sci Technol Beijing* 11:5.

86. Liu X, Li C, Xu J, Tang W, Lv F (2009) Characteristics of TiN/CrN multilayer coatings with TiCrN and CrTiN interlayer. *Advanced Ceramic Coatings and Interfaces II: Ceramic and Engineering Science Proceedings* (John Wiley & Sons, Inc., Hoboken, NJ) vol. 28, no 3, pp 135-144.

87. Chithrani BD, Ghazani AA, Chan WCW (2006) Determining the size and shape dependence of gold nanoparticle uptake into mammalian cells. *Nano Lett* 6(4):662-668.

88. Medley CD, Smith JE, Tang Z, Wu Y, Bamrungsap S*, et al.* (2008) Gold nanoparticle-based colorimetric assay for the direct detection of cancerous cells. *Anal Chem* 80(4):1067-1072.

89. Jain PK, Huang X, El-Sayed IH, El-Sayed MA (2008) Noble metals on the nanoscale: Optical and photothermal properties and some applications in imaging, sensing, biology, and medicine. *Accounts Chem Res* 41(12):1578-1586.

90. Singh N, Lyon LA (2007) Au nanoparticle templated synthesis of pNIPAm nanogels. *Chem Mater* 19(4):719-726.

91. Zhan Q, Qian J, Li X, He S (2010) A study of mesoporous silica-encapsulated gold nanorods as enhanced light scattering probes for cancer cell imaging *Nanotechnology* 21(5):055704-055704

92. Arvizo R, Bhattacharya R, Mukherjee P (2010) Gold nanoparticles: Opportunities and challenges in nanomedicine. *Expert Opin Drug Del* 7(6):753-763.

93. Turkevich J, Stevenson PC, Hillier J (1951) A study of the nucleation and growth processes in the synthesis of colloidal gold. *Discuss Faraday Soc* 11:55-75.

94. Kundu S, Peng LH, Liang H (2008) A new route to obtain high-yield multiple-shaped gold nanoparticles in aqueous solution using microwave irradiation. *Inorg Chem* 47(14):6344-6352.

95. Kundu S, Maheshwari VC, Niu S, Saraf R (2008) Polyelectrolyte mediated scalable synthesis of highly stable silver nanocubes in less than a minute using microwave irradiation. (DigitalCommons@University of Nebraska - Lincoln).

96. Curry S, Mandelkow H, Brick P, Franks N (1998) Crystal structure of human serum albumin complexed with fatty acid reveals an asymmetric distribution of binding sites. *Nat Struct Mol Biol* 5(9):827-835.

97. Govorukhina NI, Keizer-Gunnink A, van der Zee AGJ, de Jong S, de Bruijn HWA*, et al.* (2003) Sample preparation of human serum for the analysis of tumor markers: Comparison of different approaches for albumin and [gamma]-globulin depletion. *J Chromatogr A* 1009(1-2):171-178.

98. Steel LF, Trotter MG, Nakajima PB, Mattu TS, Gonye G*, et al.* (2003) Efficient and specific removal of albumin from human serum samples. *Mol Cell Proteomics* 2(4):262-270.

99. HyClone Laboratories Inc (2007) Assay of bovine calf serum. HyClone Laboratories Inc Logan, UT.

100. Alberts B, Bray D, Lewis J, Raff M, Roberts K*, et al.* (1994) *Molecular Biology of the Cell 3rd Ed.* (Garland Publishing, New York).

101. Pollard TD, Earnshaw WC (2002) *Cell Biology* (Saunders, Philadelphia, PA).

102. Baxi J (2008) Tribological characterization of coatings and nanofluids. Master of Science Texas A&M University, College Station.

103. Feng F (2010) Effects of surface properties on adhesion of protein to biomaterials. Master of Science Texas A&M University College Station.

104. LaPlaca MC, Thibault LE (1997) An *in vitro* traumatic injury model to examine the response of neurons to a hydrodynamically-induced deformation. *Ann Biomed Eng* 25:665-677.

105. Ono O, Ando J, Kamiya A, Kuboki Y, Yasuda H (1991) Flow effects on cultured vascular endothelial and smooth muscle cell functions. *Cell Struct Funct* 16:365-374.

106. Macosko CW (1994) *Rheology Principles, Measurements, and Applications* (Wiley VCH, New York).

107. Oztekin A, Brown RA (1993) Instability of a viscoelastic fluid between rotating parallel disks: Analysis for the oldroyd-b fluid. *J Fluid Mech* 255:473-502.

108. Lygren M, Andersson HI (2001) Turbulent flow between a rotating and a stationary disk. *J Fluid Mech* 426:297-326.

109. Schouveiler L, Gal PL, Chauve MP (2001) Instabilities of the flow between a rotating and a stationary disk. *J Fluid Mech* 443:329-350.

110. Shipman RWG, Denn MM, Keuningst R (1991) Free-surface effects in torsional parallel-plate rheometry. *Ind Eng Chem Res* 30(5):918-922.

111. Ando J, Nomura H, Kamiya A (1987) The effect of fluid shear stress on the migration and proliferation of cultured endothelial cells. *Microvasc Res* 33:62-70.

112. Oliveira LA, Pecheux J, Restivo AO (1991) On the flow between a rotating and a coaxial fixed disc: Numerical validation of the radial similarity hypothesis. *Theor Comp Fluid Dyn* 2:211-221.

113. Papadaki M, McIntire LV (1999) Quantative measurements of shear-stress effects on endothelial cells. *Tissue Eng Meth Protocol* 18:577-593.

114. Tyrer NM, Shepherd D, Williams DW (2000) Methods for imaging labeled neurons together with neuropil features in drosophila. *J Histochem Cytochem* 48(11):1575-1581.

115. Portney NG, Ozkan M (2006) Nano-oncology: Drug delivery, imaging, and sensing. *Anal Bioanal Chem* 384(3):620-630.

116. Montet X, Montet-Abou K, Reynolds F, Weissleder R, Josephson L (2006) Nanoparticle imaging of integrins on tumor cells. *Neoplasia* 3(3):214-222.

117. Cognet L, Tardin C, Boyer D, Choquet D, Tamarat P*, et al.* (2003) Single metallic nanoparticle imaging for protein detection in cells. *Proc Natl Acad Sci USA* 100(20):11350-11355.

118. Li Y, Zhou Je, Tung S, Schneider E, Xi S (2009) A review on development of nanofluid preparation and characterization. *Powder Technol* 196(2):89-101.

119. Sdougos HP, Bussolari SR, Dewey CF (1984) Secondary flow and turbulence in a cone-and-plate device. *J Fluid Mech* 138:379-404.

120. Ray PC (2010) Size and shape dependent second order nonlinear optical properties of nanomaterials and their application in biological and chemical sensing. *Chem Rev* 110(9):5332-5365.

121. Dasary SSR, Senapati D, Singh AK, Anjaneyulu Y, Yu H*, et al.* (2010) Highly sensitive and selective dynamic light-scattering assay for TNT detection using p-ATP attached gold nanoparticle. *ACS Appl Mater Ins* 2(12):3455-3460.

122. Meech RW (1978) Calcium-dependent potassium activation in nervous tissues. *Annu Rev Biophys Bio* 7(1):1-18.

123. Marrion NV, Tavalin SJ (1998) Selective activation of $Ca^{2+}$-activated $K^{+}$ channels by co-localized $Ca^{2+}$ channels in hippocampal neurons. *Nature* 395(6705):900-905.

124. Lipton GR, Sutherland DJ (1970) Activity rhythms in the american cockroach, periplaneta americana. *J Insect Physiol* 16(8):1555-1566.

125. Bell WJ ed (1982) *The American Cockroach* (Chapman and Hall, New York).

126. Bruker AXS Inc (2011) Dektak 150 stylus profiler. Bruker AXS Inc Madison, WI.

127. Zygo Corporation (2011) Zygo corporation announces the NewView 600. Zygo Corporation Middlefield, CT.

128. Carl Zeiss NTS (2011) Zeiss supra 55-VP. Carl Zeiss NTS Peabody, MA.

129. Hahn L-HE, Yamada KM (1979) Isolation and biological characterization of active fragments of the adhesive glycoprotein fibronectin. *Cell* 18(4):1043-1051.

130. Lotz MM, Burdsal CA, Erickson HP, McClay DR (1989) Cell adhesion to fibronectin and tenascin: Quantitative measurements of initial binding and subsequent strengthening response. *J Cell Biol* 109(4):1795-1805.

131. Biren CA, Barr RJ, McCullough JL, Black KS, Hewitt CW (1986) Prolonged viability of human skin xenografts in rats by cyclosporine. *J Investig Dermatol* 86(6):611-614.

132. Horbett TA, Schway MB (1988) Correlations between mouse 3t3 cell spreading and serum fibronectin adsorption on glass and hydroxyethylmethacrylate–ethylmethacrylate copolymers. *J Biomed Mater Res* 22(9):763-793.

133. Gumbiner BM (1996) Cell adhesion: The molecular basis of tissue architecture and morphogenesis. *Cell* 84(3):345-357.

134. Keselowsky BG, Collard DM, García AJ (2003) Surface chemistry modulates fibronectin conformation and directs integrin binding and specificity to control cell adhesion. *J Biomed Mater Res A* 66A(2):247-259.

135. Underwood PA, Steele JG, Dalton BA (1993) Effects of polystyrene surface chemistry on the biological activity of solid phase fibronectin and vitronectin, analysed with monoclonal antibodies. *J Cell Sci* 104(3):793-803.

136. Cargill RS, Dee KC, Malcolm S (1999) An assessment of the strength of ng108-15 cell adhesion to chemically modified surfaces. *Biomaterials* 20(23-24):2417-2425.

137. Sato M, Levesque M, Nerem R (1987) Micropipette aspiration of cultured bovine aortic endothelial cells exposed to shear stress. *Arteriosclerosis* 7:276-286.

138. Stamenovic D, Wang N (2000) Cellular responses to mechanical stress: Invited review: Engineering approaches to cytoskeletal mechanics. *J Appl Physiol* 89(5):2085-2090.

139. Zhu C, Bao G, Wang N (2000) Cell mechanics: Mechanical response, cell adhesion, and molecular deformation. *Annu Rev Biomed Eng* 2:189-226.

140. Sokurenko EV, Vogel V, Thomas WE (2008) Catch-bond mechanism of force-enhanced adhesion: Counterintuitive, elusive, but . Widespread? *Cell Host Microbe* 4:314-323.

141. Xu J, Tseng Y, Wirtz D (2000) Strain-hardening of actin filament networks: Regulation by the dynamic crosslinking protein a-actinin. *J Biol Chem* 275:35886-35892.

142. Galli-Resta L, Leone P, Bottari D, Ensini M, Rigosi E*, et al.* (2008) The genesis of retinal architecture: An emerging role for mechanical interactions? *Prog Retin Eye Res* 27(3):260-283.

143. Janmey PA, McCulloch CA (2007) Cell mechanics: Integrating cell responses to mechanical stimuli. *Annu Rev Biomed Eng* 9:1-34.

144. Benoit M, Gabriel D, Gerisch G, Gaub HE (2000) Discrete interactions in cell adhesion measured by single-molecule force spectroscopy. *Nat Cell Biol* 2(6):313-317.

145. Benoit M, Gaub HE (2002) Measuring cell adhesion forces with the atomic force microscope at the molecular level. *Cells Tissues Organs* 172(3):174-189.

146. Fisher J, Hu XQ, Stewart TD, Williams S, Tipper JL*, et al.* (2004) Wear of surface engineered metal-on-metal hip prostheses. *J Mater Sci: Mater Med* 15(3):225-235.

147. Fisher J, Hu X, Tipper J, Stewart T, Williams S*, et al.* (2002) An *in vitro* study of the reduction in wear of metal-on-metal hip prostheses using surface-engineered femoral heads. *P I Mech Eng H- J Eng Med* 216(4):219-230.

148. Liang H, Shi B, Fairchild A, Cale T (2004) Applications of plasma coatings in artificial joints: An overview. *Vacuum* 73(3-4):317-326.

149. Serro AP, Completo C, Colaço R, dos Santos F, da Silva CL*, et al.* (2009) A comparative study of titanium nitrides, TiN, TiNBn and TiCN, as coatings for biomedical applications. *Surf Coat Tech* 203(24):3701-3707.

150. Williams S, Isaac G, Hatto P, Stone MH, Ingham E*, et al.* (2004) Comparative wear under different conditions of surface-engineered metal-on-metal bearings for total hip arthroplasty. *J Arthroplasty* 19(8):112-117.

151. Puecha P-H, Poole K, Knebelc D, Muller DJ (2006) A new technical approach to quantify cell–cell adhesion forces by AFM. *Ultramicroscopy* 106:637–644.

152. Sugishima A, Kajioka H, Makino Y (1997) Phase transition of pseudobinary Cr-Al-N films deposited by magnetron sputtering method. *Surf Coat Tech* 97(1-3):590-594.

153. Kim GS, Lee SY, Hahn JH (2002) Synthesis of CrN/AlN superlattice coatings using closed-field unbalanced magnetron sputtering process. S *Surf Coat Tech* 171(1-3):91-95.

154. Gall D, Shin CS, Spila T, Ode´n M, Senna MJH*, et al.* (2002) Growth of single-crystal crn on mgo(001): Effects of low-energy ion-irradiation on surface morphological evolution and physical properties. *J Appl Phys* 91(6):3589.

155. Yang Q, He C, Zhao LR, Immarigeon JP (2002) Preferred orientation and hardness enhancement of TiN/CrN superlattice coatings deposited by reactive magnetron sputtering. *Scripta Mater* 46(4):293-297.

156. Liu X, Johnson C, Li C, Xu J, Cross C (2008) Developing tialn coatings for intermediate temperature solid oxide fuel cell interconnect applications. *Int J Hydrogen Energ* 33(1):189-196.

157. Diebold U (2003) The surface science of titanium dioxide. *Surf Sci Rep* 48(5-8):53-229.

158. Aladjem A (1973) Anodic oxidation of titanium and its alloys. *J Mater Sci* 8(5):688-704.

159. Morita M, Ohmi T, Hasegawa E, Kawakami M, Suma K (1989) Control factor of native oxide growth on silicon in air or in ultrapure water. *Appl Phys Lett* 55(6):562.

160. Kageshima H, Shiraishi K (1998) First-principles study of oxide growth on Si(100) surfaces and at Si)_{2}/Si(100) interfaces. *Phys Rev Lett* 81(26):5936.

161. Wenzel RN (1949) Surface roughness and contact angle. *J Phys Colloid Chem* 53(9):1466-1467.

162. Kulinich SA, Farzaneh M (2009) Effect of contact angle hysteresis on water droplet evaporation from super-hydrophobic surfaces. *Appl Surf Sci* 255(7):4056-4060.

163. Allred AL (1961) Electronegativity values from thermochemical data. *J Inorg Nucl Chem* 17(3-4):215-221.

164. Sanderson RT (1983) Electronegativity and bond energy. *J Am Chem Soc* 105(8):2259-2261.

165. Sanderson RT (1986) Electronegativity and bonding of transitional elements. *Inorg Chem* 25(19):3518-3522.

166. Pastoriza-Gallego MJ, Casanova C, Legido JL, Piñeiro MM (2011) CuO in water nanofluid: Influence of particle size and polydispersity on volumetric behaviour and viscosity. *Fluid Phase Equilibr* 300(1-2):188-196.

167. Moghaddami M, Mohammadzade A, Esfehani SAV (2011) Second law analysis of nanofluid flow. *Energ Convers Manage* 52(2):1397-1405.

168. Kuleznev VN, Mel'nikova OL, Klykova VD (1978) Dependence of modulus and viscosity upon composition for mixtures of polymers. Effects of phase composition and properties of phases. *Eur Polym J* 14(6):455-461.

169. Sperling LH (2006) *Introduction to Physical Polymer Science* 4th ed. (John Wiley & Sons, Inc, Hoboken, NJ).

170. Collyer AA, Clegg DW (1988) *Rheological Measurement* (Elsevier Applied Science Publishers Ltd, New York).

171. Murshed SMS, Leong KC, Yang C (2005) Enhanced thermal conductivity of $TiO_2$--water based nanofluids. *Int J Therm Sci* 44(4):367-373.

172. Yi G, Sayer M (1996) An acetic acid/water based sol-gel pzt process II: Formation of a water based solution. *J Sol-Gel Sci Techn* 6(1):75-82.

173. Kundu S, Panigrahi S, Praharaj S, Basu S, Ghosh SK*, et al.* (2007) Anisotropic growth of gold clusters to gold nanocubes under UV irradiation. *Nanotechnology* 18(7):075712.

174. Basu S, Ghosh SK, Kundu S, Panigrahi S, Praharaj S*, et al.* (2007) Biomolecule induced nanoparticle aggregation: Effect of particle size on interparticle coupling. *J Colloid Interf Sci* 313(2):724-734.

175. Ratner BD, Castner DG (1997) Electron spectroscopy for chemical analysis. *Surface analysis: The principal techniques* 5th ed, Vickerman JC (John Wiley & Sons, United Kingdom).

176. Moran MJ, Shapiro HN (2004) *Fundamentals of Engineering Thermodynamics* 5 ed. (John Wiley & Sons, New York).

177. Pinal R (2008) Entropy of mixing and the glass transition of amorphous mixtures. *Entropy* 10(3):207-223.

178. Delaire O, Swan, Wood T, Fultz B (2004) Negative entropy of mixing for vanadium-platinum solutions. *Phys Rev Lett* 93(18):185704.

179. Mirza UA, Chait BT (1997) Do proteins denature during droplet evolution in electrospray ionization? *Int J Mass Spectrom* 162(1-3):173-181.

180. Mirsky AE, Pauling L (1936) On the structure of native, denatured, and coagulated proteins. *Proc Natl Acad Sci USA* 22(7):439-447.

181. Yan Z, Wang J, Kong W, Lu J (2004) Effect of temperature on volumetric and viscosity properties of some [alpha]-amino acids in aqueous calcium chloride solutions. *Fluid Phase Equilibr* 215(2):143-150.

182. You C-C, Verma A, Rotello VM (2006) Engineering the nanoparticle-biomacromolecule interface. *Soft Matter* 2(3):190-204.

183. Mamedova NN, Kotov NA, Rogach AL, Studer J (2001) Albumin−cdte nanoparticle bioconjugates: Preparation, structure, and interunit energy transfer with antenna effect. *Nano Lett* 1(6):281-286.

184. Ben-Naim A (1975) Structure-breaking and structure-promoting processes in aqueous solutions. *J Phys Chem* 79(13):1268-1274.

185. Kaminsky M (1957) Ion-solvent interaction and the viscosity of strong-electrolyte solutions. *Discuss Faraday Soc* 24:171-179.

186. Graessley WW (1967) Viscosity of entangling polydisperse polymers *J Phys Chem* 47(6):1967.

187. Richard A, Margaritis A (2002) Production and mass transfer characteristics of non-newtonian biopolymers for biomedical applications. *Crit Rev Biotechnol* 22:374-355.

188. Rocha A, Zhou Y, Kundu S, Gonzalez J, BradleighVinson S*, et al.* (2011) *In vivo* observation of gold nanoparticles in the central nervous system of blaberus discoidalis. *J Nanobiotechnol* 9(1):5.

189. Shukla R, Bansal V, Chaudhary M, Basu A, Bhonde RR*, et al.* (2005) Biocompatibility of gold nanoparticles and their endocytotic fate inside the cellular compartment: A microscopic overview. *Langmuir* 21(23):10644-10654.

190. Daniel MC, Astruc D (2004) Gold nanoparticles: Assembly, supramolecular chemistry, quantum-size-related properties, and applications toward biology, catalysis, and nanotechnology. *Chem Rev* 104(1):293-346.

191. Bergen JM, von Recum HA, Goodman TT, Massey AP, Pun SH (2006) Gold nanoparticles as a versatile platform for optimizing physicochemical parameters for targeted drug delivery. *Macromol Biosci* 6(7):506-516.

192. Niidome T, Yamagata M, Okamoto Y, Akiyama Y, Takahashi H*, et al.* (2006) PEG-modified gold nanorods with a stealth character for *in vivo* applications. *J Control Release* 114(3):343-347.

193. Cedervall T, Lynch I, Lindman S, Berggard T, Thulin E*, et al.* (2007) Understanding the nanoparticle-protein corona using methods to quantify exchange rates and affinities of proteins for nanoparticles. *P Natl A Sci* 104(7):2050-2055.

194. Lundqvist M, Stigler J, Elia G, Lynch I, Cedervall T*, et al.* (2008) Nanoparticle size and surface properties determine the protein corona with possible implications for biological impacts. *Proc Natl Acad Sci USA* 105(38):14265-14270.

195. Vinson SB (1974) The role of the foreign surface and female parasitoid secretions on the immune response of an insect. *Parasitology* 68:27-33.

196. Sahoo B, Goswami M, Nag S, Maiti S (2007) Spontaneous formation of a protein corona prevents the loss of quantum dot fluorescence in physiological buffers. *Chem Phys Lett* 445(4-6):217-220.

197. Hoyle G (1953) Potassium ions and insect nerve muscle. *J Exp Biol* 30(1):121-135.

198. Luo X, Morrin A, Killard AJ, Smyth MR (2006) Application of nanoparticles in electrochemical sensors and biosensors. *Electroanalysis* 18(4):319-326.

# VITA

Aracely Rocha-Zapata received her Bachelor of Science degree in mechanical engineering from The University of Texas PanAmerican in 2006. She entered the mechanical engineering program at Texas A&M University in August 2006 and completed her M.S. in mechanical engineering in December 2008. She continued at Texas A&M University and completed her doctorate degree in mechanical engineering in August of 2011. Her research interests include the fields of biomaterials and biocompatibility.

During her graduate education, Ms. Rocha has completed two industry internships at Ford Motor Company, and has performed research at Texas A&M University and abroad at Ecole Centrale de Lyon in France and at The University of Science and Technology Beijing in China.

Ms. Rocha-Zapata may be reached at Department of Mechanical Engineering c/o Dr. Hong Liang 3123 TAMU College Station, TX 77843-3123. Her email address is aracelyrocha@gmail.com